Stability of Localised Surface Plasmon Resonance of Metal Nanoparticles

Mads Larsen

Master's Thesis

Department of Materials and Production
Aalborg University
June 3$^{\text{rd}}$ 2019

AALBORG UNIVERSITY
STUDENT REPORT

Department of
Material and Production
Skjernvej 4A
9220 Aalborg East
https://www.mp.aau.dk/

Title:
Stability of Localised Surface Plasmon Resonance of Metal Nanoparticles

Project:
Master's Thesis

Project Period:
February 1st, 2019 - June 3rd, 2019

Author
Mads Larsen

Supervisor:
Associate Prof. Vladimir N. Popok

Number of Pages: 61
Appendix: 7
Completed: 29/05-2019

Abstract:

Denne rapport er et specialeprojekt udarbejdet under titlen *Stability of Localised Surface Plasmon Resonance of Metal Nanoparticles*. Formålet med rapporten er at undersøge stabiliteten af localised surface plasmon resonance (LSPR) af kobber- og sølvnanopartikler afhængigt af 3 partikelstørrelser, substratet de er deponeret på og den atmosfære hvori de er opbevaret. Foruden testes ozonerings effekt på nanopartiklers optiske egenskaber. En magnetron sputtering cluster apparatus (MaSCA) anvendes til at deponere nanopartiklerne på substraterne, og spektrofotometri anvendes til at måle prøvernes optiske egenskaber. Sølvpartikler deponeret på quartz-substrater viser en lineær tendens i LSPR stabilitet - større partikler viser en højere grad stabilitet af plasmoniske egenskaber. Kun de mindste sølvpartikler viser en formindskning af plasmonbåndsintensiteten på over 25 % over en periode af 80 dage. Kun mindre partikler er påvirket af atmosfære. To sæt prøver blev ozoneret for at studere påvirkningen af denne procedure og viste ufyldestgørende resultater og kræver videre undersøgelse. Sølvpartikler deponeret på PMMA-substrater viser en høj grad af stabilitet af plasmoniske egenskaber over 80 dage uafhængigt af atmosfære. Ligeledes viser kobbernanopartikler den samme lineære tendens som sølv. Ligesom for sølv er kun mindre kobberpartikler påvirket af atmosfære. Ozonering er kun en effektiv metode til at lave et beskyttende lag omkring kobber for større partikler. Generelt viser kobber- og sølvnanopartikler produceret med en MaSCA en høj grad af stabilitet i plasmoniske egenskaber uafhængigt af omgivende atmosfære og substrat, hvorpå de er deponeret og med større grad af stabilitet for partikler af større dimensioner.

Preface

This report is produced by Mads Larsen, 10th semester physics student at Aalborg University. The main goal is to investigate the stability of localised surface plasmon polaritons of Ag and Cu nanoparticles produced by a magnetron-based sputtering cluster apparatus over time depending on the size of the deposited metal nanoparticles, the type of substrate they are deposited on, and the atmosphere they are stored in during the time in which they are investigated.

The report begins with a brief introduction to atomic clusters/nanoparticles and their size dependent properties. Next, the formation of clusters from the gas phase is described as well as different cluster production methods, with emphasis on magnetron sputtering. A theoretical description of surface plasmon resonance of spherical metal nanoparticles is then derived. Afterwards, the degradation of surface plasmon resonance of metal nanoparticles is shortly reviewed. Lastly, the experimental sections describes the the methods used for production and characterisation of substrates and nanoparticles and presents and discusses the obtained data.

Throughout the report, there are references which are collected in the bibliography at the end of the report. When a reference is made, it is done with [Reference Number] and the reference will guide you to the bibliography where books are listed with authors, title, edition, year, and publisher, while articles are listed with authors, title, journal, volume, and year. References are listed in the same order as they appear in the report. Figures, tables, and equations are numbered with relation to the chapters they appear in, e.g. the first figure in chapter 3 is numbered 3.1, the second 3.2 etc. Explanatory text to each figure is found right below, whereas for tables it is found right above.

Mads Larsen

Table of Contents

Chapter 1

Introduction

In recent years, clusters/nanoparticles (NPs) and nanostructures have been a greater area of research due to the fact that their properties can vary from those of a single atom to those of a bulk of atoms depending on their sizes. As an intermediate between the bulk state and discrete molecules, NPs of particular sizes also have properties which are distinctly different from both states[1].

One of these specific optical phenomena is the ability to excite localised surface plasmon polaritons with associated localised surface plasmon resonance (LSPR). The use of NPs and their LSPR have in recent times been used in various optical devices, for instance by enhancing the optical response of nearby molecules and manipulation of light in plasmonic circuitry[2][3]. The LSPR of metal NPs is sensitive to changes of the dielectric constant of the surrounding medium and as such, it is possibly to fine-tune the medium and nanoparticles to synthesise materials with interesting optical properties. Examples of LSPR include time-temperature indicators for food where the LSPR of a NP changes depending the shape of the NP[4]; wave-guides where plasmonic NP arrays are applied to allow for the guiding and strong amplification of light waves[5][6]; controlled hotspots where arrays of plasmonic metal NPs generate a large localised electromagnetic field[7]; and in SERS detection where hotspots generated by, for example, nano arrays are created in order to enhance the signal of nearby molecules in order to detect them more easily[8].

Silver and gold nanoparticles in particular are used in LSPR methods, as they exhibit excellent plasmonic properties. Gold, however, is more expensive than silver and much less abundant. Silver would therefore be the perfect candidate for LSPR methods if not for the fact that it becomes easily contaminated by other species in its surrounding environment[9]. Likewise, copper would be a good candidate for LSPR methods but also suffers from degradation[10]. As such, investigations into the cause of the degradation of these NPs and particularly methods to prevent it are of great interest.

1.1 Objective

The objective of this project is to investigate the stability of the LSPR of silver and copper NPs depending on the size of NPs, the substrate on which they are deposited, and the atmosphere in which they are stored. Highly pure and monocrystalline Ag and Cu NPs are deposited on clean quartz and/or quartz coated by thin poly(methyl methacrylate) (PMMA) films using a magnetron sputtering cluster apparatus in high to ultra-high vacuum conditions. For every metal species, particle size, and type of substrate, a pair of samples is produced to be stored one of which is store in an ambient atmosphere and one which is stored in a nitrogen box. Also, the effect of ozonation on plasmonic properties of NPs is studied. The purpose of ozonation is to investigate if it is possible to form a protective layer of oxide around the NPs which prevents them from interacting with atmospheric species. Plasmonic properties of the samples are monitored, initially on a daily basis, later on a weekly basis in order to observe the evolution of LSPRs over time, up to 80 days.

Chapter 2

Atomic Clusters

Materials are commonly dividing into two categories depending on the properties they exhibit; one category being individual atoms and molecules and a second category being bulk materials. Atomic clusters are an intermediate step between these small, individual atoms/molecules and bulk materials. A clusters consists of multiple atoms which have aggregated together. Depending on the size of the cluster and the atoms which have bounded together, the particular properties of the clusters vary significantly. In the two extremes, i.e. when the clusters are so small as to resemble individual atoms and when they are large enough to resemble bulk materials, the clusters have corresponding properties. However, as an intermediate state, the clusters can be considered to constitute an entirely new type of material which possesses unique properties.

2.1 Spherical Cluster Approximation

One of the methods of describing clusters is the spherical cluster approximation (SCA) in which the clusters consisting of N atoms is approximated to be a sphere. This model best approximates larger clusters and allows for equations to be derived for the number of surface atoms and in extension the fraction of surface atoms compared to the total number of clusters atoms.

A spherical cluster consisting of N atoms has a cluster volume V_c found by

$$V_c = NV_a, \tag{2.1}$$

where V_a is the volume of a single atom. This, however, does not take into account the fact that the spheres do not fill space entirely and as such is not a perfect representation. Expanding on this allows for a relation between cluster and atomic radii given by

$$\frac{4}{3}\pi R_c^3 = N\frac{4}{3}\pi R_a^3, \tag{2.2}$$

where R_c and R_a are the cluster radius and atomic radius, respectively. Further rearranging leads to the relation

$$R_c = N^{1/3}R_a. \tag{2.3}$$

Likewise, the diameter of the cluster can be found by the relation

$$D_c = 2R_c = 2N^{1/3}R_a. \tag{2.4}$$

The surface area S_c of the cluster can then be found by

$$S_c = 4\pi R_c^2 = 4\pi(N^{1/3}R_a)^2 = N^{2/3}S_a, \tag{2.5}$$

S_a being the surface area of the atom constituent. The number of surface atoms N_s can be found by dividing the surface area of the cluster by the cross-sectional area A_a of the atom, leading to

$$N_s = \frac{4\pi N^{2/3} r_a^2}{\pi R_a^2} = 4N^{2/3}. \tag{2.6}$$

The fraction of atoms which resides on the surface F_s is given by

$$F_s = \frac{N_s}{N} = 4N^{-1/3}. \tag{2.7}$$

A lot of cluster properties depend on this fraction as the amount of surface atoms compared to bulk atoms readily available for reactions is much larger than that of a bulk material.

As mentioned earlier, the SCA best describes larger clusters and as such starts to break down when N becomes small[1]. Fig. 2.1 shows the fraction of surface atoms F_s plotted against $N^{-1/3}$ for clusters composed of icosahedral atoms which is commonly observed for rare gas and metal clusters [1]. It can be seen that the approximation fits better as $N^{-1/3}$ tends towards zero which is equivalent to the clusters consisting of more and more atoms.

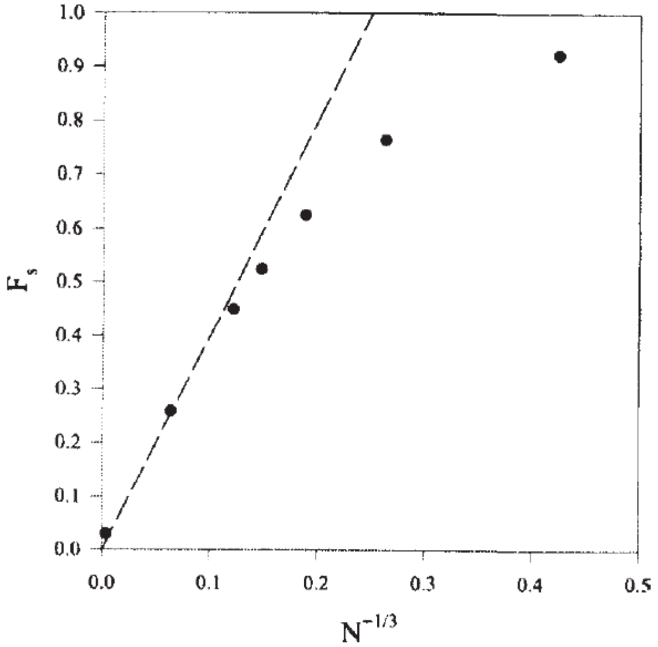

Figure 2.1. Fraction of surface atoms F_s plotted against $N^{-1/3}$ for icosahedral geometric shell clusters. The dashed line represents the prediction of the SCA. Adopted from [1].

Depending on the number of atoms which the cluster consists of, it is possible to divide the cluster size into three different regimes: small clusters which contain less than 100 atoms; medium-sized clusters which contain between 100-10,000 atoms; and large clusters which contain more than 10,000 atoms. For the three regimes, the range of diameters can be found from Eq. (2.4). The ranges and the corresponding diameters of the atoms are shown in Tab. 2.1.

Table 2.1. Classification of clusters according to size. N is the number of atoms, D is the diameter for a cluster of sodium atoms in nanometers. Adopted from [1].

	Small	Medium	Large
N	$\leq 10^2$	10^2 - 10^4	$> 10^4$
D [nm]	≤ 1.9	1.9 - 8.6	> 8.6

2.1.1 Scaling Laws

For varying sizes of clusters, generic cluster properties (G) show a regular variation. Examples of these cluster properties include the ionization energy (IP), electron affinity (EA), melting temperature (T_m), and binding energy (E_b). Using the SCA model, it is possible to describe these cluster size effects by the use of a simple scaling law through the cluster radius or the number of atoms:

$$G(R) = G(\infty) + aR^{-\alpha}, \tag{2.8}$$

$$G(N) = G(\infty) + bN^{-\beta}. \tag{2.9}$$

Here, a and b are constants specific to G while G(∞) is the value of property G in the bulk limit[1][11]. As the scaling laws make use of the bulk property, the scaling laws typically approximate clusters in the medium and large cluster regimes better. Likewise, many properties depend on $F_s \propto N^{-1/3} \propto 1/R$ and as such, the exponents in equations (2.8) and (2.9) are generally $\alpha = 1$ and $\beta = 1/3$ [1].

Examples of the application of scaling laws include the ionization energies and melting temperatures. For potassium clusters with up to 100 atoms, it is possible to fit the ionization energy with a high degree of accuracy by the following interpolation formulae

$$\mathrm{IP}^K(N)/\mathrm{eV} = 2.3 + 2.04N^{-1/3}, \tag{2.10}$$

$$\mathrm{IP}^K(R)/\mathrm{eV} = 2.3 + 5.35(R/\text{Å})^{-1}. \tag{2.11}$$

Eq. (2.10) is plotted together with experimental values of IP^K for the potassium clusters is shown in Fig. 2.2.

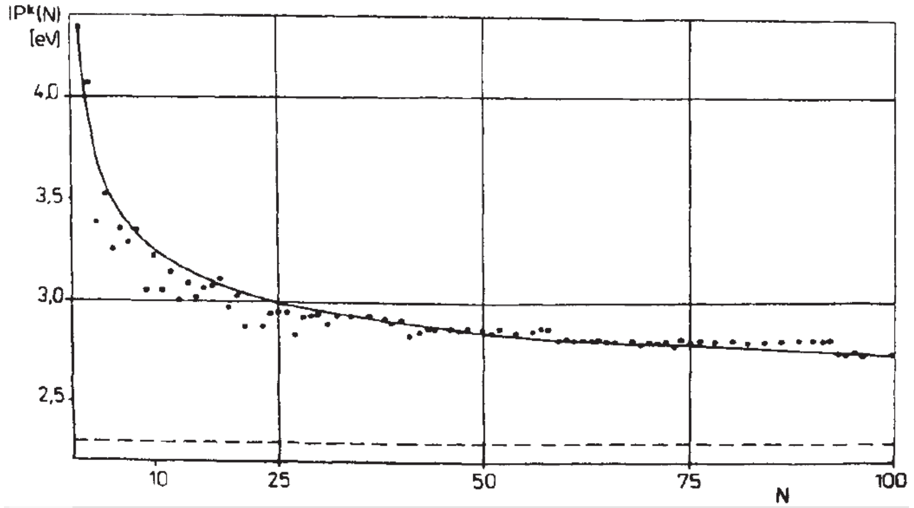

Figure 2.2. The ionization energy of potassium clusters as a function of cluster size N. The points represent experimental data, the solid line is taken from the interpolation formula Eq. (2.10), and the dashed line indicates the bulk work function. Adopted from [12].

Likewise, it is possible to approximate the melting temperatures. Specifically for gold clusters, the melting temperature has been found to decrease with decreasing cluster size, following a $1/R$ trend, fitting:

$$T_M^{\mathrm{Au}}(R)/K = 1336.15 - 5543.65(R/\text{Å})^{-1}, \tag{2.12}$$

as shown in Fig. 2.3. For small gold clusters, the melting temperature was found to be as low as 300 K [1] which is significantly lower than the corresponding bulk melting temperature of 1336 K.

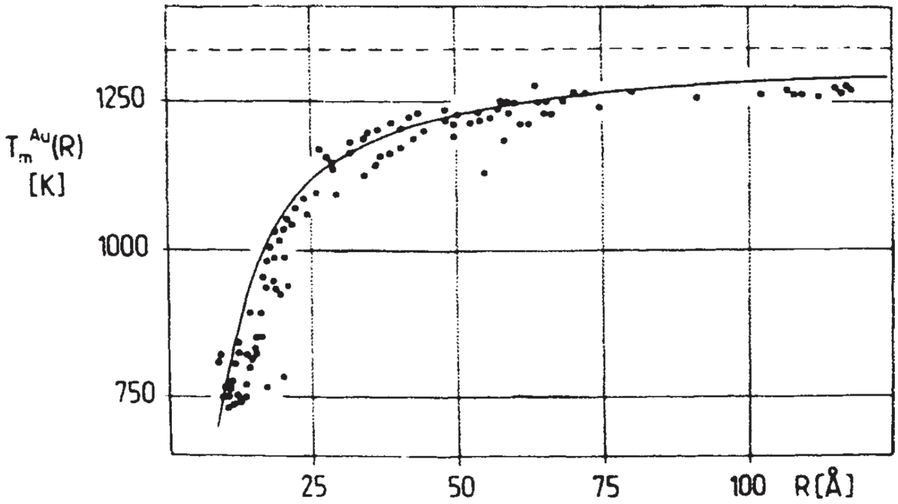

Figure 2.3. The melting temperature of gold clusters as a function of radius R. The points represent experimental data, the solid line is taken from the interpolation formula, and the dashed line indicates the bulk melting temperature. Adopted from [12].

Figures 2.2 and 2.3 show good agreement with scaling laws, though for smaller clusters, deviations are observed. Large deviations, which are usually observed as oscillations about the smooth cluster size effect (CSE) trend, are observed for many properties in the medium and particularly small cluster size regimes. These deviations arise due to quantum size effects and surface effects. The behaviour of the cluster properties depending on the number of atoms in the cluster is shown in Fig. 2.4.

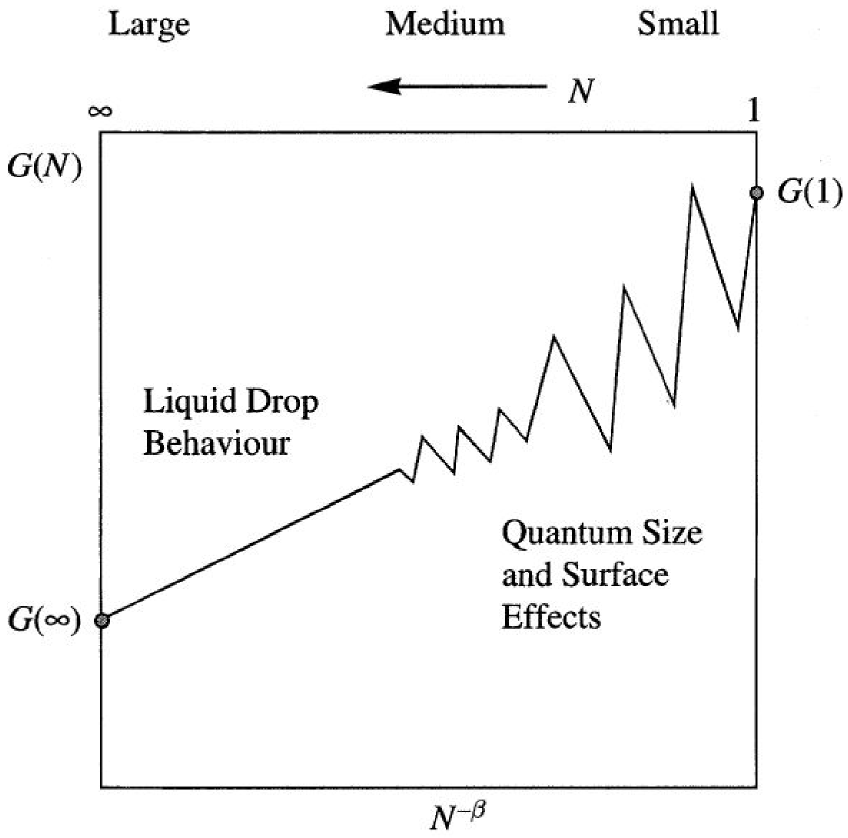

Figure 2.4. Schematic representation of the variation of a generic cluster property (G) with cluster size. Adopted from [13].

2.2 Formation of Nano Clusters

2.2.1 Gas Phase cluster Growth

Clusters which are grown in the gas phase form from individual atoms/molecules and then nucleate together. This is usually facilitated by rapid cooling of the gas causing supersaturation which makes the formation and growth of clusters from the excess vapor possible. The generation of the clusters can be divided into two steps: nucleation and growth. During the nucleation process, clusters of stable phase are formed from the metastable one, where a metastable state for a gas aggregation source is a supersatured vapor of a material of interest. The nucleation process starts with the collision of atoms which allows formation of a small cluster. For a metal species (M) and a buffer gas (He), the process can be described by three-body-collision:

$$\mathrm{M} + \mathrm{M} + \mathrm{He} \rightarrow \mathrm{M}_2 + \mathrm{He}. \tag{2.13}$$

A minimum of three atoms is required to trigger the nucleation process as the conservation of energy and momentum must be fulfilled at the same time. The helium atom must be present in the collision in order to carry away the excess energy from the binding of the metal atoms. Because the binding energy of helium is significantly lower than that of the metal, it is not altered during the collision process. Only clusters of certain sizes which are thermodynamically stable can serve for further cluster growth[14]. This size is called the critical size and depends on experimental conditions such as temperature, pressure, etc. Theoretical calculations have shown that dimers can be considered a stable nucleus for cluster growth[15][16].

When the initial cluster nucleation step has occurred, further cluster growth is governed by four processes: atom attachment, coagulation (kinetic and diffusion modes), coalescence, and aggregation[15]. The four processes are shown in Fig. 2.5. Generally, the clusters will grow larger the longer the time they spend in the aggregation region as these four processes take a longer time to occur.

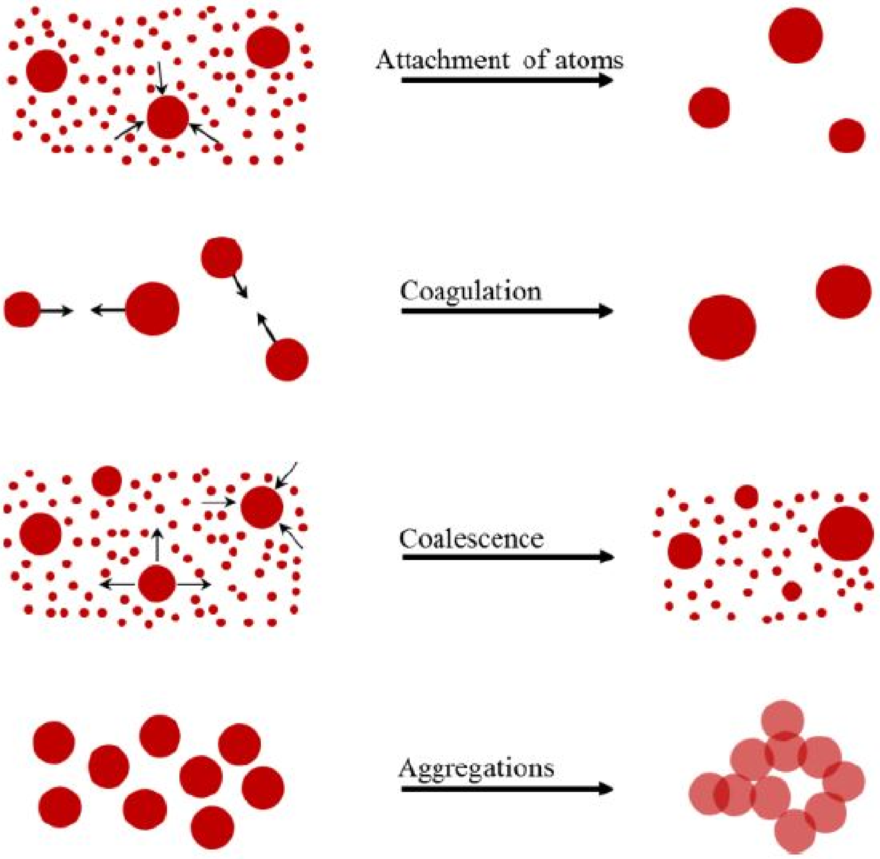

Figure 2.5. The four mechanism of cluster growth after the initial nucleation process.

The atom attachment process in which clusters grow larger by single atom addition to the cluster is shown in the first panel in Fig. 2.5. The process can be described by:

$$\mathrm{M}_n + \mathrm{M} \rightarrow \mathrm{M}_{n+1}, \tag{2.14}$$

and the additional energy from the attachment is carried into the buffer gas. The rate constant for the attachment is proportional to the cluster size, and rate constants for cluster growth is much larger than for dimer formation, leading to large cluster sizes[15].

The coagulation process in which two smaller clusters band together to form a single larger cluster is shown in the second panel in Fig. 2.5. The process can be described by:

$$\mathrm{M}_{n-m} + \mathrm{M}_m \rightarrow \mathrm{M}_n, \tag{2.15}$$

where n and m are the number of atoms in each cluster. The coagulation process can happen in two regimes where either the cluster is only strongly interacting with single gas atoms (the kinetic regime) or the cluster interacts with many gas atoms simultaneously (the diffusion regime). These inelastic collisions occur due to the Brownian motion of the gas atoms and cluster. The size distribution of growth thus depends on the regime of atom(s)-cluster interaction[15][17]. An illustration of the differences between the two regimes is shown in Fig. 2.6.

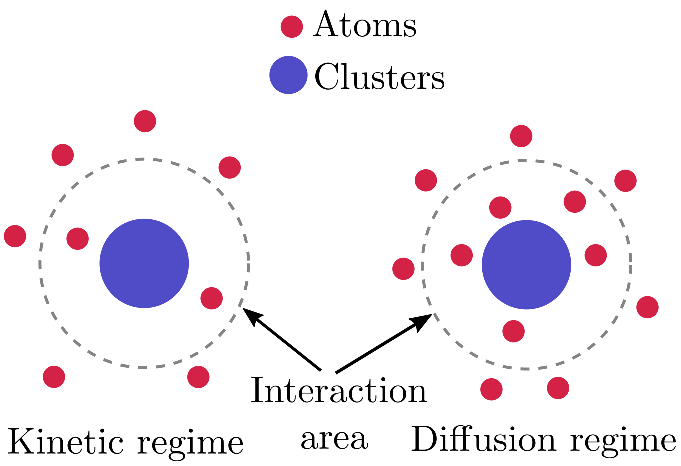

Figure 2.6. Coagulation process: kinetic and diffusion regimes of cluster interaction with surrounding atoms in the course of cluster motion in a buffer gas.

The coalescence process results from the interaction of clusters with a parent vapor and is also known as Ostwald ripening. Here, larger clusters grow larger through the absorption of vapor from smaller clusters. This process happens for very low degrees of supersaturation[15]. The rate of evaporation for smaller clusters is higher than its rate of atom attachment while for larger clusters, this relation is inversed. As a result of this, larger clusters grow, while smaller clusters evaporate.

In the aggregation process, the individual clusters join due to contact between them while still retaining much of their original shape. This process possibly plays a limited role in the cluster beams formed by metal clusters[15].

The size distribution of the clusters is dependent on the charge of the clusters as well as the ratio of positively and negatively charged particles. While theoretical studies of the charging of clusters in different plasma environments have shown that the charge on clusters is non-trivial, it is reasonable in experimental work to assume that the vast majority of the clusters leaving the aggregation chamber is either singly or neutrally charged, as shown by Ganeva et al[18]. The charge distribution is highly dependent on cluster production source and experimental parameters.

Generally, the production of nano clusters with a cluster apparatus consists of three main steps: production, mass selection (if needed), and detection. Depending on the cluster material, desired size, and distribution of the particles as well as charge, different experimental setups are required.

The production of clusters often requires the use of atomic vapor. Atomic vapors can be created through several methods including arc discharge where a large current between two electrodes is applied to cause heating, laser vaporisation where focused nanosecond laser pulses are used to vaporise a target material, ion sputtering where ions are accelerated at the clean surface of a target and the surface atoms are released from the surface, and magnetron sputtering which is used in this project and as such is described below. When an atomic vapor has been created, a cooling or carrier gas such as He is typically introduced in order to facilitate aggregation as described above.

2.2.2 Magnetron Sputtering

Magnetron sputtering utilizes the ionization of low-pressure inert gas (typically argon), thus forming a plasma. The ionization starts in the arc discharge between two electrodes, one of which is the target material to be sputtered. The electric field then accelerates the electrons towards the anode. These electrons ionize more neutral argon atoms by the following reaction

$$\mathrm{e}^- + \mathrm{Ar} \rightarrow 2\mathrm{e}^- + \mathrm{Ar}^+. \tag{2.16}$$

The ionization of the argon atom releases another electron which in turn may be used for further ionization, allowing for self-sufficient generation of plasma.

When the plasma is stabilised, sputtering occurs by energetic Ar^+ ions being accelerated towards the cathode (target). A magnetic field is used to confine the secondary electrons and keep ionization of plasma for sustainable sputtering[1][19][20]. The magnetic field is located above the target which is achieved by placing a magnet beneath the target like shown in Fig. 2.7(a). The entrapment of the secondary electrons can be understood through the Lorentz force equation:

$$\mathbf{F} = q(\mathbf{E} + \mathbf{v} \times \mathbf{B}), \tag{2.17}$$

where $\mathbf{F}$ is the force acting on a particle with charge q and velocity $\mathbf{v}$, and $\mathbf{E}$ and $\mathbf{B}$ are the electric and magnetic fields, respectively. In the magnetron case, the electric field between the anode and cathode generates a force depending on the charge of the particles, whereas the magnetic force must be perpendicular to both the magnetic field and the direction of motion[21]. This results in a circular confinement of the secondary electrons around the center of the target, behind which one of the magnetic poles is placed.

Fig. 2.7(a) shows a side-view schematic of the immediate setup around the magnetron and illustrates the magnetic and electric fields of the setup. Likewise in Fig. 2.7(a), both argon ions and free electrons are shown, demonstrating that an argon atom which has been ionized will move in the opposite direction as the electron on its path to the cathode. Due to the higher mass of the argon ion, it is much less affected by the magnetic field compared to the electron. As the ionization rate of argon atoms is much higher in the area around the cathode perpendicular to the magnetic field, a toroidal trench will be formed in the target as shown in Fig. 2.7(b). The particles take on a toroidal motion because the

Lorentz force from the magnetic field and applied electric field oscillates in a harmonious fashion as can be seen from Fig. 2.7(c), with $\mathbf{F_B}$ and $\mathbf{F_E}$ being the magnetic and electric forces, respectively. The magnetic field increases sputtering yield in two ways; one is by trapping the electrons and a second is by increasing their path length on the distance from the cathode to the anode which increases the probability of argon ionization. This also means that a lower operating pressure can be used during the sputtering process compared to traditional sputtering[21].

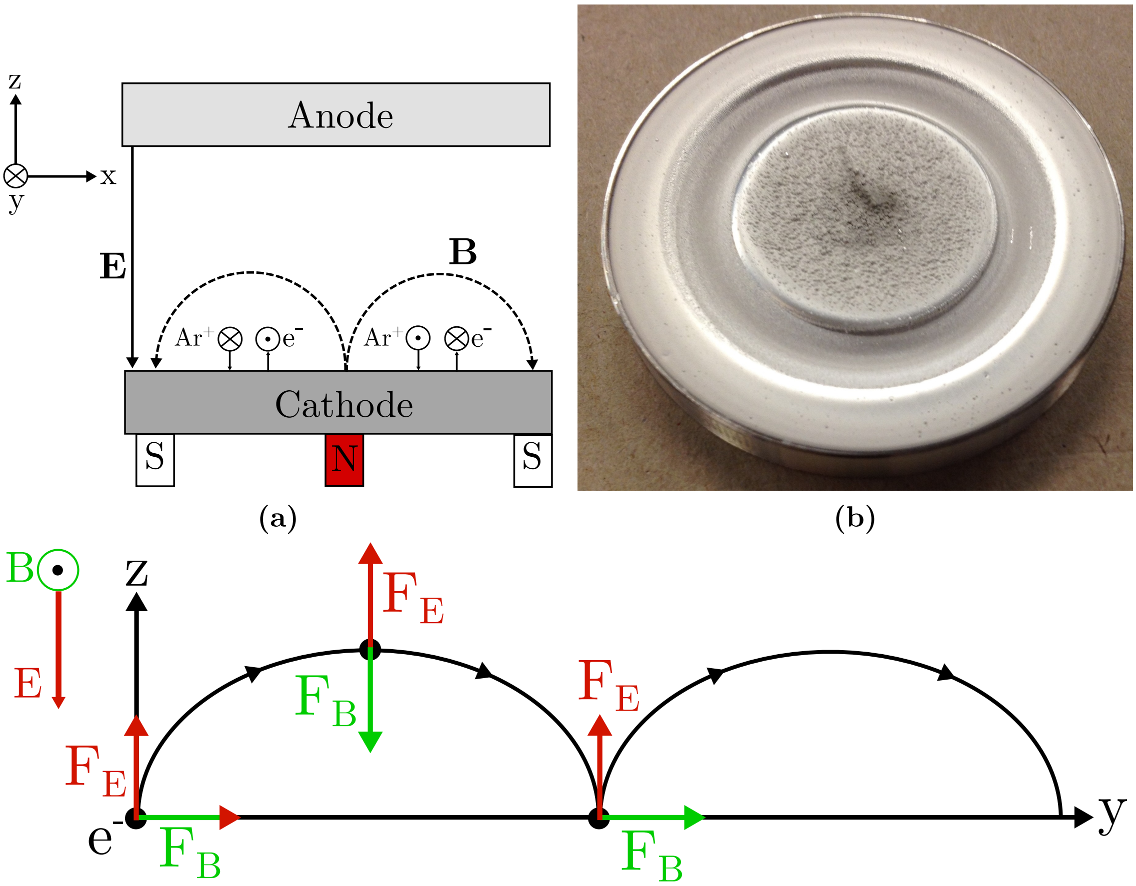

(a) **(b)**

(c)

Figure 2.7. Illustration of the magnetron sputtering setup. (a) 2D view of the electric and magnetic fields lines above the cathode/target. It is shown how an ion or electron is influenced by the fields. (b) Picture of a silver target with the erosion trench, showing that the erosion is in fact confined. (c) cycloidal motion of electron in the y-direction. The second electrons are assumed to have no initial velocity, meaning that their motion is initiated by the electric field. F_B and F_E are the magnetic and eletric forces, respectively.

The working voltages between the anode and cathode are generally about 100-500 V. The clusters produced may vary in sizes that range from several atoms to several million atoms. The amount of charged particles depend on the sputtered species but typically ranges from 20-80 % of the total amount of clusters produced[19][22].

After sputtering, the eroded material is condensed into clusters. This process is facilitated by a carrier gas (commonly helium) which can be cooled down by collisions within the walls of an aggregation chamber which has a flow of liquid nitrogen inside them as seen in Fig. 2.8. Next, the eroded material is lead through a nozzle[23]. The source can provide a rather high cluster beam flux of up to 10^{12} clusters/cm^2. This method is applicable for conducting and semiconducting materials.

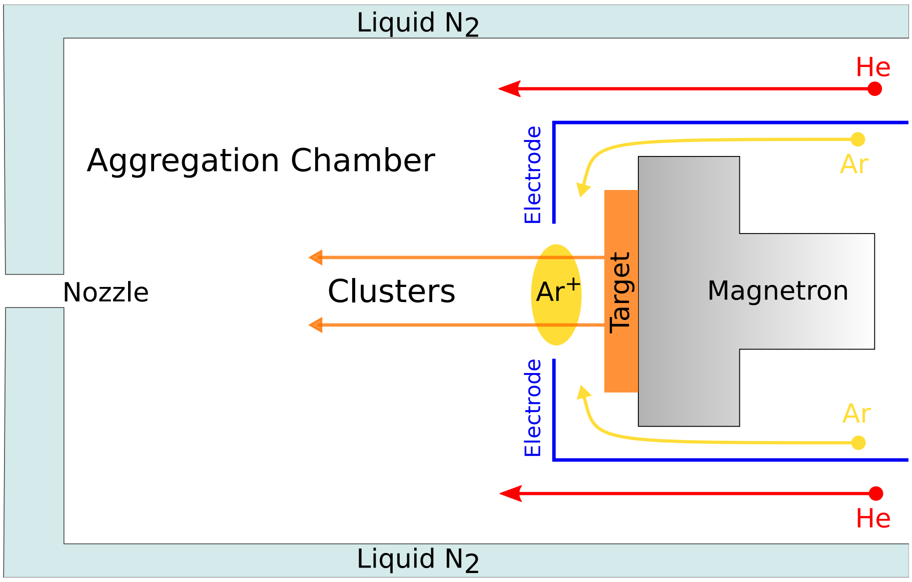

Figure 2.8. Schematic overview of the aggregation chamber in a typical magnetron sputtering source.

The cluster production is determined by several interrelated parameters which are typically varied for optimization of the beam intensity for the desired cluster size. The flow of Ar and He have major effects on the cluster production, Ar for the sputtering and He for the condensation. It is possible to vary the distance between the nozzle and the magnetron by the use of a linear translator. The translator ranges from 0-100 mm, allowing for tuning of the cluster size and beam intensity. Typically, smaller cluster sizes need a smaller aggregation length while larger size clusters need a greater aggregation length. Depending on the flow of the Ar and He gasses as well as the temperature, it is possible to optimise the condensation of the clusters. The particular flows and temperature, however, depend on the desired size of clusters as well as the particular setup used.

The main disadvantage of the magnetron sputtering source is issues which are related to beam stability and reliability. The continuous target erosion affects the cluster size distribution[24][25][26], the ion distribution in the near-cathode region[27], and the deposition rate[28]. Nevertheless, gas aggregation sources utilizing magnetron sputtering are widely used for research and industrial purposes. They allow for the production of particles of various metals and alloys or core-shell structures, and even super pure particles with perfect crystalline structures[29]. When the sources are equipped by mass-filtering systems, NP size selection can be provided. The capabilities of magnetron-based sources make them attractive for NP deposition and embedding into different materials.

2.3 Optical Properties of Metal Nanoparticles in Dielectric Environments

When a metal NP is irradiated by light, the oscillating electric field causes the conduction electrons of the NP to oscillate coherently, leading to a displacement of the electron cloud about the core of the particle as illustrated in Fig. 2.9. Given the difference in charge between the core and the electron cloud, Coulomb attraction gives rise to a restoring force which induces the electron cloud to oscillate collectively and relatively to the core[3][30]. This collective oscillation causes dipole formation. The optical properties of a NP depends on several parameters, including the particle size, the shape of the particle, the type of the material, and its surrounding dielectric medium. As this multitude of factors impact the optical properties of the NP, it is of interest to investigate simple theoretical solutions which give an approximate form for the extinction cross-section of a NP when considering Mie's solutions.

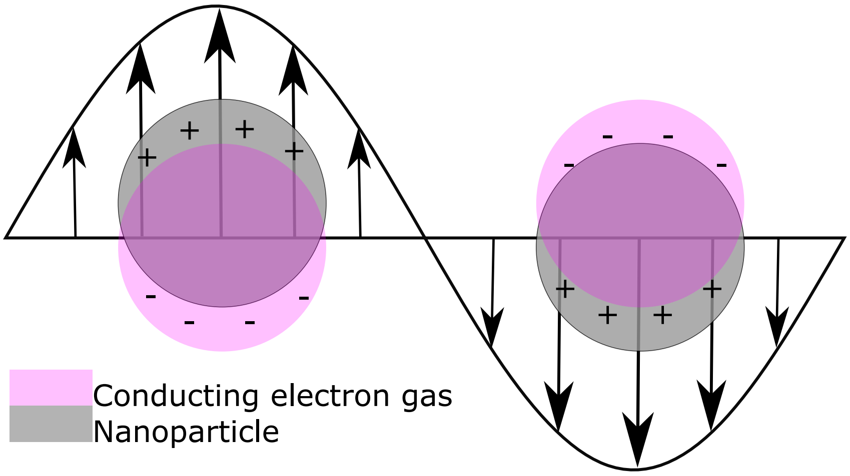

Figure 2.9. Spherical nanoparticle in an external electric field. The conducting electron gas is shifted and oscillates with the electrical field. The oscillating charge distribution of the nanoparticle gives rise to a dipole moment.

In 1908, Mie derived exact solutions to Maxwell's equations for spherical particles of any size given by

$$\nabla \times \mathbf{H} = \mathbf{J} + \frac{\partial \mathbf{D}}{\partial t}, \tag{2.18}$$

$$\nabla \times \mathbf{E} = -\mu_0 \mu \frac{\partial \mathbf{H}}{\partial t}, \tag{2.19}$$

$$\nabla \cdot \mathbf{D} = \rho, \tag{2.20}$$

$$\nabla \cdot \mathbf{B} = 0, \tag{2.21}$$

where **H** is the magnetic field, **J** is the current density, **D** is the displacement field, **E** is the electric field, **B** is the induction field, ρ is the charge density, and $\mu_0\mu$ is the magnetic permeability. As mentioned earlier, the optical properties of NPs depend on several parameters and thus it is of interest to investigate simple theoretical solutions which give an approximate expression for the extinction cross section of a NP with respect to Mie's solutions[30].

2.3.1 The Dipole Approximation

When considering small spherical NPs, it is possible to make use of the quasi-static dipole approximation which assumes that the electrons oscillate in phase and that they neglect any retardation effects which leads to a homogeneous electric field inside the metal NP as illustrated in Fig. 2.10. This is opposed to Gauss' law which states that there is no electric field inside a metal and as such, when the particle becomes larger, the approximation falls apart. The quasi-static approach starts out with finding an expression for the electric field inside and outside of the NP, given by the negative gradient of the potential $\mathbf{E} = -\nabla\phi$, where the potential ϕ can be determined from the Poisson equation[31]. For the case of a metal particle, this reduces to the Laplace's equation since the charge density ρ vanishes inside the metal as it is neutrally charged:

$$\nabla^2\phi(x,y,z) = -\frac{\rho}{\epsilon} = 0, \tag{2.22}$$

where ϵ is the permittivity. In spherical coordinates, this becomes

$$\nabla^2\phi(r,\theta,\varphi) = \frac{1}{r^2}\frac{\partial}{\partial r}\left(r^2\frac{\partial\phi}{\partial r}\right) + \frac{1}{r^2\sin(\theta)}\frac{\partial}{\partial\theta}\left(\sin(\theta)\frac{\partial\phi}{\partial\theta}\right) + \frac{1}{r^2\sin^2(\theta)}\frac{\partial^2\phi}{\partial\varphi^2} = 0. \tag{2.23}$$

As the sphere is rotationally symmetric, ϕ is independent of the azimuthal angle φ, and Eq. (2.23) only depends on the radial coordinates r and the zenith angle θ which can be separated into variables, i.e. $\phi(r,\theta) = Z(r)P(\theta)$. Inserting this into Eq. (2.23), multiplying by r^2 and dividing by $Z(r)P(\theta)$ yields

$$\frac{1}{Z(r)}\frac{\mathrm{d}}{\mathrm{d}r}\left(r^2\frac{\mathrm{d}Z(r)}{\mathrm{d}r}\right) = -\frac{1}{P(\theta)\sin(\theta)}\frac{\mathrm{d}}{\mathrm{d}\theta}\left(\sin(\theta)\frac{\mathrm{d}P(\theta)}{\mathrm{d}\theta}\right). \tag{2.24}$$

Both sides must be equal to a constant k as the left-hand side is only a function of r and the right-hand side is only a function of θ. Substituting the left-hand side for k and multiplying both side by $P(\theta)$ yields

$$\frac{1}{\sin(\theta)}\frac{\mathrm{d}}{\mathrm{d}\theta}\left(\sin(\theta)\frac{\mathrm{d}P(\theta)}{\mathrm{d}\theta}\right) + kP(\theta) = 0. \tag{2.25}$$

By introducing a change of variables $w = \cos(\theta)$, Eq. (2.25) becomes:

$$\frac{\mathrm{d}P(\theta)}{\mathrm{d}\theta} = \frac{\mathrm{d}P(\theta)}{\mathrm{d}w}\frac{\mathrm{d}w}{\mathrm{d}\theta} = -\sin(\theta)\left(\frac{\mathrm{d}P(\theta)}{\mathrm{d}w}\right) \Rightarrow -\frac{\sin(\theta)}{\sin(\theta)}\frac{\mathrm{d}}{\mathrm{d}w}\left(-\sin^2(\theta)\frac{\mathrm{d}P(\theta)}{\mathrm{d}w}\right) + kP(\theta) = 0. \tag{2.26}$$

Using that $\cos^2(\theta)+\sin^2(\theta) = w^2+\sin^2(\theta) = 1$, and substituting $n(n+1) = k$ (n=0,1,2,...), Eq. (2.26) becomes the Legendre differential equation:

$$\frac{\mathrm{d}}{\mathrm{d}w}\left(\left(1-w^2\right)\frac{dP(\theta)}{\mathrm{d}w}\right) + n(n+1)P(\theta) \tag{2.27}$$

$$= (1-w^2)\frac{\mathrm{d}^2P(\theta)}{\mathrm{d}w^2} - 2w\frac{\mathrm{d}P(\theta)}{\mathrm{d}w} + n(n+1)P(\theta) = 0. \tag{2.28}$$

The solutions for Eq. (2.28) are the Legendre polynomials $P_n(\cos\theta)$[31]. Finding the solution to the left-hand side of Eq. (2.23) is done in a similar manner by using the constant $k = n(n+1)$:

$$\frac{\mathrm{d}}{\mathrm{d}r}\left(r^2\frac{\mathrm{d}Z_n}{\mathrm{d}r}\right) - n(n+1)Z_n = 0, \tag{2.29}$$

where Z_n has two possible forms:

$$Z_n = r^n, \qquad Z_n = r^{-(n+1)}. \tag{2.30}$$

Combining these two solutions presents a general solution to the form of the potential given by

$$\phi(r,\theta) = \sum_{n=0}^{\infty}\phi_n(r,\theta) = \sum_{n=0}^{\infty}\left(A_n r^n P_n(\theta) + B_n r^{-(n+1)}P_n(\theta)\right), \tag{2.31}$$

where A_n and B_n are constants which are to be determined through the initial conditions as well as boundary conditions[31].

The distortion of an electric field around a metal NP is illustrated in Fig. 2.10. If the wavelength of the incident light is much large than the size of the particle, the applied electric field E_0 can be considered undistorted at large wavelengths.

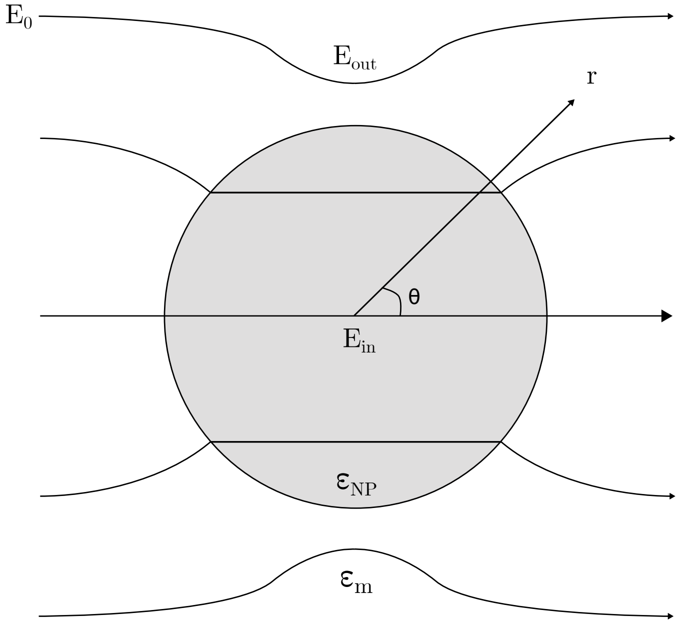

Figure 2.10. Distortion of the electric field around and inside a metal NP zenith angle θ and distance r from the center of the NP.

As such, for large distances from the particle, it is required that the electric field equals the external electric field and all terms with power greater than one must be zero. This boundary condition then implies than $A_n = 0$ for $n \geq 2$ and A_0 is neglected as it will disappear when taking the gradient to the potential. The particle has a neutral net charge and therefore the terms which contain r^{-1} must be zero as the potential would otherwise be the potential of a point charge. When $n \geq 2$, B_n must equal zero as the particle is assumed to be a dipole inside the particle and as such, the electric field must be uniform. The inside and outside potentials then become

$$\phi_{out} = A_{out} r \cos(\theta) + B_{out} r^{-2} \cos(\theta), \tag{2.32}$$

$$\phi_{in} = A_{in} r \cos(\theta) + B_{in} r^{-2} \cos(\theta). \tag{2.33}$$

Far from the dipole, the electric field is uniform and as such $\phi_{out} \to E_0 r \cos(\theta)$, meaning that $A_{out} = -E_0$. Likewise, $B_{in} = 0$ is required as the potential inside the particle would otherwise become infinite at the centre of the particle. The inside and outside potentials then reduce to:

$$\phi_{out} = -E_0 r \cos(\theta) + B_{out} r^{-2} \cos(\theta), \tag{2.34}$$

$$\phi_{in} = A_{in} r \cos(\theta). \tag{2.35}$$

The last constants A_{in} and B_{out} can be calculated from the boundary conditions that consider the fact that the NP is completely immersed in a dielectric. One boundary condition is that the potential must be continuous over the boundary, and the other is that the displacement field D must be continuous over the boundary as well given that there are no free charges on the surface of a dielectric[31]. Equating equations (2.34) and (2.35) and setting $r = a$, where a is the radius of the NP, yields

$$\left(-E_0 a + B_{out} a^{-2}\right) \cos(\theta) = A_{in} a \cos(\theta) \Rightarrow A_{in} = -E_0 + B_{out} a^{-3}. \tag{2.36}$$

Taking the displacement field as $\mathbf{D} = \epsilon \mathbf{E}$ in $r = a$ yields:

$$\epsilon_1 \left[\frac{\partial \phi_{in}}{\partial r}\right]_{r=a} = \epsilon_m \left[\frac{\partial \phi_{out}}{\partial r}\right]_{r=a} \tag{2.37}$$

$$\epsilon_1 \left(E_0 + B_{out} a^{-3}\right) = \epsilon_m \left(E_0 - 2B_{out} a^{-3}\right) \Rightarrow B_{out} = E_0 a^3 \frac{\epsilon_1 - \epsilon_m}{\epsilon_1 + 2\epsilon_m}. \tag{2.38}$$

where ϵ_1 and ϵ_m are the dielectric functions of the NP and the immersion medium, respectively. Inserting this expression for B_{out} into Eq. (2.36) gives

$$A_{in} = E_0 \frac{\epsilon_1 - \epsilon_m}{\epsilon_1 + 2\epsilon_m} - E_0 = E_0 \left(\frac{\epsilon_1 - \epsilon_m}{\epsilon_1 + 2\epsilon_m} - 1\right) = -E_0 \frac{3\epsilon_m}{\epsilon_1 + 2\epsilon_m}. \tag{2.39}$$

Inserting the expressions for A_{in} and B_{out} into equations (2.34) and (2.35), it is possible to calculate the electric field in terms of spherical coordinates by

$$\nabla f(r, \theta) = \frac{\partial f}{\partial r} \hat{r} + \frac{1}{r} \frac{\partial f}{\partial \theta} \hat{\theta}, \tag{2.40}$$

where $\hat{r}$ and $\hat{\theta}$ are the unit vectors. The electric field inside and outside then become

$$\mathbf{E}_{in} = -\nabla \phi_{in} = E_0 \frac{3\epsilon_m}{\epsilon_1 + 2\epsilon_m} (\hat{r} \cos(\theta) - \hat{\theta} \sin(\theta)), \tag{2.41}$$

$$\mathbf{E}_{out} = -\nabla\phi_{out} = E_0(\hat{r}\cos(\theta) - \hat{\theta}\sin(\theta)) + E_0\frac{a^3}{r^3}\frac{\epsilon_1 - \epsilon_m}{\epsilon_1 + 2\epsilon_m}(2\hat{r}\cos(\theta) + \hat{\theta}\sin(\theta)). \quad (2.42)$$

As $(\hat{r}\cos(\theta) - \hat{\theta}\sin(\theta)) = \hat{x}$, it can be seen that the field inside the NP is constant and homogeneous in the x-direction. Likewise, the outer field is represented by a field in the x-direction which is the constant external electric field but also a second term which describes the scattered field $\mathbf{E}_{scatter}$ from the NP. The scattered field can be described like the field of a dipole in the centre of the NP which is a function of the dipole moment $\mathbf{p} = \epsilon_m\alpha(\omega)E_0\hat{x}$ where $\alpha(\omega)$ is the polarisability[32]. As such, $\mathbf{E}_{scatter}$ can be described by:

$$\mathbf{E}_{scatter} = E_0\frac{a^3}{r^3}\frac{\epsilon_1 - \epsilon_m}{\epsilon_1 + 2\epsilon_m}(2\hat{r}\cos(\theta) + \hat{\theta}\sin(\theta)) = \frac{\mathbf{p}}{4\pi\epsilon_0\epsilon_m}\left(\frac{2\hat{r}\cos(\theta)}{r^3} + \frac{\hat{\theta}\sin(\theta)}{r^3}\right), \quad (2.43)$$

where the expression for the polarisability is:

$$\alpha(\omega) = 4\pi\epsilon_0 a^3\frac{\epsilon_1(\omega) - \epsilon_m}{\epsilon_1(\omega) + 2\epsilon_m}. \quad (2.44)$$

The dielectric properties of a metal is a function of the wavelength of the incident light and must therefore be taken into account. The polarisability describes how an external electric field will affect the NP.

2.3.2 The Radiating Dipole

This subsection will present the derivation of the extinction cross-section σ_{ext} of a NP particle which describes the total power removed from an incident electric field by a metal NP. The total power removed is the sum of the scattered and absorbed light, denoted by σ_{scatt} and σ_{abs}, respectively.

The Maxwell equation solutions obtained by Mie shows that the electric field which is scattered by a NP is that of a radiation dipole[30]. As such, the electric field of the dipole contributes to the extinction cross-section σ_{ext} through the scattering σ_{scatt}. The electric and magnetic field of a radiating dipole in spherical coordinates are given by

$$\mathbf{E}_r(t) = \frac{\cos(\theta)}{4\pi\epsilon_0\epsilon_m}\left[\frac{2}{r^2} + \frac{n_m}{c}\frac{2}{r^2}\frac{\mathrm{d}}{\mathrm{d}t}\right]|\mathbf{r}(t - n_m r/c)|, \quad (2.45)$$

$$\mathbf{E}_\theta(t) = \frac{\sin(\theta)}{4\pi\epsilon_0\epsilon_m}\left[\frac{1}{r^3} + \frac{n_m}{c}\frac{1}{r^2}\frac{\mathrm{d}}{\mathrm{d}t} + \frac{n_m^2}{c^2}\frac{1}{r}\frac{\mathrm{d}^2}{\mathrm{d}t^2}\right]|\mathbf{p}(t - n_m r/c)|, \quad (2.46)$$

$$\mathbf{H}_\varphi(t) = \frac{\sin(\theta)}{4\pi\epsilon_0\epsilon_m}\sqrt{\frac{\epsilon_0\epsilon_m}{\mu_0\mu_m}}\left[\frac{n_m}{c}\frac{1}{r^2}\frac{\mathrm{d}}{\mathrm{d}t} + \frac{n_m^2}{c^2}\frac{1}{r}\frac{\mathrm{d}^2}{\mathrm{d}t^2}\right]|\mathbf{p}(t - n_m r/c)|, \quad (2.47)$$

where n_m is the refractive index of the surrounding medium, c is the speed of light in vacuum, $\mu_0\mu_m$ is the permeability of the surrounding medium and t is time.

The total radiated power of the dipole can be found by the use of the Poynting vector $\mathbf{S}$ which describes the total local energy flow per unit time. As such, the time average of the Poynting vector is used to determine the average radiated power. The Poynting vector can normally be calculated by $\mathbf{S}_{scatt} = \mathbf{E}(t) \times \mathbf{H}(t)$. For a radiating dipole, however, only the far field terms (r^{-1}) describes the net transport of energy as the terms for the near-field (r^{-3}) and intermediate-field (r^{-2}) fall off quickly and as such can be omitted. Thus, the Poynting vector can be calculated as

$$\mathbf{S}(t) = \mathbf{E}_\theta(t) \times \mathbf{H}_\varphi(t) = \frac{1}{16\pi^2\epsilon_0\epsilon_m}\frac{\sin^2(\theta)}{r^2}\frac{n_m^3}{c^3}\left[\frac{\mathrm{d}^2}{\mathrm{d}t^2}\left|\mathbf{p}(t - n_m r/c)\right|\right]^2 \hat{r}. \tag{2.48}$$

Given that the dipole oscillates harmonically, the dipole moment can be written as $\mathbf{p}(r,t) = \mathrm{Re}\left[\mathbf{p}(r)\exp(-i\omega t)\right]$. Inserting this expression into Eq. (2.48) and integrating over the closed spherical surface yields the radiated power P:

$$P_{scatt} = \oint_{\delta V} \mathbf{S}_{scatt} \cdot \hat{r}\mathrm{d}A$$

$$= \int_0^{2\pi} \mathrm{d}\varphi \int_0^{\pi} \frac{1}{16\pi^2\epsilon_0\epsilon_m}\frac{\sin^2(\theta)}{r^2}\frac{n_m^3}{c^3}\left[\frac{\mathrm{d}^2}{\mathrm{d}t^2}\mathrm{Re}[\mathbf{p}(r)\exp(-i\omega t)]\right]^2 r^2\sin(\theta)\hat{r}\cdot\hat{r}\mathrm{d}\theta$$

$$= \frac{1}{4\pi\epsilon_0\epsilon_m}\frac{2n_m^3}{c^3}\left|\omega^2\mathbf{p}(r)\cos(\omega t)\right|^2. \tag{2.49}$$

Taking the time average of Eq. (2.49) gives:

$$\langle P_{scatt}\rangle = \frac{1}{6\pi\epsilon_0\epsilon_m}\frac{n_m^3}{c^3}\left|\omega^2\mathbf{p}(r)\right|^2\frac{1}{T}\int_0^T \left|\cos(\omega t)\right|^2\mathrm{d}t = \frac{\omega^4}{12\pi\epsilon_0\epsilon_m}\frac{n_m^3}{c^3}\left|\mathbf{p}(r)\right|^2. \tag{2.50}$$

The scattering cross section can then be found by dividing Eq. (2.50) by the time average of the Poynting vector. The time average of the Poynting vector of the incident light can be calculated similarly to that of the scattered field using the general formula [32]

$$\langle\mathbf{S}_{inc}\rangle = \frac{1}{2}\mathrm{Re}(\mathbf{E}\times\mathbf{H}^*), \tag{2.51}$$

where $\mathbf{H}^*$ is the complex conjugate of $\mathbf{H}$. The incident light which is a plane wave is given by an electric and a magnetic component where both can be expressed through the electric component. This is done by[31]:

$$\mathbf{E}(\mathbf{r},t) = \mathbf{E_0}\exp(i(\mathbf{k}\cdot\mathbf{r} - \omega t)) \tag{2.52}$$

$$\mathbf{H}(\mathbf{r},t) = \frac{\mathbf{k}}{\omega\mu_0\mu_m}\times\mathbf{E}_0\exp(i(\mathbf{k}\cdot\mathbf{r} - \omega t)). \tag{2.53}$$

Inserting equations (2.52) and (2.53) into Eq. (2.51) then yields:

$$\langle\mathbf{S}_{inc}\rangle = \frac{1}{2}\mathrm{Re}\left[\mathbf{E_0}\exp(i(\mathbf{k}\cdot\mathbf{r} - \omega t))\times\left(\frac{\mathbf{k}}{\omega\mu_0\mu_m}\times\mathbf{E}_0\exp(-i(\mathbf{k}\cdot\mathbf{r} - \omega t))\right)\right]. \tag{2.54}$$

Using the triple product rule $\mathbf{a}\times(\mathbf{b}\times\mathbf{c}) = \mathbf{b}(\mathbf{a}\cdot\mathbf{c}) - \mathbf{c}(\mathbf{a}\cdot\mathbf{b})$ yields:

$$\langle\mathbf{S}_{inc}\rangle = \frac{1}{2}\mathrm{Re}\left(\frac{\mathbf{k}}{\omega\mu_0\mu_m}\left|\mathbf{E}_0\right|^2\right) = \frac{\mathbf{k}}{2\omega\mu_0\mu_m}\left|\mathbf{E}_0\right|^2. \tag{2.55}$$

Considering the magnitude of this vector and using the magnitude for the wave vector $k = \omega n_m/c$, Eq. (2.55) becomes

$$\langle \mathbf{S}_{inc} \rangle = \frac{n_m}{2c\mu_0\mu_m} \left|\mathbf{E}_0\right|^2 . \tag{2.56}$$

Calculating the scattering cross-section is then done by dividing Eq. (2.50) with Eq. (2.56):

$$\sigma_{scatt} = \frac{\langle P_{scatt} \rangle}{\langle \mathbf{S}_{inc} \rangle} = \left(\frac{\omega^4}{12\pi\epsilon_0\epsilon_m} \frac{n_m^3}{c^3} \left|\mathbf{p}(r)\right|^2 \right) \Big/ \left(\frac{n_m}{2c\mu_0\mu_m} \left|\mathbf{E}_0\right|^2 \right) \tag{2.57}$$

$$= \frac{\omega^4 n_m^2 \mu_0\mu_m}{6\pi\epsilon_0\epsilon_m c^2} \frac{\left|\mathbf{p}(r)\right|^2}{\left|\mathbf{E}_0\right|^2}. \tag{2.58}$$

Substituting back to k as well as using the expression for the refraction index $n_m = \sqrt{\epsilon_m\mu_m}$ and the fact that $c = 1/\sqrt{\epsilon_0\mu_0}$ and lastly using the expression for the dipole moment $\mathbf{p} = \epsilon_m \alpha(\omega) E_0 \hat{x}$, the scattering cross-section becomes:

$$\sigma_{scatt} = \frac{k^4}{6\pi\epsilon_0^2} \left|\alpha(\omega)\right|^2 . \tag{2.59}$$

In order to calculate the extinction cross-section which is the sum of the absorption cross-section and scattering cross-section, the absorption cross-section is needed. Similarly to the scattering cross-section, the absorption cross-section is found by dividing the absorbed power with the intensity of the incident light $\langle \mathbf{S}_{inc} \rangle$. The absorbed power is found through Poynting's theorem:

$$\langle P_{abs} \rangle = -\frac{1}{2} \int_V \mathrm{R}(\mathbf{j}^* \cdot \mathbf{E}_0) \mathrm{d}V, \tag{2.60}$$

where $\mathbf{j}$ is the current density and V is the volume of the spherical NP. Considering only the lowest-order terms of a radiating dipole, the current density can be written as[32]:

$$\mathbf{j}(\mathbf{r}, t) = \frac{\mathrm{d}}{\mathrm{d}t} \mathbf{p}(t) \delta^3(\mathbf{r} - \mathbf{r}_0), \tag{2.61}$$

where $\mathbf{r}_0$ is the centre of the oscillating dipole and δ is the Dirac delta function. The dipole is still approximated to be oscillating harmonically and as such can be split into two parts $\mathbf{p}(\mathbf{r}, t) = \mathrm{Re}\left[\mathbf{p}(\mathbf{r}) \exp(-i\omega t)\right]$. This means the current density can be written as:

$$\mathbf{j}(\mathbf{r}, t) = -i\omega \mathbf{p}(\mathbf{r}, t) \delta^3(\mathbf{r} - \mathbf{r}_0). \tag{2.62}$$

This can be inserted into Eq. (2.61) to give

$$\langle P_{abs} \rangle = -\frac{1}{2} \int_V \mathrm{Re}\left(i\omega \mathbf{p}(\mathbf{r}, t) \delta^3(\mathbf{r} - \mathbf{r}_0) \cdot \mathbf{E}_0 \right) \mathrm{d}V \tag{2.63}$$

$$= -\frac{\omega}{2} \mathrm{Re}\left[i\mathbf{p} \cdot \mathbf{E}_0\right] = \frac{\omega}{2} \mathrm{Im}\left[\mathbf{p}(\mathbf{r}, t) \cdot \mathbf{E}_0\right]. \tag{2.64}$$

By dividing Eq. (2.64) by the magnitude of the Poynting vector of the incident light, Eq. (2.56), the absorption cross-section can be calculated:

$$\sigma_{abs} = \frac{\langle P_{abs} \rangle}{\langle \mathbf{S}_{inc} \rangle} = \frac{\frac{\omega}{2} \mathrm{Im}\left[\mathbf{p}(\mathbf{r}, t) \cdot \mathbf{E}_0\right]}{\frac{n_m}{2c\mu_0\mu_m} \left|\mathbf{E}_0\right|^2} = \frac{\omega c \mu_0 \mu_2}{n_m} \frac{\mathrm{Im}\left[\mathbf{p} \cdot \mathbf{E}_0\right]}{\left|\mathbf{E}_0\right|^2} \tag{2.65}$$

$$= \frac{k}{\epsilon_0}\text{Im}\left[\alpha(\omega)\right]. \tag{2.66}$$

As the sum of the absorption and scattering cross-sections, the extinction cross-section becomes:

$$\sigma_{ext} = \sigma_{scatt} + \sigma_{abs} = \frac{k^4}{6\pi\epsilon_0^2}\left|\alpha(\omega)\right|^2 + \frac{k}{\epsilon_0}\text{Im}[\alpha(\omega)]. \tag{2.67}$$

Given that $\alpha(\omega)$ scales with a^3, the scattering cross-section scales with a^6 while the absorption cross-section only scales with a^3, meaning that scattering will be more prominent for larger NPs. This means that for smaller NPs, the scattering cross-section can be omitted. Doing so and inserting Eq. (2.44) into Eq. (2.67), the extinction cross-section becomes

$$\sigma_{ext} = \frac{k}{\epsilon_0}\text{Im}\left[4\pi\epsilon a^3\frac{\epsilon_r + i\epsilon_i - \epsilon_m}{\epsilon_r + i\epsilon_i + 2\epsilon_m}\right], \tag{2.68}$$

where the dielectric function of the NP, $\epsilon_1(\omega)$, has been split into a real and imaginary part ϵ_r and ϵ_i, respectively. The imaginary part comes from the complex dielectric function $\epsilon(\omega) = \epsilon' + i\frac{\sigma}{\epsilon_0\omega}$, where σ is the conductivity of the material[32]. The refractive index of a material can be given by $n = n_r + ik_i$ and given that $\epsilon \approx n^2$, the real and imaginary parts of the dielectric function are commonly given by $\epsilon_r = n^2 - k_i^2$ and $\epsilon_i = 2nk_i$, respectively, where k_i is the imaginary part of the refractive index and n_r is the real part of the refractive index.

In order to find the resonance condition, and therefore the peak position with respect to wavelength, of the extinction cross-section, the denominator of the imaginary fraction in Eq. (2.68) must be considered. The fraction can be rationalised my multiplying both the numerator and denominator by the complex conjugate of the denominator:

$$\left(\frac{a+ib}{c+id}\right)\left(\frac{c-id}{c-id}\right) = \frac{(ac+bd)+i(bc-ad)}{c^2+d^2}. \tag{2.69}$$

Doing so to Eq. (2.68) gives:

$$\sigma_{ext} = \frac{k}{\epsilon_0}\text{Im}\left[4\pi\epsilon_0 a^3\frac{((\epsilon_r-\epsilon_m)(\epsilon_r+2\epsilon_m)+\epsilon_i^2)+i(\epsilon_i(\epsilon_r+2\epsilon_m)-\epsilon_i(\epsilon_r-\epsilon_m))}{(\epsilon_r+2\epsilon_m)^2+\epsilon_i^2}\right] \tag{2.70}$$

$$= \frac{k}{\epsilon_0}\left[4\pi\epsilon_0 a^3\frac{(\epsilon_i(\epsilon_r+2\epsilon_m)-\epsilon_i(\epsilon_r-\epsilon_m))}{(\epsilon_r++2\epsilon_m)^2+\epsilon_i^2}\right] \tag{2.71}$$

$$= \frac{12\epsilon_m\epsilon_i\pi k a^3}{(\epsilon_r+2\epsilon_m)^2+\epsilon_i^2}. \tag{2.72}$$

By inserting the wave number $k = 2\pi\sqrt{\epsilon_m}/\lambda$, where λ is the wavelength of the incident light, an expression for the the extinction cross-section is obtained:

$$\sigma_{ext} = \frac{24\epsilon_m^{3/2}\epsilon_i\pi^2 a^3}{\lambda((\epsilon_r+2\epsilon_m)^2+\epsilon_i^2)}. \tag{2.73}$$

By dividing with the cross-section of the particle, the effective extinction Q_{ext} is obtained:

$$Q_{ext} = \frac{24\epsilon_m^{3/2}\epsilon_i \pi a}{\lambda((\epsilon_r + 2\epsilon_m)^2 + \epsilon_i^2)}. \tag{2.74}$$

This parameter is unitless and describes how efficiently a spherical particle extinguishes radiation depending on its size, its complex index of refraction, and the dielectric medium that surrounds it. The effect of the surrounding dielectric medium can be seen in Fig. 2.11 where Eq. (2.74) has been simulated for silver with surrounding mediums of air and PMMA, respectively.

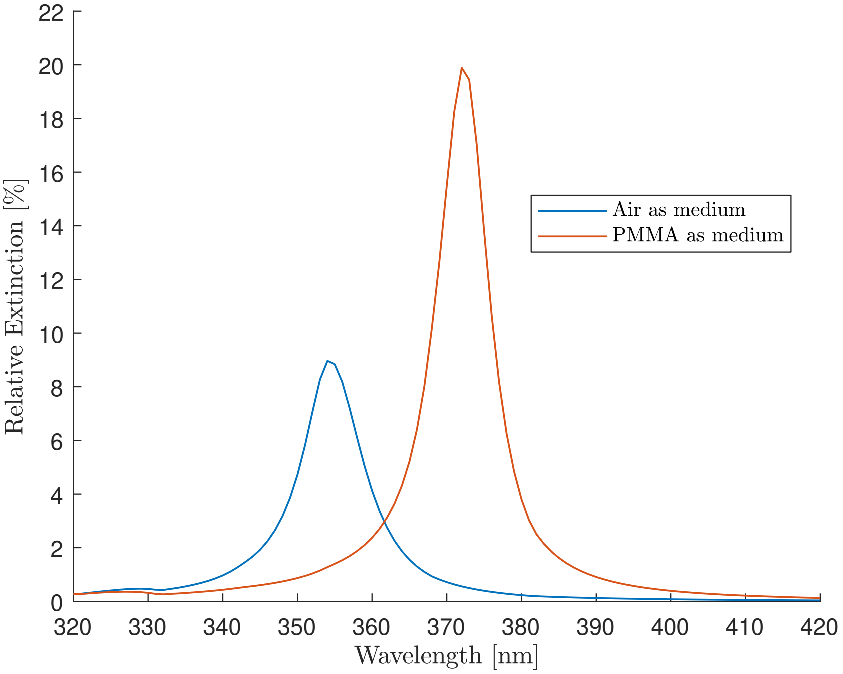

Figure 2.11. Extinction cross-section calculated using Eq. (2.74) for a silver sphere with air (blue) and PMMA (red) as its surrounding medium, respectively. The dielectric data of silver have been taken from [33].

2.3.3 Substrate Effect on Refractive Indices

The effective extinction Q_{ext} of a particle depends on the dielectric medium that surrounds it. The NP, however, might not be surrounded by a single dielectric medium, and as such it is convenient to describe the surrounding dielectric mediums as a single dielectric medium. This is the case in this project, where NPs of Ag or Cu are deposited on quartz and/or PMMA substrates. The surrounding medium can therefore be considered as a mixture between the underlying substrate and the surrounding air as illustrated in Fig. 2.12.

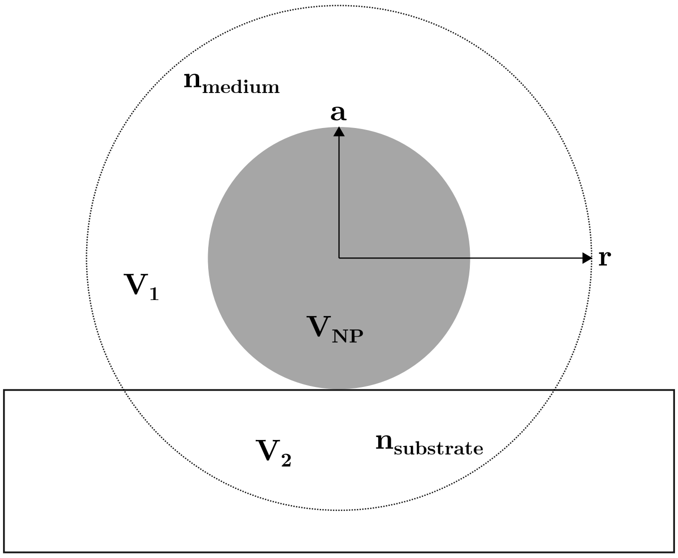

Figure 2.12. Illustration of the effective medium around a spherical nanoparticle resting on top of a substrate with a surrounding medium with sensing range of the shell being $(r - a)$ from the surface of the nanoparticle.

Following the example of Curry et al[34], it is possible to define a weighting factor β which describes the total influence on the SPR peak wavelengths from the medium and substrate collectively[34]. The effective refractive index is

$$n_{eff} = \beta n_m + (1 - \beta) n_{substrate}, \tag{2.75}$$

where n_m is the refractive index of the immersion medium and $n_{substrate}$ is the refractive index of the substrate on which the particle is deposited. This expression squared can then be used for ϵ_m in Eq. (2.74). Assuming that the sensing volume is a shell with uniform sensitivity the weighting factor is:

$$\beta = \frac{V_m}{V_{tot} - V_{NP}}, \tag{2.76}$$

where V_m is the volume of the immersion medium, V_{tot} is the volume of the sensing sphere, and V_{NP} is the volume of the NP.

2.4 Degradation of Localised Surface Plasmon Resonance

The applications of LSPR is under rapid development [2][3][35]. As can be seen from Eq. (2.67), the scattering of a NP can be neglected for particles with $a << \lambda$ as it scales with $(a/\lambda)^4$ compared to the absorption which scales with (a/λ) and as is typically stronger in the visible range. The resonance can be utilised in sensing and the absorption also enhances the strongly confined field which can be used to enhance or manipulate optical response from nearby molecules as for instance in surface enhanced Raman spectroscopy (SERS)[36]. Noble metals, and especially gold, have been widely used in plasmon resonance applications. Silver has a larger optical cross section[9], a lower cost than gold, and is much more abundant and as such would be attractive to use in place of gold. As such, silver has drawn a lot of attention but that it corrodes easily, degrading its plasmonic properties, thus limiting its applications[9]. Due to its excellent plasmonic properties but quick degradation, silver has garnered a lot of attention in recent years[9]. The degradation effect is particularly enhanced on the nanoscale due to the larger surface-to-volume ratio. More specifically, Ag is more easily affected by ambient species such as O_2 or H_2S, causing silver oxide or silver sulfide to form on the surface of the NPs[36]. Several studies have been carried out to determine whether the main cause of degradation of silver is caused by reaction with oxygen or sulfur in the ambient atmosphere but as of yet, neither can be excluded as the main culprit of degradation. Cao et al[37] investigated the stability of Ag NPs under atmospheric condition and vacuum conditions, respectively. The study found that the NPs kept under atmospheric conditions showed concentrations of sulfur and also morphological changes, as well as increased concentrations of oxygen. The study by Oates et al [38] found that silver films stored in an ambient atmosphere show no signs of silver sulfide while silver oxide was observed. In contrast, studies by Novikov et al[29] and Scuderi et al[39] suggest that oxidation does in fact not play a large role in the degradation of the LSPR bands of silver NPs and as such is caused by other atmospheric or sulphurous species, respectively.

Copper also exhibit great plasmonic properties and as such can also serve for the methods mentioned above. Copper, however, also suffers from degradation due to contamination from ambient species. Copper NPs are particularly affected by atmospheric oxygen in the ambient atmosphere, constructing copper-oxides[10][40][41].

Several methods have been suggested in order to avoid the degradation of Ag and Cu NPs, most of which consist of making a protective layer around the NPs. Examples of such protective layers include the fabrication of a very thin layer of Au, creating an Ag-Au core/shell nanostructure[42][43], passivating Ag NPs with a self-assembled monolayer of hexanethiols[39], transferring a few layers of graphene on top of either Ag or Cu films[44][45], silica-coating of Ag NPs[46], AgCu alloy NPs with graphene coating[9], and possibly the formation of a continuous oxide shell around Cu NPs by the use of UV-ozone treatment[23].

Chapter 3

Experimental Details

3.1 Sample Preparation

The experimental purpose of this project is to investigate the degradation of LSPR of Ag and Cu NPs over time depending on the size of the NPs, the atmosphere in which they are kept, and the substrate the NPs have been deposited on. Three sizes of NPs are selected for deposition, applying voltages of 200, 600 and 1200 V to the EQMS (see details below). Two types of substrates, namely, quartz and quartz spin-coated by poly(methyl methacrylate) (PMMA) film are used in the experiments. After deposition, the substrates with NPs are stored either in an ambient atmosphere or in a special hermetic box with continuous flow of N_2 pushing out ordinary air, respectively, in order to investigate the degradation depending on the atmospheric environment in which the NPs are stored.

3.1.1 Spin-coating of PMMA

For the formation of PMMA films, the quartz samples were cleaned in an ultra-sonic bath and subsequently wiped off. Next, PMMA was spun-coated on the samples using a 1.5 % solution of PMMA. Spin-coating was performed at 2000 RPM for 2 minutes. The thickness of the PMMA layer was then investigated using AFM by making a slight scratch in the PMMA layer down to the substrate and measuring the depth of the trench. It was confirmed to be roughly 100 nm thick.

3.1.2 Cluster Deposition Set-up

For the production and deposition of the size-selected Ag and Cu clusters on the substrates, a MaSCA as seen in Fig. 3.1 was used. The MaSCA consists of four main chambers: the source chamber, the ion optics chamber, the electrostatic quadrupole mass selector (EQMS) chamber, and the deposition chamber. The setup is equipped with four turbomolecular pumps (from 230-1250 l/s) which are backed by fore-vacuum pumps, all of which are provided from Pfeiffer Vacuum. By the use of differential pumping, a background pressure of up to 5.0×10^{-8} mbar is achievable in the source chamber. To measure the pressure inside the chambers, two ion gauges are installed. For the separation of the ion optics chamber and then EQMS chamber, a pneumatic UHV gate valve with a leak rate of less than 1×10^{-10} Torr l/s has been installed.

A commercial source (NC200U, Oxford Applied Research) was utilised in the production of the metal clusters.

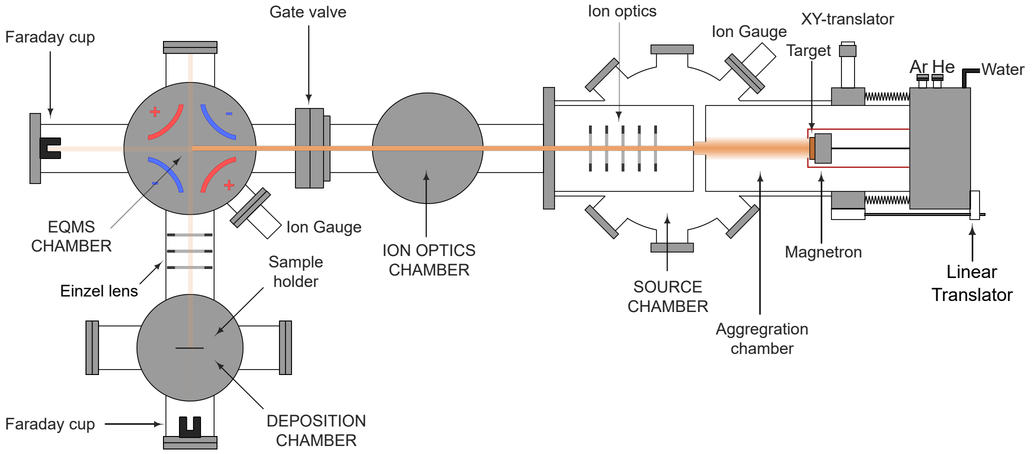

Figure 3.1. Schematic view of the MaSCA.

In the aggregation chamber, seen in Fig. 2.8, an Ag or Cu target of 99.99 % purity is sputtered with argon ions, clusters form and aggregate and are then expanded into the source chamber through the nozzle. In the source chamber, the clusters are collimated into a beam through a conically shaped skimmer, after which they are directed into the EQMS chamber. There are also ion optics inside the source chamber to direct the path of the cluster beam. The clusters produced in the source are of different sizes with a significant fraction of them being ionized which allows for mass/size selection by the use of electrostatic fields [23][47]. As such, it is possible to divert the path of the beam of ions depending on the mass and charge of the particles through the use of an EQMS.

Electrostatic Quadrupole Mass Selector

The clusters are size(mass)-selected in the EQMS. The EQMS uses a quadrupole potential consisting of four hyperbolic electrodes as described by Hartmann et al[20]. The electrodes are divided into two pairs which are biased with the same absolute voltages albeit with opposite polarities. The electrodes are surrounded by a grounded shield with circular orifices which allow the cluster beam to move into the EQMS. An electric potential (U_{QP}) is applied to the electrodes which creates a hyperbolical equipotential field, causing the cluster to deflect depending on the particles charge/mass ratio. Specifically, the deflection depends on the balance between the kinetic energy of the electrostatic field. The energy (E) needed to deflect a cluster by 90° at a given U_{QP} is

$$E = qU_{QP}, \tag{3.1}$$

where q is the particle charge. This energy must equal the kinetic energy of the particle, leading to the relation

$$\frac{m}{q} = \frac{2U_{QP}}{v^2}. \tag{3.2}$$

As the shapes of the quadrupoles are not completely hyperbolic, a correction constant must be applied to the potential energy[20]. The correction value presented in Hartmann et al[20] suggested the broadening of

$$E = (1.72 \pm 0.19) qU_{QP}. \tag{3.3}$$

The above description is based on ideal conditions where particle are assumed to be of the same charge, velocity and the beam is adjusted exactly along the main axes.

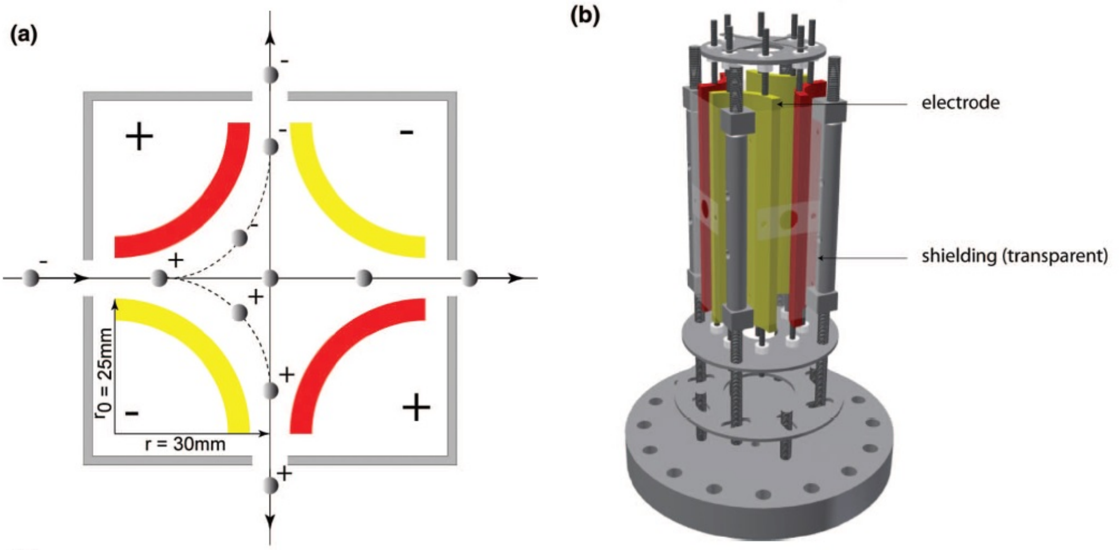

Figure 3.2. (a) Cross-sectional view of the EQMS with included trajectories for positive, negative and neutral clusters, respectively. (b) Pseudo 3D schematic view of the EQMS. Adopted from Hartmann et al[20]

Experiments with silver have demonstrated standard deviation of particle diameters within 7 % being achieved for optimized EQMS parameters [48]. The cluster mean height for different voltages can be found by the use of AFM imaging and can be seen in Fig. 3.3.

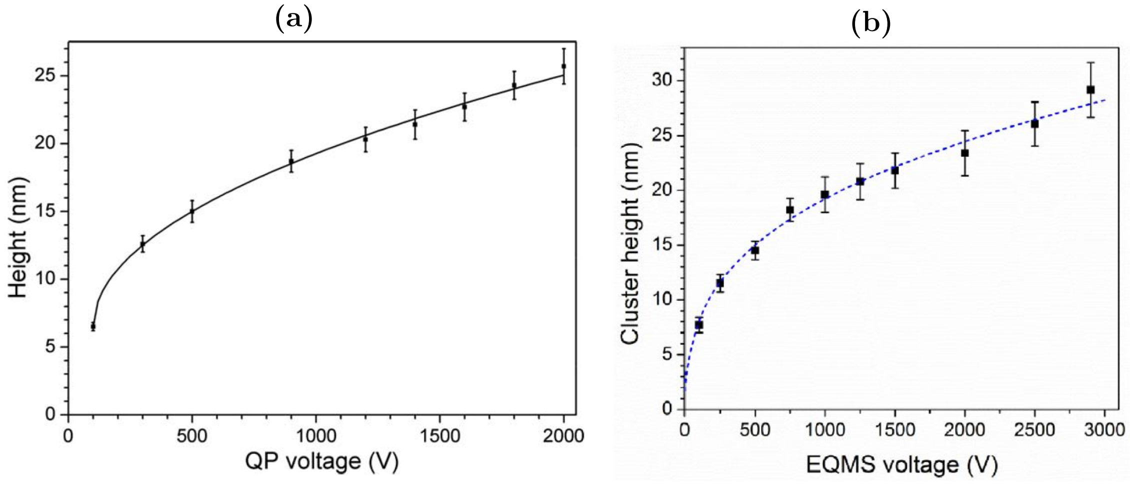

Figure 3.3. Cluster mean height for different voltages for (a) Ag NPs and (b) Cu NPs. Error bars show standard deviations. V is the numerical size of the voltage applied to the electrodes in the quadrupole. Adopted from [48] and [23], respectively.

In the undiverted cluster beam path, a Faraday cup is placed in the quadrupole chamber. When no voltage is applied to the quadrupole, this allows for measurement of the cluster beam intensity. When voltage has been applied to the EQMS, particles are deflected and directed into the deposition chamber. Likewise, a Faraday cup is placed in the deposition chamber behind the sample holder. Between the EQMS chamber and the deposition chamber, an Einzel lens is placed in order to focus or defocus the cluster beam, allowing for the particles to be deposited in a more controlled manner.

3.1.3 UV-Ozone Treatment

Some of the samples in this project were also subjected to UV-ozone (UV-O_3) treatment. UV-ozone treatment is a dry-cleaning method which is particularly effective at removing organic contaminants. The working principle of UV-ozone treatment is to convert organic compounds into volatile substances such as water, carbon dioxide or nitrogen by decomposition by ultraviolet rays and strong oxidation during the formation and decomposition of O_3[49]. Two major wavelengths of ultraviolet rays are applied at 184.9 nm and 253.7 nm. When atmospheric oxygen O_2 is irradiated with rays of wavelength 184.9 nm, the oxygen absorbs the ray, generating O_3 by the following reaction

$$\mathrm{O_2} \rightarrow \mathrm{O} + \mathrm{O}$$
$$\mathrm{O} + \mathrm{O_2} \rightarrow \mathrm{O_3}$$

Ozone O_3 irradiated with rays at wavelength 253.7 nm then absorbs the ultraviolet light to decompose the O_3. During formation and decomposition of O_3, atomic oxygen O having a strong oxidizing ability is generated which in turn interacts with surface contaminants. Aside from the cleaning of organic materials from a substrate, UV-ozone treatment also has the effect of being oxidizing materials[49], which is the main purpose of subjecting the samples in this project to the treatment. This is done in order to investigate how the Ag and Cu NPs are affected by a rapid oxidation.

3.2 Characterisation of Deposited Clusters

The clusters deposited on the substrates were studied by the use of atomic force microscopy (AFM) and optical spectroscopy. A brief description of the two methods as well as modes of operations and techniques are given below.

3.2.1 Atomic Force Microscopy

In order to study the size and the coverage of the deposited clusters, AFM was applied. An NTEGRA in conjunction with associated software from NT-MDT Spectrum Instruments was used. AFM has several modes of operation, the most common modes being *contact*, *semi-contact/tapping*, and *non-contact*. In this project, the tapping mode under ambient conditions was applied. Silicon bodied, poly-silicon levers and silicon high resolution tips with Au reflective coating and tip curvature of ≤10 nm and resonance frequencies between 140 and 235 kHz from ScanSens were used.

3.2.2 Optical Spectrometry

In order to investigate the degradation of the LSPR over time, optical spectrometry was used on the samples. The optical spectrophotometer used in this project was a Lambda 1050 UV/VIS/NIR together with PerkinElmer UV Winlab software version 6.0.4. from PerkinElmer. Measurements were carried out in double beam transmittance mode. In the first step, a reference beam is directed directly into a photodetector in order to collect the transmittance value corresponding to 100 % transmittance over the selected range of wavelength. Next, a sample is inserted into the sample holder and the beam is now directed through the sample before it it encounters the photodetector. The relative transmittance through the sample compared to the reference beam is then calculated for the entire wavelength spectra. As the Ag and Cu NPs are deposited on both pure quartz and quartz-PMMA substrates, baselines for both ($T_{\text{substrate}}$) without NPs are taken in order to calculate the loss in transmission called the relative extinction. The relative extinction is calculated by

$$A_{\text{rel}} = (1 - T_{\text{subtrate+NP}}) - (1 - T_{\text{substrate}}). \tag{3.4}$$

Note that A_{rel} constitutes both absorption and scattering of light. The spectra for the Cu NPs were collected in the 350-800 nm wavelength interval while the spectra for the Ag NPs were collected in the 320-750 nm wavelength interval. During the first week after deposition of NPs, measurements were made each consecutive day with approximately 24 hour intervals in order to investigate the immediate changes. Afterwards the initial week had passed, measurements were taken in 7 day intervals.

3.3 Sample Overview

This section presents a brief overview of the samples, including the filtering voltage V_q applied to the EQMS during deposition, the atmosphere they were kept in, and if and how long they have been subjected to the UV-ozone treatment.

Table 3.1. Quartz samples with Ag NPs deposited with voltages V_q applied to the EQMS. Additionally, pairs were kept in different atmospheric conditions and some were ozonated.

Sample	V_q	Atmosphere	Ozonation
Q_1	200 V	Ambient	None
Q_2	200 V	Nitrogen	None
Q_5	600 V	Ambient	None
Q_6	600 V	Nitrogen	None
Q_3	1200 V	Ambient	None
Q_4	1200 V	Nitrogen	None
Q_7	1200 V	Nitrogen	40 min
Q_8	1200 V	Ambient	40 min

Table 3.2. PMMA samples with Ag NPs deposited with voltages V_q applied to the EQMS. Additionally, pairs were kept in different atmospheric conditions.

Sample	V_q	Atmosphere	Ozonation
P_3	200 V	Ambient	None
P_4	200 V	Nitrogen	None
P_7	600 V	Ambient	None
P_8	600 V	Nitrogen	None
P_5	1200 V	Ambient	None
P_6	1200 V	Nitrogen	None

Table 3.3. Quartz samples with Cu NPs deposited with voltages V_q applied to the EQMS. Additionally, pairs were kept in different atmospheric conditions and some were ozonated

Sample	V_q	Atmosphere	Ozonation
C_5	600 V	Nitrogen	30 min
C_6	600 V	Ambient	30 min
C_1	1200 V	Nitrogen	20 min
C_2	1200 V	Ambient	20 min
C_3	1200 V	Nitrogen	40 min
C_4	1200 V	Ambient	40 min
C_7	600 V	Nitrogen	None
C_8	600 V	Ambient	None
C_9	1200 V	Nitrogen	None
C_{10}	1200 V	Ambient	None

Chapter 4

Results and Discussion

This chapter will present and discuss the data obtained during the project. AFM measurements are carried out to verify the sizes of the NPs deposited at different filtering voltages. Optical measurements monitoring evolution of plasmon band on a long-time scale are performed and discussed.

4.1 AFM Imaging

AFM images for samples Q1, Q5, Q3, and Q7 which have silver particles deposited on quartz substrates can be seen in figures 4.1, 4.2, 4.3 and 4.4, while AFM images for samples C6 and C4 which have copper particles deposited on quartz substrates can be seen in figures 4.5 and 4.6, respectively. Obtaining meaningful AFM images of samples P3 through P8 with silver particles deposited on quartz-PMMA substrates was not possible. All samples appear to have below monolayer (ML) coverage, with the exception of Q3 which seemingly has higher than ML coverage. Likewise, all samples show that particles of varying sizes are deposited on them. Some NPs might be multiply charged, i.e. double or triple charge instead of single charge which NPs produced in a MaSCA setup commonly have. Some particles are much more abundant. Analysis of the height profiles of the most abundant and most extreme NPs on the samples are carried out in order to verify the sizes of the deposited NPs. The mean height of the most abundant NPs is designated $<h>$ and the mean height of the most extreme NPs is designated $<h_e>$.

Table 4.1. Average height $<h>$ and the most extreme $<h_e>$ of NPs on the samples.

Sample	Q1	Q5	Q3	C6	C4
Filtering voltage	200 V	600 V	1200 V	600 V	1200 V
$<h>$ [nm]	7.5	12.5	28.5	16.4	22.2
$<h_e>$ [nm]	17.0	28.3	65.6	43.1	53.7

Comparison of $<h>$ with Fig. 3.3(a) shows that NPs on samples Q1 and Q5 are smaller than the expected size, while Q3 have averagely larger NPs. The NPs on Q1 and Q5 might be smaller due to oblation and flattening of the NPs caused by the large difference in surface tension between quartz and silver which are $\gamma_{quartz} < 100$ mJ/m^2 and $\gamma_{Ag} \approx$ 1200 mJ/m^2, respectively[50]. To minimise the difference in the Gibbs free energy at the interface, a particle will tend to deform in order to increase the contact area, resulting in an oblate shape. In contrast, the NPs on Q3 are larger than the expectation. This can be related to the high coverage on this samples which makes it difficult to make precise measurements. Another possibility for deviations is high roughness of the quartz substrates. The measurements presented in Fig. 3.3 were done on flat Si surfaces with roughness below 0.3 nm. Due to the high coverage on this sample, the presence of these larger particles may be due to aggregation occurring after deposition.

Meanwhile, comparison of $<h>$ with Fig. 3.3(b) shows that NPs on samples C4 and C6 seem to have sizes very close to the expected ones of 16 and 20 nm, respectively, both being slightly larger than expected.

Following the SCA, the amount of atoms composing NPs of different sizes are calculated and presented in Tab. 4.2.

Table 4.2. Approximate amount of atoms per cluster calculated through the SCA for obtained average $<h>$.

Sample	Q1	Q5	Q3	C6	C4
Filtering voltage	200 V	600 V	1200 V	600 V	1200 V
$<h>$ [nm]	7.5	12.5	28.5	16.4	22.2
N	≈ 10,400	≈ 54,300	≈ 644,200	≈ 196,700	≈ 487,900

Obtaining meaningful AFM images of the ozonated samples with silver NPs was not possible. An AFM image of sample Q7 is shown in Fig. 4.4. As can be seen, the quality of the image is poor and there are massive pillars present, some of which are over 100 nm tall.

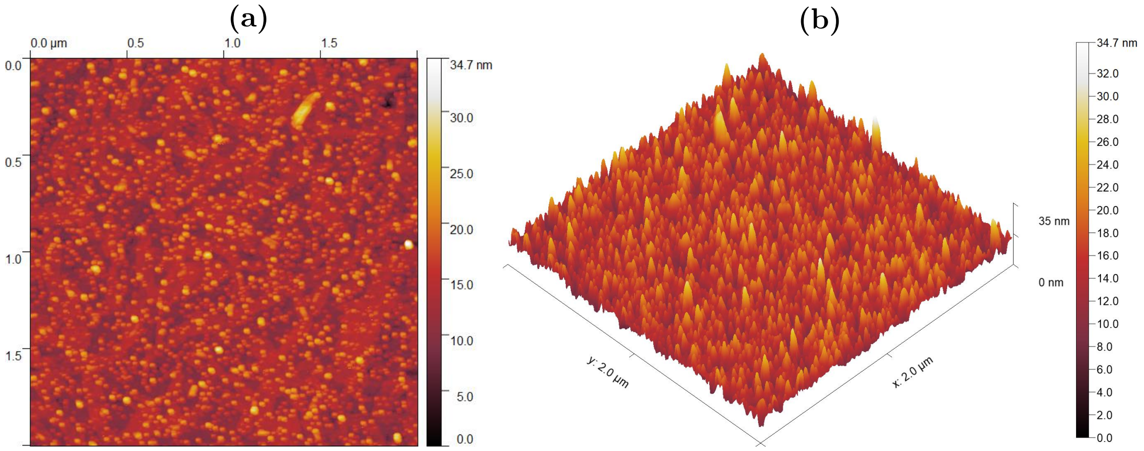

Figure 4.1. AFM image of sample Q1 (a) 2D and (b) 3D

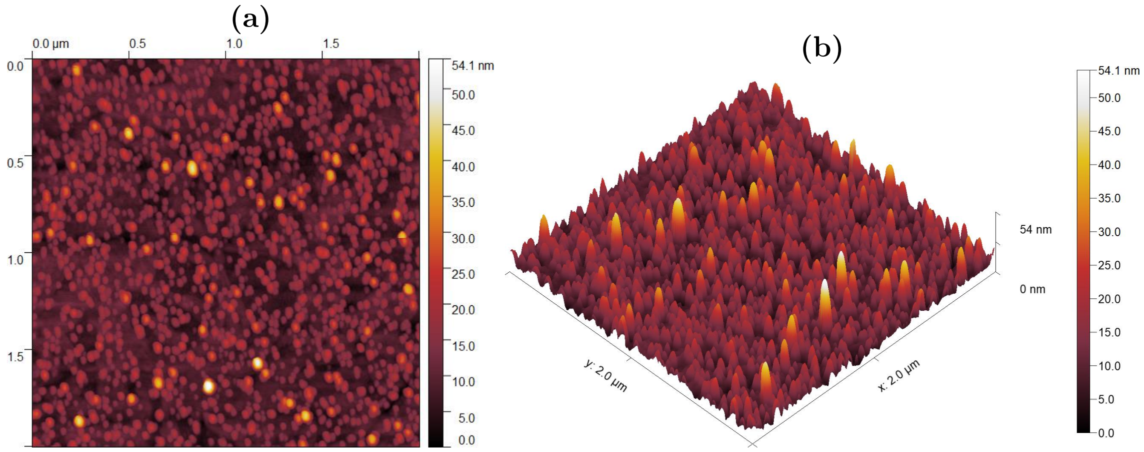

Figure 4.2. AFM image of sample Q5 (a) 2D and (b) 3D

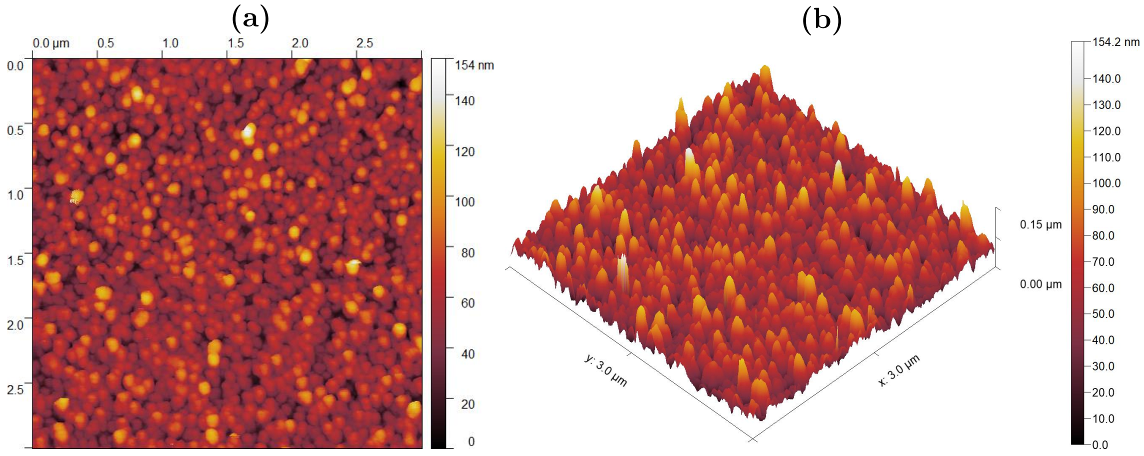

Figure 4.3. AFM image of sample Q3 (a) 2D and (b) 3D

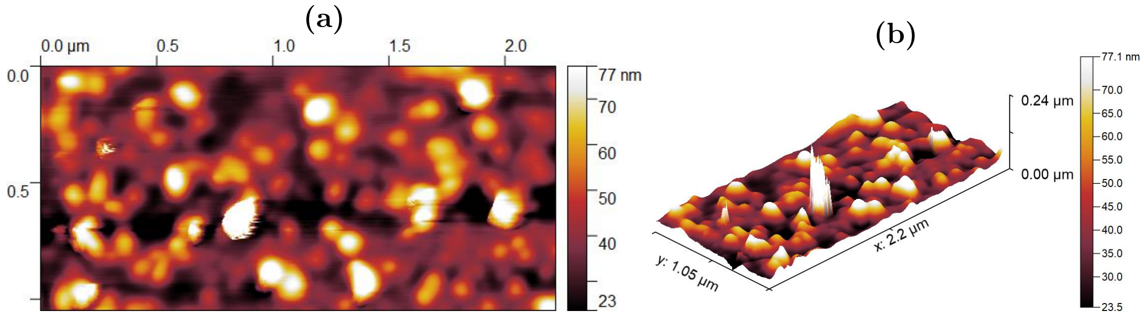

Figure 4.4. AFM image of sample Q7 (a) 2D and (b) 3D

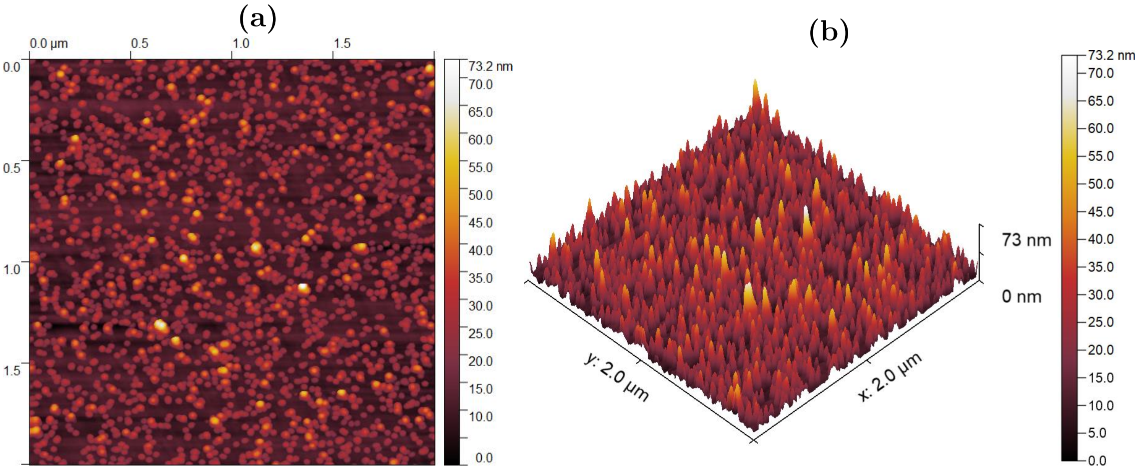

Figure 4.5. AFM image of sample C6 (a) 2D and (b) 3D

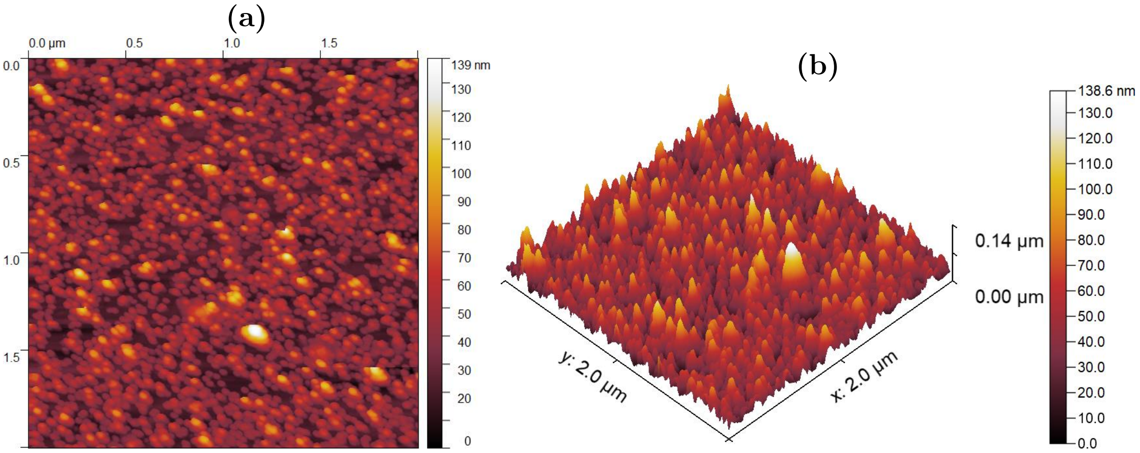

Figure 4.6. AFM image of sample C4 (a) 2D and (b) 3D

4.2 Evolution of Plasmonic Properties of Silver Nanoparticles on Quartz Substrates

This section discusses the evolution over time of the optical properties of the samples with differing sizes of Ag NPs deposited on pure quartz substrates. The samples are separated in pairs, each pair being deposited at different filtering voltages. Subsequently, each pair of samples have one sample stored in an ambient atmosphere while the other one is stored in a special hermetic box with continuous flow of N_2 which pushes out ordinary air. For day 1 (day of deposition), all samples are red-shifted compared to the theoretical peak of the plasmon band in air at 355 nm as seen in Fig. 2.11. Considering the measurements on day 1 presented in Tab. 4.3, a surprising tendency is that samples with smaller NPs tend to show a more red-shifted plasmon band. This contrasts usual observations that increasing particle size red-shifts and broadens the plasmon bands[51]. These tendencies were simulated by Barber et al[52] and Meier et al[53] and are due to the dynamic depolarization field which is generated by the polarized matter surrounding the center of a particle. This depolarization needs to be taken into account when finding the resonance condition in Eq. (2.74) and instead leads to a denominator of $\epsilon_r(\omega)(1-q^2)+(2+q^2)+2/3\epsilon_i q^3=0$ in order to reach resonance, where $q = ka$, k being the wavenumber and a being the particle radius. In order to reach resonance for greater values of a, a more negative value of ϵ_r is required which corresponds to longer wavelengths. Simulations presented in [51], however, show that the red-shift caused by larger particles is small for small differences in particle size.

Table 4.3. Peak position of the relative extinction over time for quartz samples with Ag NPs

Filtering voltage	200 V		600 V		1200 V	
Sample	Q1 (Ambient)	Q2 (Nitrogen)	Q5 (Ambient)	Q6 (Nitrogen)	Q3 (Ambient)	Q4 (Nitrogen)
Day of measurement						
1	397 nm	397 nm	384 nm	384 nm	367 nm	371 nm
2	410 nm	400 nm	388 nm	387 nm		
3	413 nm	403 nm	389 nm	388 nm	373 nm	376 nm
4	413 nm	409 nm	392 nm	392 nm	375 nm	376 nm
5	414 nm	411 nm	393 nm	392 nm	376 nm	376 nm
6	416 nm	412 nm	392 nm	391 nm	377 nm	376 nm
7			392 nm	392 nm	377 nm	377 nm
8	417 nm	412 nm			377 nm	378 nm
9	420 nm	410 nm				
10/11	417 nm	413 nm	393 nm	393 nm	378 nm	378 nm
13	421 nm	413 nm				
17/18	423 nm	415 nm	396 nm	396 nm	381 nm	381 nm
23/24	424 nm	420 nm	396 nm	396 nm	382 nm	382 nm
30/31	421 nm	421 nm	396 nm	396 nm	382 nm	382 nm
37/38	421 nm	417 nm	397 nm	399 nm	382 nm	382 nm
44/45	415 nm	415 nm	399 nm	399 nm	383 nm	382 nm
51/52	415 nm	413 nm	400 nm	400 nm	383 nm	382 nm
52/59	415 nm	426 nm	400 nm	400 nm	384 nm	382 nm
65/66	417 nm	417 nm	403 nm	400 nm	385 nm	384 nm
72/73	415 nm	413 nm	400 nm	403 nm	384 nm	384 nm
79/80	415 nm	426 nm	403 nm	400 nm	385 nm	385 nm

A possible explanation to the red-shifting of the plasmon band for smaller NPs is that the smaller NPs are more affected by the underlying quartz substrate when considering the effective medium theory described in Subsec. 2.3.3. Simulations are carried out in order to estimate the effect on the plasmon bands caused by the effective medium.

The simulations for silver are carried out for three different NP radii (a) of 5, 8, and 10 nm, respectively. The thickness ($r - a$) of the dielectric shell surrounding the particle is kept at a constant of 10 nm (see Fig. 2.12). For different particle radii and constant shell thickness, the weighting factor β changes. The weighting factor ranges from 0 to 1 and describes how large a fraction of the total surrounding effective medium is air. A β value of 1 means that the NP is complete immersed in air, while a value of 0 means that the NP is completely immersed in the substrate. Fig. 4.7 shows how the plasmon band of differently sized NPs are blue-shifted with greater NP size, assuming that the effective medium has the same shell thickness for all sizes of particles. As the underlying quartz substrate has a higher refractive index than that of air, the effective refractive index of a medium surrounding the NP will become greater for NPs of smaller size.

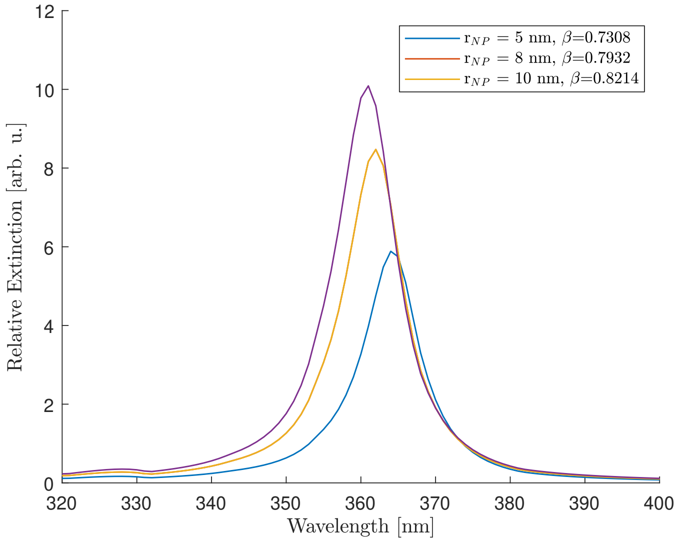

Figure 4.7. Evolution of the plasmon peak depending on the nanoparticle radius assuming a constant shell thickness $(r - a)$ of 10 nm.

As Fig. 4.7 shows, the difference caused by the effective medium variation is very small and as such cannot account for the up to 30 nm difference in plasmon band positions alone. The above simulation is made for completely spherical particles, but as argued earlier, there is a possibility that the particles have become oblate in shape. This possibly causes the underlying substrate to have an even greater effect on the effective medium surrounding the particles. Oblation of the particles also causes red-shifting of the plasmon peak as shown by Novikov et al[29] and Krenn et al[54]. Simulations show that in order for spherical particles to have a plasmon band position equivalent to the one observed for samples Q1 and Q2, the particles have to be completely immersed into the quartz substrate as shown in Fig. A.1 in App. A.1. Fig. 4.7 shows an increase in LSPR peak intensity which can be readily understood by considering Eq. 2.74. As shown, Q_{ext} is proportional to a^3. Increasing the particle size therefore leads to an increase in intensity of the LSPR peak.

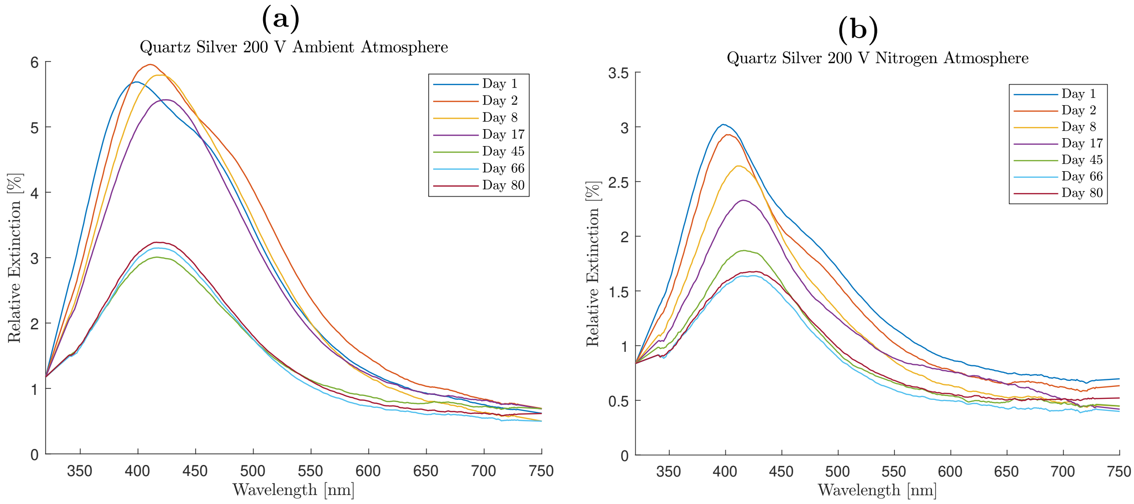

Figure 4.8. Relative extinction spectra for (a) Q1 and (b) Q2, respectively, with peaks as indicated in Tab. 4.3

The optical spectra of samples Q1 and Q2 are presented in Fig. 4.8 and show a gradual red-shifting of the peak band position with time. The gradual red-shift may be explained by a gradual change in the dielectric medium surrounding the NP. If species in the surrounding atmosphere interacts with the surface atoms of the Ag NPs and create oxides compounds, it is possible that the surface of the NPs gradually form a shell of silver oxide or silver compounds with dielectric constant large than unity around it. An increase in dielectric function red-shifts the plasmon band as per the resonance condition $\epsilon_r = -2\epsilon_m$ in Eq. 2.74. Novikov et al[29] performed similar measurements with NPs filtered at 300 V and 1600 V, respectively. Their results similarly showed that the plasmon band of smaller NPs was more red-shifted and the plasmon band for NPs filtered at 300 V was observed at around 385-390 nm as deposited which is in good agreement with the current work. On day 2, a red-shift is observed for both samples, albeit much more significantly for sample Q1 which was kept in ambient conditions. Q1 shows a significant increase in band intensity whereas no such thing is observed for Q2. The changes in plasmon band position and intensity may be related to chemical reactions of silver with atmospheric species and formation of a thin shell with dielectric function greater than unity which would explain why Q2 which was kept in a nitrogen atmosphere does not show as significant changes as Q1 after the first day. Another possible explanation is the deformation of the spherical NPs into an oblate shape[52]. When the optical measurements were performed, the sample were brought out of their respective environments, meaning that in particular sample Q2 may have been allowed to interact with atmospheric species which might explain the similarities in change of extinction intensity as seen in Fig. A.3. Over the course of 80 days, the extinction intensity for both samples has decreased significantly, approximately by 50 % and 60 % for Q1 and Q2, respectively. The main reason for the decrease in the plasmon band intensity is most likely caused by chemical interaction of NPs with environmental species such as sulphur or oxygen which possibly degrades the metallic core of the NPs into metallic compounds. In comparison Novikov et al[29] monitored the evolution of the LSPR bands of the smaller particles over the span of 30 days where they observed that the band intensity decreased by less than 20 %. Comparing the plasmon band intensity for the extinction of day 32 of samples Q1 and Q2, the equivalent decrease in intensity is about 25 % for both samples. This suggests consistency in the decrease in plasmon band intensity over time for particles produced in a MaSCA and filtered at the 200-300 V range. Tab. 4.3 shows that both samples Q1 and Q2 start to stabilise with regards to the plasmon peak position at around 415 nm on day 45. Fluctuations may in part be due the fact that measurements of the spectra were not necessarily taken on the same area of the sample every time as there are a few millimeters leeway in the sample holder. The relative extinctions shown in Fig. 4.8 are all relatively small and the coverage, as can be seen in Fig. 4.1, is below a monolayer, meaning that a weaker signal may lead to larger errors when processing the data, particularly during smoothing.

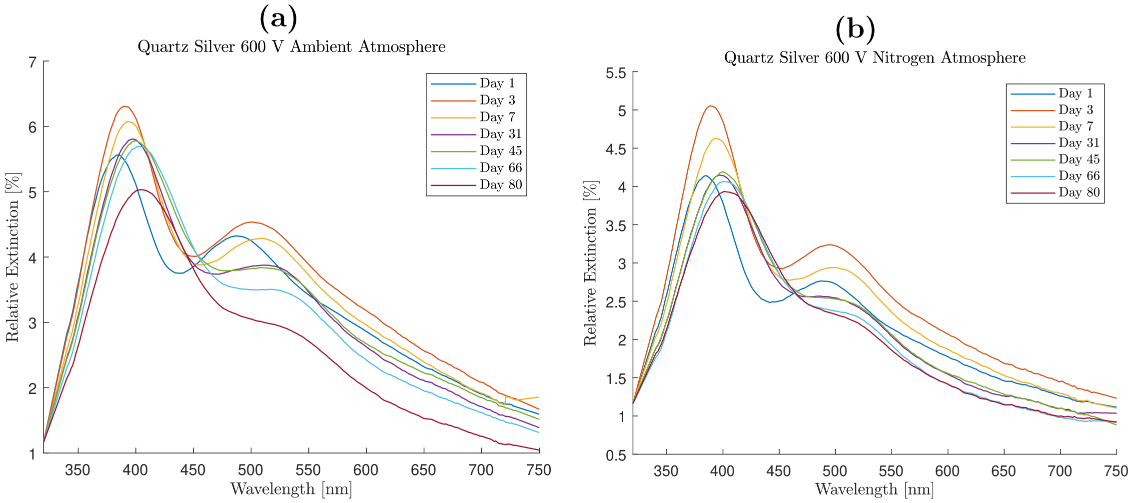

Figure 4.9. Relative extinction spectra for (a) Q5 and (b) Q6, respectively, with peaks as indicated in Tab. 4.3

As can be seen in Fig. 4.9, samples Q5 and Q6 show two plasmon bands. The one at shorter wavelength is associated with individual NPs, while the second one can be related to random formation of dimer or trimer structures as found in [29]. From Fig. 4.8 a similar second band as a shoulder of the first one can be resolved. The behaviour of the first band will be further discussed. Generally, Q5 and Q6 show the commonly observed red-shift over time with a particularly high red-shift on the second day as can be seen in Fig. 4.9. In contrast to sample Q2, Q6 does experience the same size of red-shift and increase in extinction intensity as Q5. This suggest that this initial phenomenon is not caused by ambient species reacting with the NPs which is further supported by considering sample Q4 which also experiences the same effect. As such, the initial postulate that the initial red-shift and increase in plasmon band intensity may be caused by the formation of silver oxide seems unlikely. Thus, the most probable cause for the red-shift and increase in intensity is the deformation of the NPs from spherical to oblate shape due to the difference in surface tension between quartz and silver as discussed earlier. Both samples show a gradual red-shifting, both red-shifting at the same rate and then stabilising around day 45. As argued above the initial red-shift of the plasmon band and its initial increase in intensity is most likely not due to the formation of silver oxides. Therefore, this formation seems to be the most likely cause of the gradual red-shift of the plasmon band peak over time. Both Q5 and Q6 show only small changes in the relative extinction as seen in Fig. 4.9. Over the course of 80 days, the extinction intensity of samples Q5 and Q6 are decreased by 20 % and 9 %, respectively. Worth noting is that the decrease in extinction intensity of the plasmon band is significantly smaller for samples Q5 and Q6 compared to Q1 and Q2. As the NPs on these samples are of greater radii, the fraction of surface atoms compared to the total amount of atoms is also smaller, meaning that the metallic core would degrade slower due to possible interaction with atmospheric species.

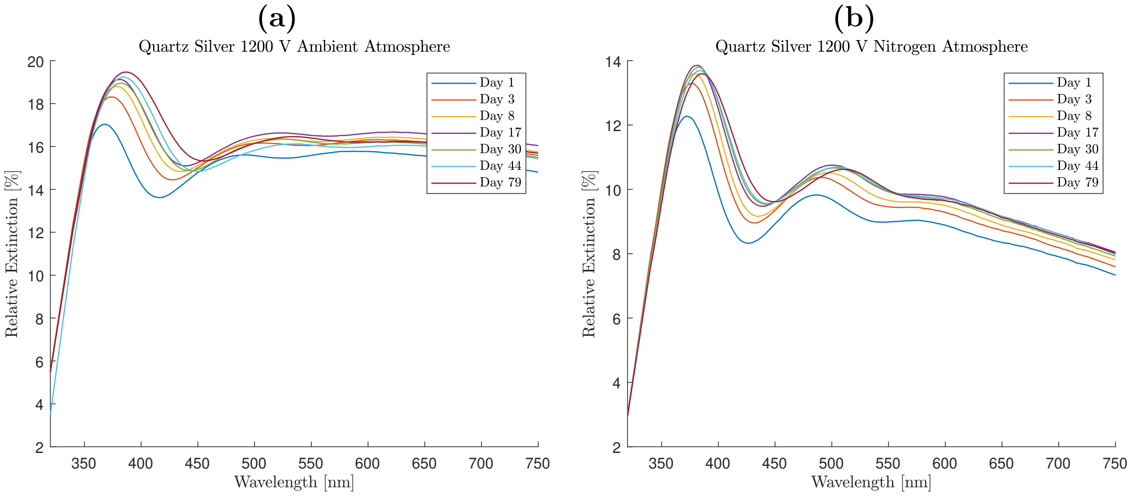

Figure 4.10. Relative extinction spectra for (a) Q3 and (b) Q4, respectively, with peaks as indicated in Tab. 4.3

Both samples Q3 and Q4 experience the same type of initial red-shift and increase in extinction of the band associated with individual particles after the first day as experienced by samples Q5 and Q6, further suggesting that the oblation of the NPs is the reason for the initial red-shift and increase in intensity of the plasmon band. The occurrence of further weakbands are also observed for Q3 and Q4 at approximately 510 nm and potentially at around 600 nm. This is probably due to the much higher coverage as seen in Fig. 4.3, meaning that the density of particles is greater, more easily allowing for aggregation of individual particles into dimers/trimers as supported by the high relative extinction. The high relative extinction is also partly due to the larger cluster size for Q3 and Q4 which leads to enhanced extinction as per Eq. 2.74. Over the subsequent weeks of monitoring, there are no losses in the extinction intensity of either Q3 or Q4 as seen in Fig. 4.10. The plasmon band intensities instead increase by 24 % and 9 % for Q3 and Q4, respectively. As mentioned earlier, NPs with greater radii have a small fraction of surface atoms, meaning that the metallic core would degrade slower than for NPs with smaller radii. For Q3 and Q4 which see an increase in plasmon band intensity, it is possible that the core has seen no degradation through interaction with atmospheric species. The increase in plasmon band intensity is likely caused by the reactions between the atmospheric species and the surface atoms of the NPs, forming some kind of silver oxide or silver compound shell with dielectric constant greater than unity around the NPs. This would cause an increase in the effective dielectric constant of the medium surrounding the NPs as described in Sec. 2.3.3 which in turns increases the plasmon band intensity as per Eq. 2.74. On day 45, the plasmon band peak once again stabilises as for the other samples.

All samples have stabilised around day 44/45. The total red-shift of the plasmon band from day 1 until day 44/45 of the samples with NPs filtered at 200 V, 600 V, and 1200 V correspond to 18 nm, 15 nm and 11 nm, respectively. There are two sizes of red-shift for Q3 and Q4, but from day 4, further red-shift of the plasmon band occurs at the same rate and as such only the day 1 value for Q4 is considered. That the plasmon band of smaller NPs red-shifts a greater amount before stabilising with respect to wavelength suggests that the shell that possible forms around the NPs have a greater effect on the plasmon band of the smaller NPs. Curry et al[34] suggests that when determining the sensing range $(r-a)$ of the shell surrounding the NP (see Fig. 2.12), the thickness is set equal to the radius of the particle a. For smaller radii, the effect of the silver oxide/compound shell would thus be larger than for the particles of greater radii, given the oxide/compound shell is limited in size by the surface atoms. This effect may explain the difference in red-shift of the plasmon band for differently sized NPs from day 1 until stabilisation on day 45 where the shell may have saturated.

The next couple of samples had UV-ozone treatment performed on them in order to see if a protective oxide shell could form around the NPs which should serve to prevent degradation of plasmonic properties.

Table 4.4. Peak position of the relative extinction over time for samples Q7 and Q8 with Ag NPs deposited on a quartz substrate at 1200 V and ozonated for 40 minutes.

Sample	Q7 (Nitrogen)	Q8 (Ambient)
Day of measurements		
Pre-ozonation	370 nm	370 nm
1	382 nm	382 nm
2	376 nm	360 nm
3	376 nm	∼425 nm
4	∼380 nm	∼425 nm
5	∼450 nm	431 nm
6	∼450 nm	442 nm
9	∼430 nm	455 nm
17	451 nm	457 nm
23	455 nm	451 nm
30	456 nm	447 nm
37	457 nm	443 nm
44	459 nm	445 nm
51	456 nm	439 nm
58	457 nm	438 nm
65	457 nm	439 nm
72	457 nm	438 nm
79	456 nm	438 nm

An interesting detail to note is that the initial position pre-ozonation of the plasmon peak of Q7 and Q8 are equivalent to the position of the plasmon peak for Q3 and Q4 which had NPs deposited at the same voltage. As can be seen in Fig. 4.11, both samples show secondary plasmon bands close to 500 nm before ozonation equivalently to those observed in Fig 4.10. Obtaining meaningful AFM images of the ozonated samples was difficult (see Fig. 4.4) but the similarities between the spectra support that the NPs deposited on Q7 and Q8 were of similar size and density as for Q3 and Q4. Immediately after ozonation for 40 minutes, the plasmonic properties of the NPs seemed to have been quelled as seen in Fig. 4.11, a trend for the following days. Finding precise positions for the peaks during several days after the ozonation was difficult as the extinction bands are of low intensity and very broad. Instead, an estimation was made from Fig. A.6 in App. A.2 where the decrease in extinction comes to a temporary halt. However, unexpectedly, on day 9, both samples start to show an increase of the plasmon band intensity. The subsequent measurements then show a gradual increase in extinction, in the case of Q8 even exceeding the relative extinction from pre-ozonation. The nature of this phenomenon is not understood and requires further study.

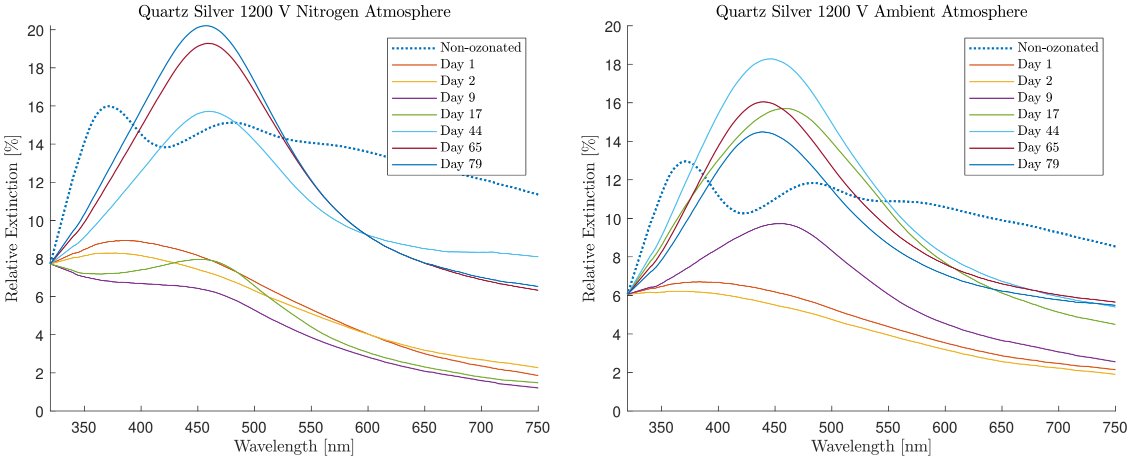
(a) **(b)**

Figure 4.11. Relative extinction spectra for (a) Q7 and (b) Q8, respectively, with peaks as indicated in Tab. 4.4

Quartz substrates Q9 and Q10 with Ag NPs deposited at 200 V were also ozonated for 40 minutes in order to see if there is a difference for smaller particles compared to larger ones described above. Optical measurements taken immediately after the ozonation of these samples, however, revealed complete quelling of the extinction intensity and as such was not monitored systematically. When samples Q7 and Q8 started showing signs of increasing the extinction intensity, optical measurements were performed on these samples in order to investigate if this was a general trend for ozonated Ag NPs. These samples, however, did not show the same increase in extinction intensity as samples Q7 and Q8 as can be seen in Fig. 4.12. One of the obvious conclusions that can be made is that size matters. It seems that metallicity of small particles is completely destroyed by ozonation and they are not able to recover LSPR.

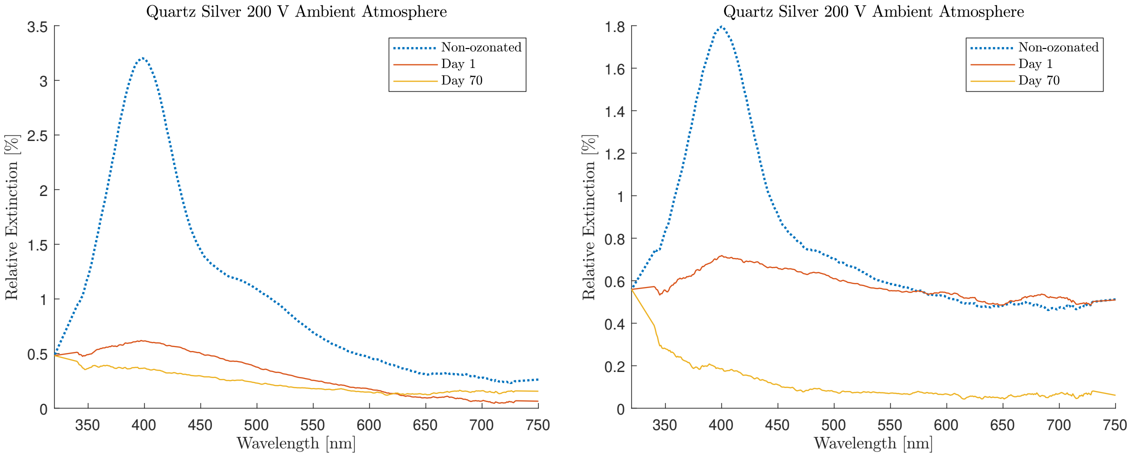
(a) **(b)**

Figure 4.12. Relative extinction spectra for (a) Q9 and (b) Q10, respectively.

To summarise, samples Q1 through Q6 with the exception of Q2 show an initial red-shift and increase in intensity of the plasmon band after the first day of optical measurements. Samples which were kept in the nitrogen atmosphere were stored there immediately after performing the optical measurements. As such it seems most likely that this phenomenon is caused by the deformation of the spherical NPs into oblately shaped NPs. The gradual red-shift of the plasmon band is then caused by formation of silver oxide/compound shells with larger than unity dielectric constant causing an increasing in the dielectric constant of the effective surrounding medium. The stability of the plasmon band of the NPs seems to increase with NP size. Over 80 days, the plasmon band intensity of the smallest NPs decrease by at least 50 %, while the plasmon band intensity of the medium sized NPs decrease between 9-20 % while the plasmon band intensity of the largest NPs show an increase of up to 24 %. No particular difference is observed for the atmosphere in which the samples are stored, although it has to be noted that measurements of the optical spectra were carried out in an ambient atmosphere. During the measurements, the samples kept in the nitrogen atmosphere were also exposed to ambient atmospheric conditions. Thus, these samples also had high chances to be affected by atmospheric species after many measurements.

Evolution of the optical spectra of all above-discussed samples for the first week after deposition can be found in App. A.2.

4.3 Evolution of Plasmonic Properties of Silver Nanoparticles on PMMA Substrates

This section discusses the evolution of the optical spectra of Ag NPs on PMMA samples in the same manner as in the previous section for quartz. The position of the plasmon band peak for different voltages at which the Ag NPs have been deposited on the samples as well as the atmosphere they are kept can be found in Tab. 4.5. The PMMA was not annealed after spin-coating and as such can be considered as a viscous and unhardened PMMA.

Table 4.5. Peak position of the relative extinction over time for PMMA samples with Ag NPs deposited at different voltages.

Filtering voltage	200 V		600 V		1200 V	
Sample	P3 (Ambient)	P4 (Nitrogen)	P7 (Ambient)	P8 (Nitrogen)	P5 (Ambient)	P6 (Nitrogen)
Day of measurement						
1	404 nm	400 nm	412 nm	386 nm	379 nm	382 nm
2	411 nm	404 nm	413 nm	387 nm		
3	413 nm	405 nm	413 nm	387 nm	388 nm	386 nm
4	413 nm	407 nm	416 nm	389 nm	390 nm	388 nm
5			415 nm	389 nm	390 nm	390 nm
6	416 nm	408 nm	413 nm	390 nm	390 nm	391 nm
7	416 nm	408 nm			391 nm	391 nm
8/9	417 nm	408 nm	416 nm	390 nm	392 nm	392 nm
11	417 nm	411 nm			392 nm	392 nm
15/17	418 nm	411 nm	417 nm	391 nm	396 nm	396 nm
23/25	418 nm	412 nm	411 nm	391 nm	396 nm	396 nm
30/32	420 nm	416 nm	418 nm	391 nm	397 nm	396 nm
37/39	421 nm	416 nm	416 nm	392 nm	399 nm	396 nm
44/46	421 nm	416 nm	413 nm	396 nm	400 nm	398 nm
51/53	422 nm	417 nm	423 nm	393 nm	400 nm	398 nm
58/60	425 nm	420 nm	418 nm	396 nm	404 nm	399 nm
65/67	425 nm	417 nm	424 nm	396 nm	404 nm	400 nm
72/74	425 nm	425 nm	421 nm	396 nm	404 nm	400 nm
79/81	425 nm	425 nm	424 nm	396 nm	405 nm	401 nm

Similarly to the quartz samples, the smaller particles have plasmon band maxima at longer wavelengths than those of larger NPs. The same considerations can be made using the effective medium theory as for the quartz samples. One only needs to take into account that the refractive index of PMMA is slightly greater than that of quartz ($n_{\mathrm{PMMA}} = 1.48$, $n_{\mathrm{quartz}} = 1.45$) and as such the presence of PMMA would lead to a slightly larger red-shift of the plasmon band for the same particle size compared to quartz. This tendency can be clearly seen by comparing the values presented in tables 4.3 and 4.5. One should also consider a higher probability for a NP to become embedded into the PMMA compared to quartz, meaning that the weighting factor of the PMMA can also be larger, particularly for the smaller particles filtered at 200 V. Looking carefully into Tab. 4.5, one can see an outlier which is sample P7 having very high red-shift compared to all other samples. The reason could be more significant particle embedding into PMMA film compared to other samples.

As can be seen in Fig. 4.13, both sample P3 and P4 show gradual red-shifting of the plasmon peak while the extinction rises on day 2 and then gradually decreases as time passes. As was the case for the equivalent quartz samples Q1 and Q2, the gradual red-shift of the plasmon band of P3 and P4 may be due to the oblation of the NPs. However, the oblation of the NPs is due to the difference in surface tension between Ag and quartz as mentioned in Sec. 4.1. The surface tension of PMMA ($\gamma_{\mathrm{PMMA}} = 41$ mJ/m^2) is of the same order of magnitude as that of quartz. The PMMA used in this work, however, is a viscous PMMA and is much softer than quartz and as such will more likely allow for embedding of the NPs instead of oblation. It is more likely, then, that the immediate red-shift and increase in intensity of the plasmon band are caused by partial embedding into the PMMA instead of oblation. Hanif et al[48] performed similar depositions of Ag NPs filtered at 300 V onto viscous PMMA substrates. They found that for Ag NPs deposited under these conditions, the aspect ratio ($< d > / < h >$) = 1.06, where $< d >$ is the lateral diameter of a NP and $< h >$ is the average height of a NP, supporting that the change between day 1 and day 2 is caused by partial embedding of the NPs. Over the course of 79 days the plasmon band intensities gradually decrease by a total of 14 % and 9 % for P3 and P4, respectively. This decrease is much smaller than for Q1 and Q2 at 50 % and 60 %, respectively, and may be due to a smaller amount of surface atoms being readily available for reactions with atmospheric species because of the partial embedding of the NPs. Another possibility is that the NPs deposited on PMMA become further embedded thereby increasing the effective dielectric constant of the surrounding medium due to the larger contribution from PMMA. Thus, a potential decrease in the plasmon band intensity may be "hidden". If this is the case, NPs of smaller size may see a smaller decrease in plasmon band intensity. As can be seen in Tab. 4.5, the plasmon bands for P3 and P4 stabilise with respects to wavelength around 425 nm. The total red-shift of the plasmon band peaks for samples P3 and P4 are 21 nm and 25 nm, respectively. The equivalent quartz samples, Q1 and Q2, have a red-shift of between 18 and 20 nm. The larger red-shift of the plasmon bands for P3 and P4 compared to Q1 and Q2 is likely due to the combined effects of embedding into PMMA and interactions with atmospheric species. Both embedding into the PMMA and interactions with species would cause the effective dielectric constant of the surrounding medium to increase, thus leading to a red-shift of the plasmon band.

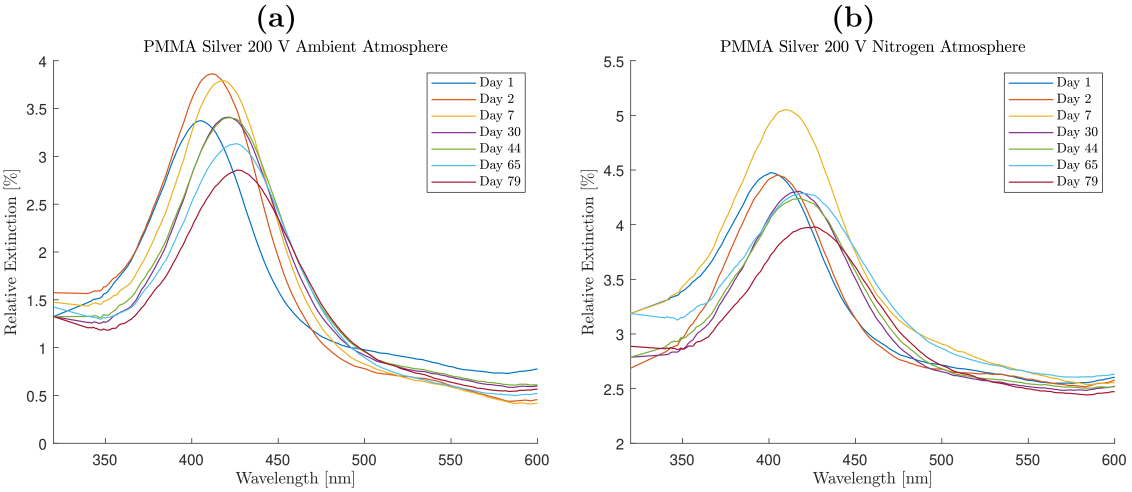

Figure 4.13. Relative extinction spectra for (a) P3 and (b) P4, respectively, with peaks as indicated in Tab. 4.5

As can be seen in Fig. 4.14, P7 and P8 do not show the same red-shift of the plasmon band or increase in intensity on day 2 of measurements as observed for Q5 and Q6. As argued earlier, the initial red-shift and increase in intensity of the plasmon band between days 1 and 2 of measurements for the quartz samples is likely caused by the oblation of the NPs. For the NPs deposited on PMMA, this does not occur due to the softness of the

PMMA. As such, the difference between the two sets of samples for the first two days is reasonable. P7 and P8 have a second plasmon band at around 550-600 nm as was the case for Q5 and Q6, albeit for Q5 and Q6 the second plasmon band was present at 500-550 nm. With respect to plasmon band peak, P7 is an outlier as mentioned earlier. This might be due to the fact that after spin-coating of the PMMA, the substrates were not annealed, meaning that the PMMA is soft and viscous, more easily allowing for the NPs to be directly embedded on deposition. All the PMMA substrates were prepared on the same day while the deposition of NPs was performed on different days. As such, the PMMA substrates most likely have varying degree of hardness, although only P7 is an outlier. All data obtained for PMMA substrates have been processed with the same baseline for PMMA as described in Subsec. 3.2.2. This might be the cause of the much larger red-shift of the plasmon band for P7. P7 and P8 both show gradual decrease in the intensity of the plasmon bands together with a red-shift. Over the course of 79 days, the intensity of the plasmon bands decrease by 10 % and 12 % for P7 and P8, respectively. Comparatively, Q5 and Q6 saw decreases of 20 % and 9 %, respectively. If the assumption made earlier that the contribution to the effective dielectric constant of the surrounding medium from the embedding into PMMA "hides" the decrease in plasmon intensity, these results are reasonable. As the plasmon band is more red-shifted compared to the other samples with PMMA, it is reasonable to assume that the NPs have been further embedded into the PMMA. As such the increase in intensity due to PMMA makes up for the decrease in intensity due to interactions with atmospheric species. However, the results for Q5 and Q6 and P7 and P8 show good agreement with each other. Averagely, the decrease in intensity for samples P3+P4 and P7+P8 are the same (=22 %). If the equivalent quartz pairs Q1+Q2 and Q5+Q6 are considered, there is a larger average difference (55 % vs 14 %, respectively). The reason for this large average difference may be due to the increase in plasmon intensity caused by embedding mentioned earlier. The smaller size NPs deposited on P3 and P4 more easily embeds into the PMMA compared to the medium sized NPs deposited on P7 and P8. An increase in plasmon intensity from embedding into PMMA which causes increase in ϵ_m will thus be larger for particles of smaller size as they more easily embeds into the PMMA. This effect will to a larger degree make up for the decrease in plasmon intensity due to reactions with atmospheric species for smaller sizes of NPs. This may be the case for the NPs deposited on PMMA but this effect cannot occur on the quartz samples, thus leading to a larger average difference in the decrease of the plasmon band intensities. P7 seemingly stabilises with regards to the plasmon peak at 423 nm while P8 stabilises at 396 nm, leading to total red-shifts of the plasmon bands of 11 nm and 10 nm, respectively. Unusually, these are smaller red-shifts than the ones for Q5 and Q6 which both show total red-shifts of 15 nm. As argued above, the combined effect of embedding into PMMA and interactions with atmospheric species should lead to a larger total red-shift of the PMMA samples when compared to their quartz equivalents. This discrepancy suggests that P7 and P8 may have been affected less by atmospheric species compared to the Q5 and Q6.

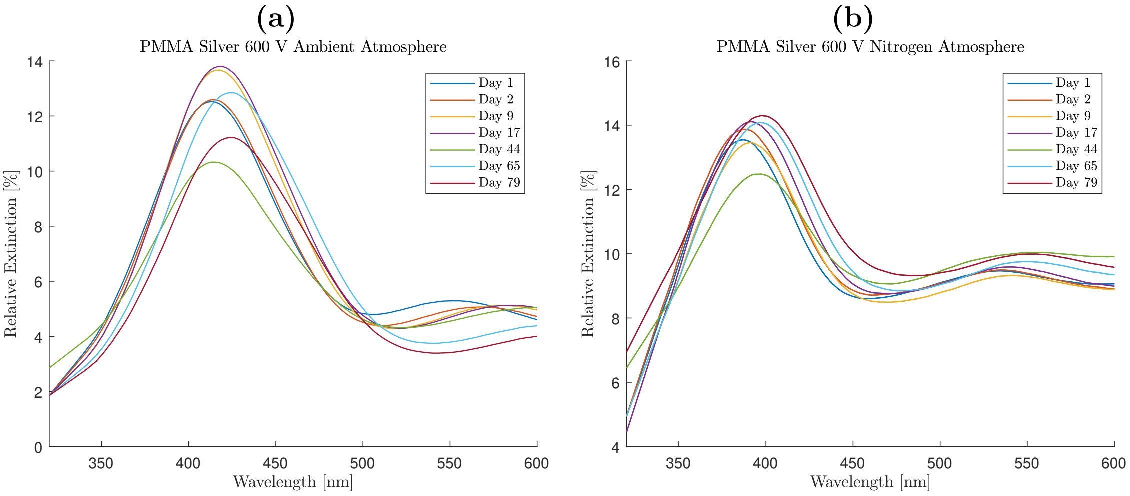

Figure 4.14. Relative extinction spectra for (a) P7 and (b) P8, respectively, with peaks as indicated in Tab. 4.5

Contrary to P7 and P8, P5 and P6 do show both a red-shift of the plasmon band as well as an increase in its intensity on day 3 of measurements as can be seen in Fig. 4.15. The most probable cause is that the viscous PMMA of these particular samples allows for embedding of large NPs. After the red-shift of the plasmon band and its increase in intensity on day 3, the plasmon bands continue the red-shift and increasing of intensity over time. As for samples Q3 and Q4, the most probable cause for the continuous increase in intensity and red-shift of the plasmon band for P5 and P6 is the formation of a silver oxide/compound shell with dielectric constant greater than unity around the NPs. This shell then protects the core of the NP from chemically interacting with species in the surrounding atmosphere while at the same time increasing the effective dielectric constant of the medium surrounding the NPs. Further embedding into the PMMA as time passes also leads to an increase in the plasmon band intensity and a red-shift thereof. It is worth mentioning that the second band at larger wavelength is much less pronounced compared to the case of quartz. It might be suggested that particles deposited on PMMA have much lower diffusion mobility and, thus, much lower probability of forming dimer structures. They also show a very high degree of stability, showing no signs of degradation over a time period of 53 days, much like their quartz-substrate counterparts. P5 and P6 seem to have stabilised with regards to plasmon band peak position at 404 nm and 399 nm, respectively. The total red-shift of the plasmon band are then 20 nm and 17 nm, respectively compared to the 16 nm and 11 nm of Q3 and Q4. The differences in total red-shift of the plasman band are most like caused by the effect of the PMMA on ϵ_m.

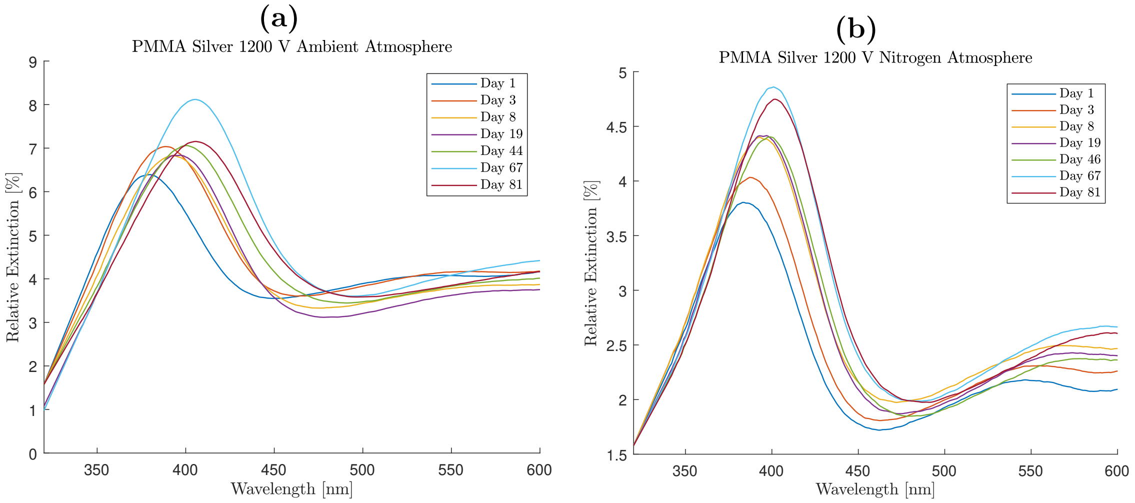

Figure 4.15. Relative extinction spectra for (a) P5 and (b) P6, respectively, with peaks as indicated in Tab. 4.5

To summarise, samples P3 through P8 generally show a higher degree of stability with regards to the intensity of the plasmon band than their quartz counterparts. The quartz substrate show the tendency that the degree of stability with regards to plasmon band intensity increase with size. The same tendency is partially observed for the PMMA substrates but it is hard to conclude whether it is a general rule for the PMMA substrates, as the PMMA also plays a role in the increase in plasmon band intensity. The red-shift on the plasmon band and increase of the intensity there of observed between day 1 and day 2/3 for the quartz substrates was not observed for the PMMA substrates. This is due to the fact that the PMMA is a softer material than quartz and the difference in surface tension therefore promotes embedding instead of oblation of the NPs. No significant differences were observed for the samples stored in nitrogen and ambient atmosphere. Similarly, the samples were exposed to atmospheric conditions during measurement of their optical spectra, allowing for atmospheric species to promote chemical reaction and convert metallic silver into compounds.

Evolution of the optical spectra of all above-discussed samples for the first week after deposition can be found in App. A.3.

4.4 Evolution of Plasmonic Properties of Copper Nanoparticles on Quartz Substrates

This section discusses the data obtained on the quartz samples with Cu NPs deposited at differing filtering voltages of 600 and 1200 V. The as-deposited samples are also compared to those treated by ozone. Ozonation was performed in order to study if a homogeneous protective shell of oxide can be formed around a Cu NP in order to preserve its LSPR from degrading.

Table 4.6. Peak position of the relative extinction over time for quartz samples with Cu NPs deposited at different voltages and ozonation times.

Filtering voltage	600 V		1200 V		1200 V	
Ozonation time	30 min		20 min		40 min	
Sample	C5 (Nitrogen)	C6 (Ambient)	C1 (Nitrogen)	C2 (Ambient)	C3 (Nitrogen)	C4 (Ambient)
Day of measurement						
Pre-ozonation	590 nm	585 nm	589 nm	582 nm	596 nm	597 nm
1	611 nm	611 nm	597 nm	598 nm	615 nm	621 nm
2	614 nm	612 nm	597 nm	600 nm	616 nm	617 nm
3	613 nm	613 nm	598 nm	599 nm	618 nm	621 nm
4	631 nm	631 nm	600 nm	600 nm	617 nm	619 nm
5	621 nm	608 nm	598 nm	600 nm	618 nm	622 nm
6	613 nm	613 nm	598 nm	600 nm	619 nm	622 nm
7/8	614 nm	612 nm	598 nm	600 nm	617 nm	621 nm
11/12	621 nm	613 nm	600 nm	601 nm	621 nm	624 nm
17/18	613 nm	612 nm	600 nm	602 nm	619 nm	617 nm
24/25	614 nm	613 nm	602 nm	602 nm	619 nm	614 nm
31/32	613 nm	608 nm	602 nm	602 nm	621 nm	615 nm
38/39	619 nm	632 nm	604 nm	605 nm	620 nm	629 nm
45/46	627 nm	612 nm	602 nm	603 nm	622 nm	628 nm
52/53	626 nm	612 nm	604 nm	606 nm	621 nm	622 nm
59/60	612 nm	612 nm	603 nm	606 nm	621 nm	621 nm
66/67	612 nm	614 nm	605 nm	605 nm	622 nm	617 nm
73/74	622 nm	612 nm	607 nm	606 nm	621 nm	617 nm
80/81	614 nm	631 nm	607 nm	607 nm	622 nm	619 nm

Plasmon extinction for Cu NPs is known to be lower compared to Ag ones. Thus, for similar particle sizes and surface coverage, much lower plasmon band intensity is expected for the case of Cu. Considering Fig. 4.1, it is observed that the difference between the average height of the particles used for Cu are roughly 6 nm, meaning that any shift in plasmon peak position after deposition should be minor. The difference that are present may be due to difference in coverages as can be seen in figures 4.5 and 4.6. The spectra presented in Fig. 4.17 shows a lot of noise compared to figures 4.18 and 4.19. Due to the lower extinction intensity for samples C5 and C6, the error in the optical measurements become larger and the data becomes more fluctuating, meaning that the position of the plasmon peak is less reliably found.

Simulations of Cu NPs with sizes corresponding to the average heights of the Cu NPs found in Tab. 4.1 are carried out. The thickness $(r - a)$ of the dielectric shell surrounding the particle is kept at a constant of 10 nm. For a constant thickness of the surrounding shell the weighting factor β will depend on the radius of the simulated particle. $\beta = 0$ corresponds to complete immersion in air, while $\beta = 1$ corresponds to complete immersion into the quartz substrate. Fig. 4.16 shows that simulations of the extinction depending on the particle radius a, and in extension of that β, has very little influence on the position of the plasmon peak. Given the small difference in NP radii ($a = 8.2$ nm and $a = 11.1$ nm, respectively), only a minor increase in extinction intensity is seen for the larger radius NP. It can be seen from Fig. 4.16 that the theoretical plasmon band peaks for Cu NPs of diameters of 16 nm and 22 nm are at circa 560 nm. Comparison of these simulations with tables 4.6 and 4.7 show that the plasmon peaks for the experimental data are all red-shifted by 18-37 nm. Fig. A.2 shows the relationship between the relative extinction and β value of a spherical Cu NP with a radius of 8 nm. Even complete immersion of the Cu NP into the quartz ($\beta = 0$) is blue-shifted compared to experimental data for as-deposited Cu NPs and corresponds to $\lambda = 560$ nm. This discrepancy may be explained with the simplicity of the quasi-static approximation used in Sec. 2.3 which neglects the effect of size and shape on the plasmon band position.

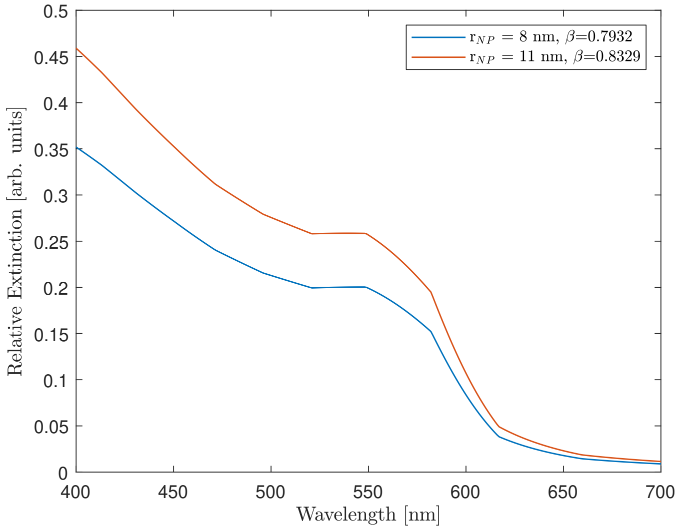

Figure 4.16. Evolution of the plasmon peak depending on the nanoparticle radius assuming a constant shell thickness $(r - a)$ of 10 nm. Dielectric data taken from [33].

The optical spectra for samples C5 and C6 in Fig. 4.17 exhibit very similar characteristics. Before ozonation, the LSPR peaks are located at 590 nm and 585 nm for C5 and C6, respectively. In comparison, the maximum efficiency for Cu in air is circa λ=560 nm as mentioned earlier. In comparison, Popok et al[23] deposited Cu NPs with a MaSCA filtered at 500 V on a quartz substrate which showed an LSPR peak located at 580 nm. The 100 V difference in filtering voltage may account for the 5-10 nm discrepancy in LSPR peak location in the current work. Immediately after ozonation for 30 minutes, the plasmon bands for C5 and C6 are red-shifted and broadened and the intensity of the plasmon band is reduced by 10 % for both samples. The decrease in plasmon band intensity is likely due to the high reactivity of copper with oxygen[44]. During the ozonation process, metallic copper is rapidly converted into copper oxide instead of forming a homogeneous protective layer around the NPs. This is opposed to the findings in [23] where the plasmon band intensity is increased after ozonation for 20 minutes. It is possible that the prolonged treatment time for the ozonation procedure has caused the degradation to take place instead of the shell formation of the protective layer. After 80 days, no change is observed for either sample with regards to the intensity of the plasmon bands or the peak location of these bands compared to day 1 (day of ozonation).

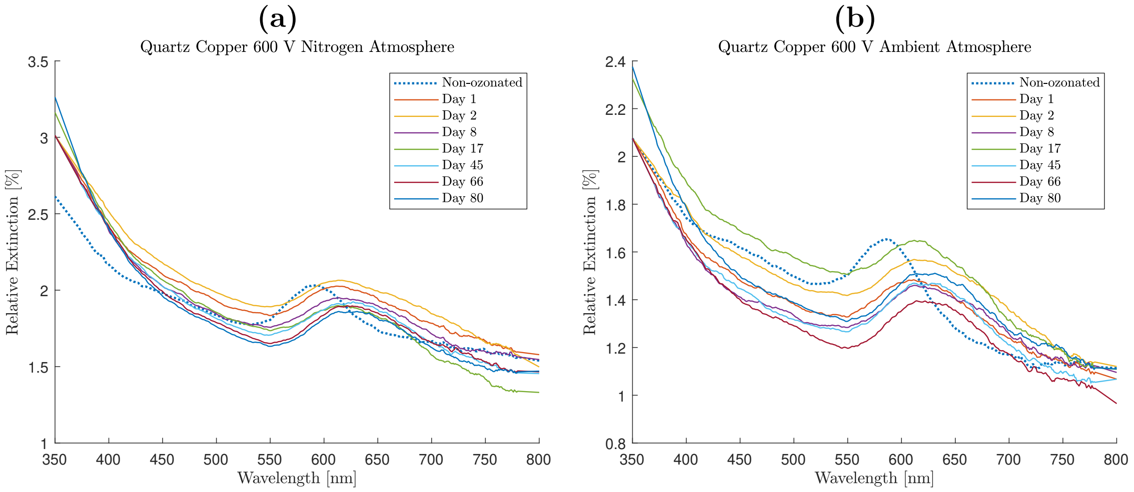

Figure 4.17. Relative extinction spectra for (a) C5 and (b) C6, respectively, with peaks as indicated in Tab. 4.6

The optical spectra for samples C1 and C2 exhibit the characteristics which were expected from the ozonation treatment. Before ozonation, the plasmon band peaks are found at 589 nm and 582 nm for C1 and C2, respectively. In comparison Ceynowa[55] performed similar measurements on ozonated Cu NPs deposited on quartz substrate with a MaSCA with filtering voltages at 1000 V, showing plasmon band peaks at 580 nm. The relative extinction of C1 and C2 are much higher than those presented in [55] which might account for the red-shift of plasmon bands of C1 and C2. After ozonation of C1 and C2, their plasmon bands are red-shifted and the intensity is increased, indicating that an oxide shell has formed around the Cu NP together in with it a change in the dielectric environment surround the NP. After 81 days of storage in nitrogen and ambient atmosphere for C1 and C2, respectively, the intensity is further increased and an additional red-shift of the plasmon band is observed. The increase over 81 days may be explained through the conversion of metallic copper on the surface into copper oxide (Cu_2O), leading to an increase in the surrounding dielectric medium. The dielectric constant of copper oxide in the 350-800 nm interval is approximately 9[56], which is significantly higher than the dielectric constant of air = 1. The data presented in [23] is also in accordance with the assumption that ozonation process forms a protective shell around the Cu NP with prevents it from degrading due to interactions with atmospheric species. After 81 days, the plasmon band intensity has increase by 154 % and 83 % for C1 and C2, respectively. Neither sample show signs of stabilising with respect to the position of the plasmon band peak.

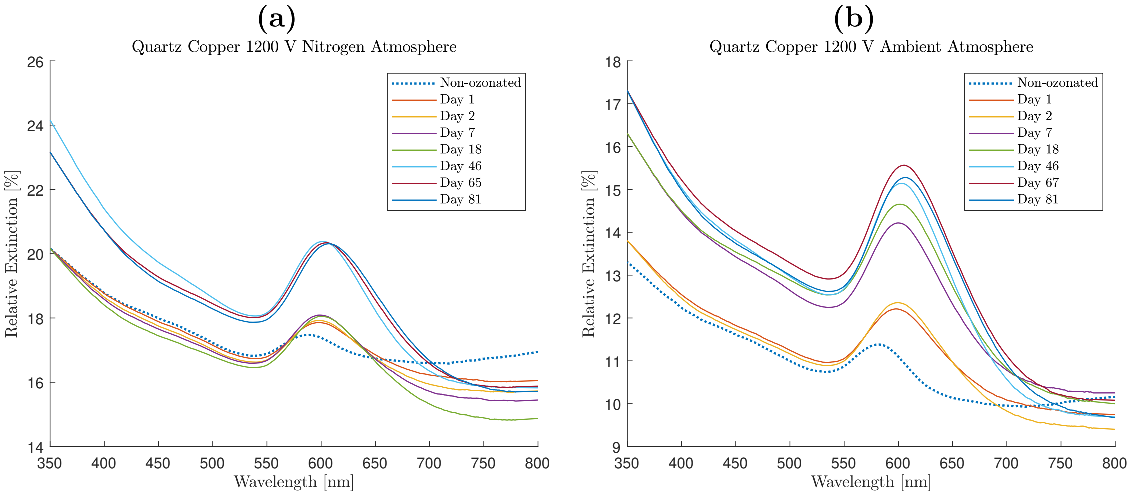

Figure 4.18. Relative extinction spectra for (a) C1 and (b) C2, respectively, with peaks as indicated in Tab. 4.6

Samples C3 and C4 show the same excellent tendencies as for samples C1 and C2 as can be seen in Fig. 4.18. This might be expected as the only difference in production of the samples was the amount of time they were ozonated, suggesting that the smaller amount of time of 20 minutes of ozonation is sufficient to form a protective oxide layer around the Cu NPs for the case of NPs filtered at 1200 V. As a comparison, the plasmon band intensity after 81 days is increased by 35 % and 14 % for C3 and C4, respectively.

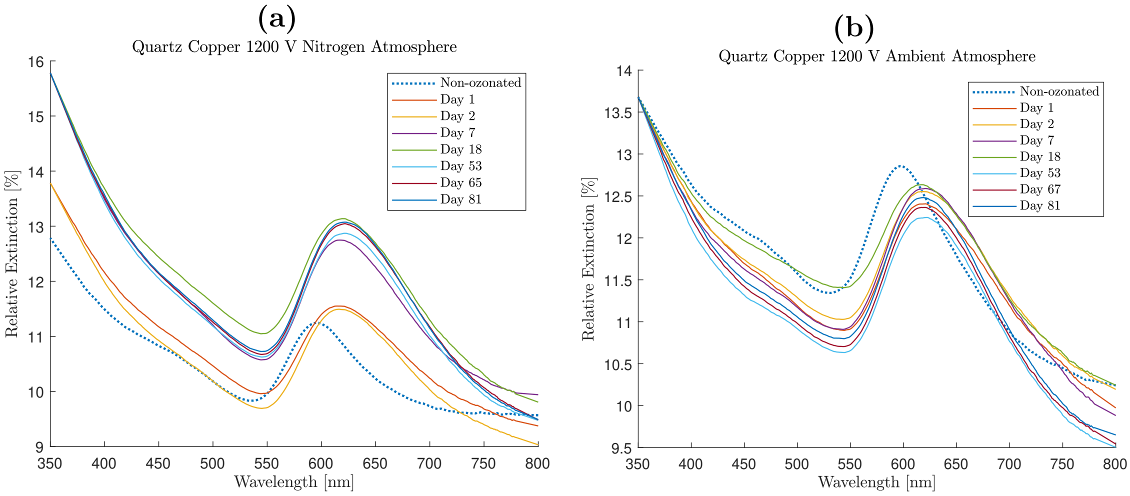

Figure 4.19. Relative extinction spectra for (a) C3 and (b) C4, respectively, with peaks as indicated in Tab. 4.6

Next, quartz substrates with Cu NPs deposited and non-ozonated are presented and discussed. These samples were produced in order to study the difference between ozonated and non-ozonated NPs.

Table 4.7. Peak position of the relative extinction over time for quartz samples with Cu NPs deposited at different voltages.

Filtering voltage	600 V		1200 V	
Sample	C7 (Nitrogen)	C8 (Ambient)	C9 (Nitrogen)	C10 (Ambient)
Day of measurement				
1	584 nm	578 nm	589 nm	578 nm
2	586 nm	585 nm	589 nm	584 nm
3	586 nm	589 nm	589 nm	585 nm
4	589 nm	589 nm	590 nm	586 nm
5	590 nm	596 nm	590 nm	586 nm
12	591 nm	608 nm	591 nm	591 nm
19	593 nm	621 nm	592 nm	593 nm
26	598 nm	621 nm	596 nm	596 nm
33	601 nm	628 nm	593 nm	597 nm
40	607 nm	634 nm	594 nm	597 nm
47	607 nm	634 nm	596 nm	600 nm
54	607 nm	642 nm	596 nm	600 nm
61	608 nm	640 nm	596 nm	601 nm
68	614 nm	642 nm	596 nm	603 nm

For samples C7 and C8, there is a large difference in the evolution of the LSPR bands as seen in Fig. 4.20. Both samples show an initial increase in extinction as well as a red-shift of the plasmon band. As is the case for Ag NPs, this change is most likely due to the oblation of the NPs due to the difference in surface tension between copper and quartz. For copper the surface tension $\gamma_{\text{Cu}} \approx 1650$ mJ/m^2 while for quartz γquartz < 100 mJ/m^2[50]. For the following weeks, however, C8 has a much larger decrease in the extinction intensity together with a broadening of the peak band whereas C7 shows no such tendencies. As C8 is kept in the ambient atmosphere, whereas C7 is kept in a nitrogen atmosphere. As copper is highly reactive, particularly with oxygen[41], the large abundance of oxygen in the air is most likely the cause for the decrease in plasmon band intensity of C8 which is kept in the ambient atmosphere, while C7 which is kept in a nitrogen atmosphere has no oxygen to react with. After 64 days, the decrease in plasmon band intensity is 0 % and 84 % for C7 and C8, respectively. As such, storing copper NPs in a nitrogen atmosphere seem to be an excellent method of preventing degradation of their plasmonic properties.

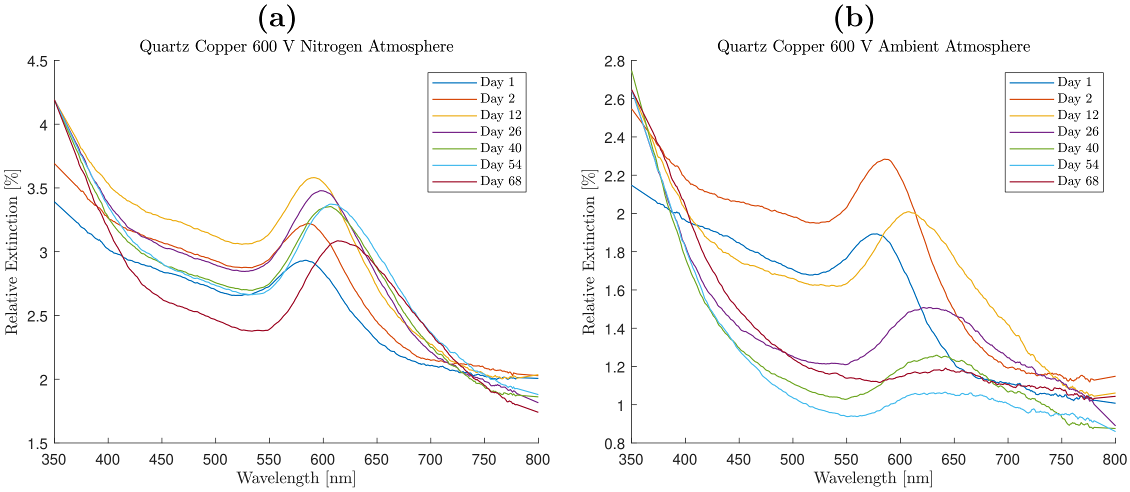

Figure 4.20. Relative extinction spectra for (a) C7 and (b) C8, respectively, with peaks as indicated in Tab. 4.7

In contrast to samples C7 and C8, samples C9 and C10 are both highly stable for the entire duration of 64 days. In fact, both samples show an increase in the plasmon band intensity as time passes. After 64 days, the plasmon band intensities increase by 31 % and 108 % for C9 and C10, respectively. This is surprising as the non-ozonated samples should show the same tendencies, respective of size difference. C9 and C10, however, are deposited at 1200 V for which the ozonated samples were highly stable. The smaller fraction of surface atoms might be the cause of the differences, disallowing smaller NPs to be ozonated as they may react too easily with the oxygen/ozone during the ozonation process allowing the oxygen to oxides the NPs internally while this is not the case for the larger NPs. This may also be the reason for the larger NPs being more stable even in an ambient environment. In [55], the stability of Cu NPs deposited on quartz and filtered at 1000 V was also investigated over a timeline of 10 weeks in an ambient environment. Results showed that the plasmon band intensity of the Cu NPs were strongly preserved over 5 weeks and still had not be completely quelled over a timeline of 10 weeks. The reason for the increase in plasmon band intensity in the current work is most likely due to the conversion of metallic copper on the surface into copper oxide (Cu_2O), leading to an increase in the surrounding dielectric medium

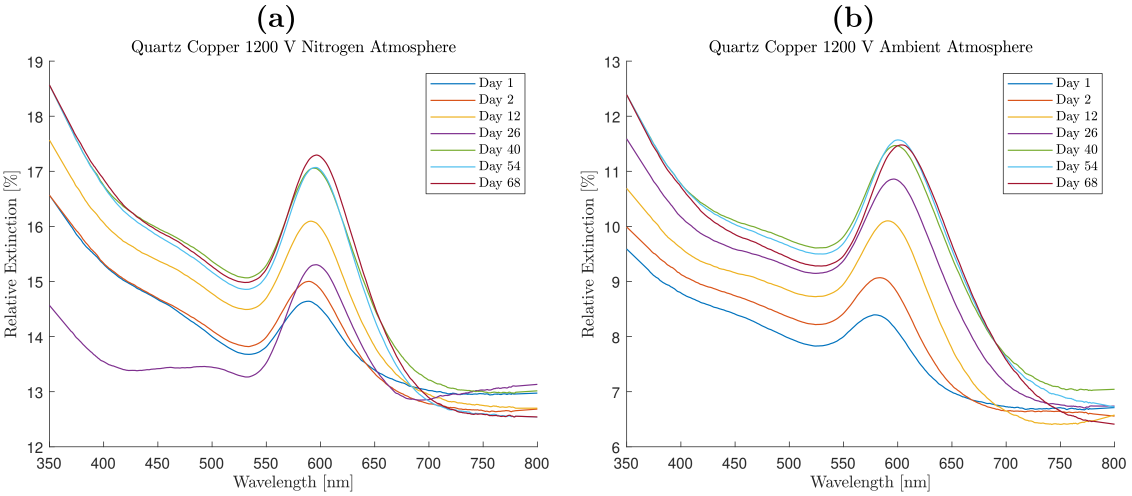

Figure 4.21. Relative extinction spectra for (a) C9 and (b) C10, respectively, with peaks as indicated in Tab. 4.7

In order to investigate the effects of the ozonation, initial XPS measurements were performed on 4 grids with Cu NPs deposited at 200 V, two of which were ozonated and two of which were not. Preliminary observations of the XPS measurements showed that the non-ozonated samples had formed CuO and Cu_2O oxide connections, while the ozonated samples had only formed Cu_2O oxide connections, suggesting that ozonation of samples indeed does prevent the Cu NPs from degrading further into oxides. This is also in agreement with the assumption that the dielectric environment of the surrounding medium would increase.

To summarise, all samples with Cu NPs deposited at 1200 V showed great stability with respect to the extinction intensity. Of the samples with Cu NPs deposited at 600 V, only samples C7 which was not ozonated and stored in nitrogen showed good stability in the extinction intensity. The reason that the smaller NPs do not become stable after ozonation is probably due to the ozonation rapidly converting metallic copper into oxides other than Cu_2O where as this does not occur for the larger Cu NPs. At the same time, C7 and C8 show differences depending on their atmospheric environment. C7 (nitrogen atmosphere) showed good stability with regards to the extinction intensity while C8 (ambient atmosphere) did not. Storing Cu NPs in a nitrogen atmosphere thus seems to be an effective method of preventing degradation of Cu NPs from oxygen interactions.

Evolution of the optical spectra of all above-discussed samples for the first week after deposition can be found in App. A.4.

Chapter 5

Conclusion

Ensembles of size-selected Ag and Cu NPs on quartz and PMMA substrate are fabricated using a magnetron based sputtering cluster apparatus (MaSCA). Ag NPs with sizes of approximately 8 nm, 13 nm, and 29 nm are deposited on quartz and quartz-PMMA substrates, while Cu NPs with sizes of approximately 16 nm and 22 nm are deposited on quartz substrates. Subsequently, optical measurements of the samples with NPs are performed in order to monitor the evolution of the LSPR bands of the NPs over time. Ozonation is investigated as a method of protecting the plasmonic properties of metallic NPs from degradation due to interactions with atmospheric species. All samples are made in pairs of which one is stored in an ambient atmosphere while one is stored in a nitrogen atmosphere. This is all done in order to investigate the stability over time of Ag and Cu NPs depending on the size of the NPs and the environment surrounding the NPs.

The peak of the plasmon band of Ag NPs on quartz substrates is observed to blue-shift with increasing particle size. As particles becomes smaller, the effect on the surrounding medium is more greatly affected by the underlying quartz substrate. Additionally, stability of the extinction intensity is seen to increase significantly for larger Ag NPs. Over the course of 80 days, the only samples with Ag NPs deposited that showed a decrease of the plasmon band intensity of over 25 % were the samples with Ag NPs of diameter 8 nm, showing a decrease in plasmon band intensity of 60 % and 50 % for Q1 and Q2, respectively. The two pairs of ozonated Ag NPs samples showed very different results. Immediately after ozonation, both pairs show complete quelling of the plasmon band intensities. After a few days, one pair of samples shows a gradual increase in the plasmon band intensity whereas the plasmon band intensity of the other pair of samples remains quenched. These trends continue over time. This phenomenon is not understood and requires further studies.

The results for the Ag NPs on PMMA substrates and quartz substrates are not in complete agreement. The Ag NPs deposited on quartz showed that the stability of the plasmon band intensity increases with increasing particle size. This general tendency is not observed for the Ag NPs deposited on PMMA substrates. All PMMA samples show great stability in terms of the plasmon band intensity over time. After 80 days, no PMMA samples show a decrease of the plasmon band intensity of over 14 %. The overall greater stability of the PMMA substrates is likely due to the increase in the dielectric constant of the surrounding medium. This increase in the dielectric constant is caused by the higher dielectric constant of PMMA compared to quartz.

For the Cu NPs on quartz substrates, the larger NPs all show great stability in their plasmonic properties. For the smaller particles only one of the samples show good stability in its plasmonic properties. This is the non-ozonated sample stored in a nitrogen atmosphere and it shows no decrease in its plasmon band intensity.

It is found that larger Ag and Cu NPs fabricated by the use of MaSCA tend to be more stable with regard to their plasmonic properties regardless of the atmospheric conditions they are stored in. Ozonation of Ag NPs does not seem to be an efficient method for protecting their plasmonic properties as quenching of their plasmon band intensities is observed. For larger sizes of Cu NPs the method of creating a protective oxide shell around the NPs have been found an efficient method of increasing the stability of the plasmonic properties.

The reported results showcase a high degree of stability of plasmonic properties over up to 80 days of MaSCA fabricated Ag and Cu NPs. The MaSCA fabricated Ag and Cu NPs are of highly pure and monocrystalline nature. The monocrystalline nature of the particles mean that only atoms present at the surface of the NP should be reactive as a result of reduced coordination numbers. Due to the high stability of the plasmonic properties the reported results are highly relevant to the fabrication of metamaterials, sensors, and waveguides utilizing the plasmonic properties of metallic NPs produced by a MaSCA.

Bibliography

[1] Roy L. Johnston. *Atomic and Molecular Clusters*. Taylor and Francis, 1st edition, 2002. ISBN 0-748-40930-0.

[2] M. Rycenga, C. M. Cobley, J. Zeng, W. Li, C. H. Moran, Q. Zhang, D. Qin, and Y. Xia. Controlling the synthesis and assembly of silver nanostructures for plasmonic applications. *Chemical Reviews*, Vol. 111, Issue 6, p. 3669-3712, 2011.

[3] A. Moores and F. Goettmann. The plasmon band in noble metal nanoparticles: an introduction to theory and applications. *New Journal of Chemistry*, Vol. 30, Issue 8, p. 1121-1132, 2006.

[4] J. Zeng, S. Roberts, and Y. Xia. Nanocrystal-based time–temperature indicators. *Chemistry - a European Journal*, Vol. 16, Issue 42, p. 12559-12563, 2010.

[5] E. Palagios, A. Chen, J. Foley, S. K. Gray, U. Welp, D. Rosenmann, and V. K. Vlasko-Vlasov. Ultra-confined modes in metal nanoparticle arrays for subwavelength light guiding and amplification. *Advanced Optical Materials*, Vol. 2, Issue 4, p. 394-399, 2014.

[6] W. P. Klein, C. N. Schmidt, B. Rapp, S. Takabayashi, W. B. Knowlton, J. Lee, B. Yurke, W. L. Hughes, E. Graugnard, and W. Kuang. Multiscaffold DNA origami nanoparticle waveguides. *Nanoletters*, Vol. 13, Issue 8, p. 3850-3856, 2013.

[7] N. Pazos-Pérez, W. Ni, A. Schweikart, R. A. Alvarez-Puebla, A. Fery, and L. M. Liz-Marzain. Highly uniform SERS substrates formed by wrinkle-confined drying of gold colloids. *Chemical Science*, Vol. 1, Issue 2, p. 174-178, 2010.

[8] T. Y. Jeon, D. J. Kim, S.-G. Park, S. h. Kil, and D.-H. Kim. Nanostructured plasmonic substrates for use as SERS sensors. *Nano Convergence*, Vol. 3, Issue 18, 2016.

[9] Z. Song, Z. Chen., X. Bian, L. Zhou, D. Ding, H. Liang, Y. Zou, S. Wang, L. Chen, C. Yang, X. Zhang, and W. Tan. Alkyne-functionalized superstable graphitic silver nanoparticles for raman imaging. *J. Am. Chem. Soc*, Vol. 136, Issue 39, p. 13558-13561, 2014.

[10] N. Tajima, M. Fukui, Y. Shintani, and O. Tada. In situ studies on oxidation of copper films by using atr technique. *J.Phys. Soc. Jpn.*, Vol. 54, Issue 11, p. 4236-4240, 1986.

[11] John A. Blackman. *Handbook of Metal Physics: Metallic Nanoparticles.* Elsevier, 1st edition, 2009. ISBN 978-0-444-51240-6.

[12] Hellmut Haberland. *Clusters of Atoms and Molecules : Theory, Experiment, and Clusters of Atoms.* Springer-Verlag, 1st edition, 1994. ISBN 978-3-642-84331-0.

[13] R. L. Johnston. The development of metallic behaviour in clusters. *Philosophical Transactions of the Royal Society A*, Vol. 356, Issue 1735, p. 211-230, 1998.

[14] C. G. Granqvist and R. A. Buhrman. Ultrafine metal particles. *Journal of Applied Physics*, Vol. 47, Issue 5, p. 2200-2219, 1976.

[15] B. M. Smirnov. Processes involving clusters and small particles in a buffer gas. *Phys. -Usp*, Vol. 54, Issue 7, p. 691-721, 2011.

[16] P. V. Kashtanov and B. M. Smirnov. Nanoclusters: Properties and processes. *High Temperature*, Vol. 48, Issue 6, p. 886-900, 2010.

[17] K. Wegner, P. Piseri, H. Vahedi Tafreshi, and Milani P. Cluster beam deposition: a tool for nanoscale science and technology. *J. Phys. D: Appl. Phys*, Vol. 39, p. 439-459, 2006.

[18] M. Ganeva, A. V. Pipa, B. M. Smirnov, P. V. Kashtanov, and R. Hippler. Velocity distribution of mass-selected nano-size cluster ions. *Plasma Sources Sci. Technol*, Vol. 2, 045011, 2013.

[19] V.N. Popok, I. Barke, E. E. B. Campbell, and K.-H. Meiwes-Broer. Cluster-surface interaction: From soft landing to implantation. *Surface Science Reports*, Vol. 66, Issue 10, p. 347-377, 2011.

[20] H. Hartmann, V. N. Popok, I. Barke, V. von Oeynhausen, and K.-H. Meiwes-Broer. Design and capabilities of an experimental setup based on magnetron sputtering for formation and deposition of size-selected metal cluster on ultra-clean surfaces. *Review of Scientific Instruments*, Vol. 83, Issue 7, 073304, 2012.

[21] J. A. Bittencourt. *Fundamentals of Plasma Physics.* Springer, 3rd edition, 2004. ISBN 978-1-4757-4030-1.

[22] V.N. Popok. Cluster beam synthesis of polymer composites with nanoparticles, ch. 2. In John Zhanhu Guo, Kenan Song, and Chuntai Liu, editors, *Polymer-Based Multifunctional Nanocomposites and Their Applications.* Elsevier, 2019. ISBN 978-0-12-815067-2.

[23] V. N. Popok, M. Hanif, F. A. Ceynowa, and P. Fojan. Immersion of low-energy deposited metal clusters into poly(methyl methacrylate). *Nuclear Instruments and Methods in Physics Research B*, Vol. 409, p. 91-95, 2017.

[24] S. Pratontep, S. J. Carroll, C. Xirouchaki, M. Streun, and R. E. Palmer. Size-selected cluster beam source based on radio frequency magnetron plasma sputtering and gas condensation. *Rev. Sci. Instrum.*, 76, 045103, 2005.

[25] M. Ganeva, A.V. Pipa, and R. Hippler. The influence of target erosion on the mass spectra of clusters formed in the planar dc magnetron sputtering source. *Surface & Coatings Technology*, Vol. 213, p. 41-47, 2012.

[26] M. Ganeva, T. Peter, S. Bornholdt, H. Kersten, T. Strunskus, V. Zaporojtchenko, F. Faupel, and R. Hippler. Mass spectrometric investigations of nano-size cluster ions produced by high pressure magnetron sputtering. *Contrib. Plasma Phys.*, Vol. 52, Issue 10, p. 881-889, 2012.

[27] T. Welzel and K. Ellmer. The influence of the target age on laterally resolved ion distributions in reactive planar magnetron sputtering. *Surface & Coatings Technology*, Vol. 205, p. 294-298, 2011.

[28] B. Chapman. *Glow Discharge Processes: Sputtering and Plasma Etching.* Wiley, 1st edition, 1980. ISBN 978-0-471-07828-9.

[29] S. M. Novikov, V. N. Popok, A. B. Evlyukhin, M. Hanif, P. Morgen, J. Fiutowski, J. Beerman, H.-G. Rubahn, and S. I. Bozhevolnyi. Highly stable monocrystalline silver clusters for plasmonic applications. *Langmuir*, Vol. 33, Issue 24, p. 6062-6070, 2017.

[30] K. L. Kelly, E. Coronado, L. L. Zhao, and G. C. Schatz. The optical properties of metal nanoparticles: The influence of size, shape, and dielectric environment. *J. Phys. Chem. B*, Vol. 107, p. 668-677, 2003.

[31] J. Reitz, F. J. Milford, and R. W. Christy. *Foundations of Electromagnetic Theory.* Pearson, 2009. ISBN 978-0321581747.

[32] Lukas Novotny. *Principles of Nano-optics.* Cambridge University Press, 2012. ISBN 978-1107005464.

[33] P. B. Johnson and R. W. Christy. Optical constants of the noble metals. *Physical Review B*, Vol. 6, Issue 12, p. 4370-4379, 1972.

[34] A. Curry, G. Nusz, A. Chilkoti, and A. Wax. Substrate effect on refractive index dependence of plasmon resonance for inidiviidual silver nanoparticles observed using darkfield microspectrometry. *Optics Express*, Vol. 13, Issue 7, p. 2668-2677, 2005.

[35] F. Faupel, V. Zaporojtchenko, T. Strunkus, and M. Elbahri. Metal-polymer nanocomposites for functional applications. *Advanced Engineering Materials*, Vol. 12, Issue 12, p. 1177-1190, 2010.

[36] A. K. Samal, L. Polavarapu, S. Rodal-Cedeira, L. M. Liz-Marzán, J. Pérez-Juste, and I. Pastoriza-Santos. Size tunable Au@Ag core-shell nanoparticles: Synthesis and surface-enhanced raman scattering properties. *Langmuir*, Vol. 29, Issue. 48, p. 15076-15082, 2013.

[37] W. Cao and H. E. Elsayed-Ali. Stability of Ag nanoparticles fabricated by electron beam lithography. *Materials Letters*, Vol. 63, Issue. 26, p. 2263-2266, 2009.

[38] T. W. H. Oates et al. The effect of atmospheric tarnishing on the optical and structural properties of silver nanoparticles. *J. Phys. D: Appl. Phys*, Vol. 46, 145308, 2013.

[39] M. Scuderi, M. Esposito, F. Todisco, D. Simeone, I. Tarantini, L. D. Marco, M. D. Giorgi, G. Nicotra, L. Carbone, D. Sanvitto, A. Passaseo, G. Gigli, and M. Coscuná. Nanoscale study of the tarnishing process in electron beam lithography-fabricated silver nanoparticles for plasmonic applications. *J. Phys. Chem. C*, Vol. 20, p. 24314-24323, 2016.

[40] G. H. Chan, J. Zhao, E. M. Hicks, G. C. Schatz, and R. P. V. Duyne. Plasmonic properties of copper nanoparticles fabricated by nanosphere lithography. *Nano Letters*, Vol. 7, Issue 7, p. 1947-1952, 2007.

[41] M. Shi, H. S. Kwon, Z. Peng, A. Elder, and H. Yang. Effects of surface chemistry on the generation of reactive oxygen species by copper nanoparticles. *ACS Nano*, Vol. 6, Issue. 3 p. 2157-2164, 2012.

[42] C. Gao, Z. Lu, Y. Liu, Q. Zhang, M. Chi, Q. Cheng, and Y. Yin. Highly stable silver nanoplates for surface plasmon resonance biosensing. *Angew. Chem. Int. Ed.*, Vol. 51, p. 5629-5633, 2012.

[43] A. Gutés, R. Maboudian, and C. Carraro. Gold-coated silver dendrites as sers substrates with an improved lifetime. *Langmuir*, Vol. 28, p. 17846-17850, 2012.

[44] V. G. Kravets, R. Jalil, Y.-J. Kim, D. Ansell, D. E. Aznakayeva, B. Thackray, L. Britnell, B. D. Belle, F. Withers, I. P. Radko, Z. Han, S. I. Bozhevolnyi, K. S. Novoselov, A. K. Geim, and A. N. Grigorenko. Graphene-protected copper and silver plasmonics. *Scientific Reports*, Vol. 4, Article No. 5517, 2014.

[45] J. C. Reed, H. Zhu, A. Y. Zhu, C. Li, and E. Cubukcu. Graphene-enabled silver nanoantenna sensors. *Nano Letters*, Vol. 12, p. 4090-4094, 2012.

[46] Y. Hu, Y. Shi, H. Jiang, G. Huang, and C. Li. Scalable preparation of ultrathin silica-coated Ag nanoparticles for sers application. *ACS Appl. Mater. Interfaces*, Vol. 5, p. 10643-10649, 2013.

[47] `http://www.oaresearch.co.uk/oaresearch/cluster/`. Accessed: 27-05-2019.

[48] M. Hanif, R. R. Juluri, M. Chirumamilla, and V. N. Popok. Poly(methyl methacrylate) composites with size-selected silver nanoparticles fabricated using cluster beam technique. *Journal of Polymer Science*, Vol. 54, Issue 12, p. 1152-1159, 2016.

[49] Ultraviolet-ozone surface treatment. *Three Bond Technical News*, Vol. 17, 1986.

[50] B. Janczuk and A. Zdziennicka. A study on the components of surface free energy of quartz from contact angle measurements. *J. Mater. Sci.*, Vol. 29, Issue 12, p. 3559-3564, 1994.

[51] Michael Quinten. *Optical Properties of Nanoparticle Systems - Mie and Beyond.* Wiley-VCH Verlag & Co., 1st edition, 2011. ISBN 0978-3-527-41043-9.

[52] P. W. Barber, R. K. Chang, and H. Massoudi. Surface-enhanced electric intensities on large silver spheroids. *Physical Review Letters*, Vol. 50, No. 13, p. 997-1000, 1983.

[53] M. Meier and A. Wokaun. Enhanced fields on large metal particles: dynamic depolarization. *Optics Letters*, Vol. 8, No. 11, p. 581-583, 1983.

[54] J. R. Krenn, G. Schider, W. Rechberger, B. Lamprecht, A. Leitner, and F. R. Aussenegg. Design of multipolar plasmon excitations in silver nanoparticles. *Applied Physics Letters*, Vol. 77, Issue 21, p. 3379-3381, 2000.

[55] Florian A. Ceynowa. *Formation of Metal-Polymer Nanocomposites Using Cluster Beam Technique.* PhD thesis, Aalborg University, 2017.

[56] M. Querry. Optical constants of minerals and other materials from the millimeter to the ultraviolet. *Contractor Report CRDC-CR-85034*, 1985.

Appendix A

Additional Simulations and Spectra

A.1 Simulations

This section of the appendix presents simulation showing how the plasmon band evolves depending on the weighting factor β as described in Subsec. 2.3.3. A weighting factor of $\beta = 1$ means that the NP is completely immersed in air, while a weighting factor of $\beta = 0$ means that the NP is completely immersed in the underlying substrate, in this case quartz.

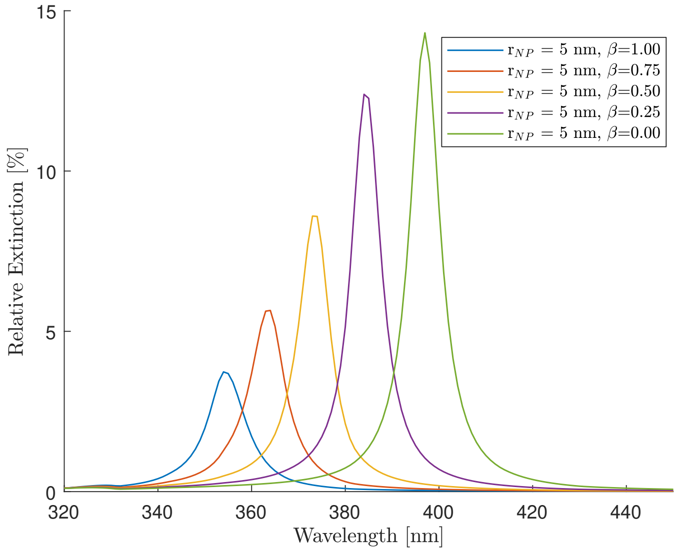

Figure A.1. Effect on the plasmon peak depending on the weighting factor for a spherical silver particle with a radius of 5 nm with the surrounding medium being air and the underlying substrate being quartz

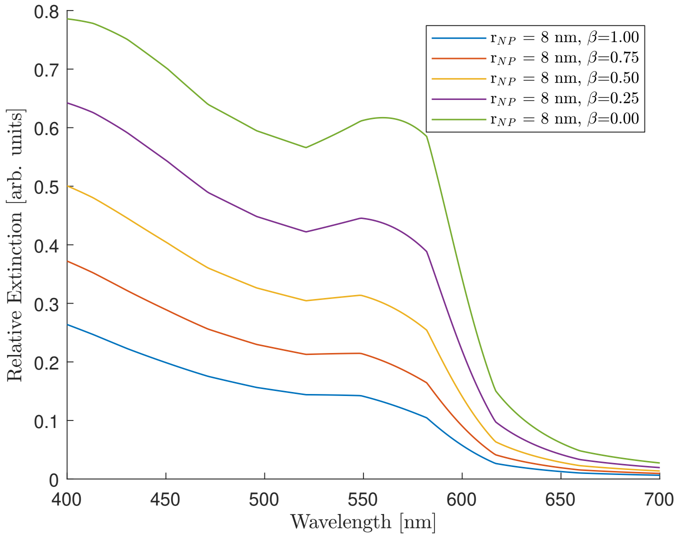

Figure A.2. Effect on the plasmon peak depending on the weighting factor for a spherical copper particle with a radius of 8 nm with the surrounding medium being air and the underlying substrate being quartz

A.2 Quartz Silver LSPR Spectra

This section presents additional spectra of the evolution of the LSPR of Ag NPs deposited on quartz substrates.

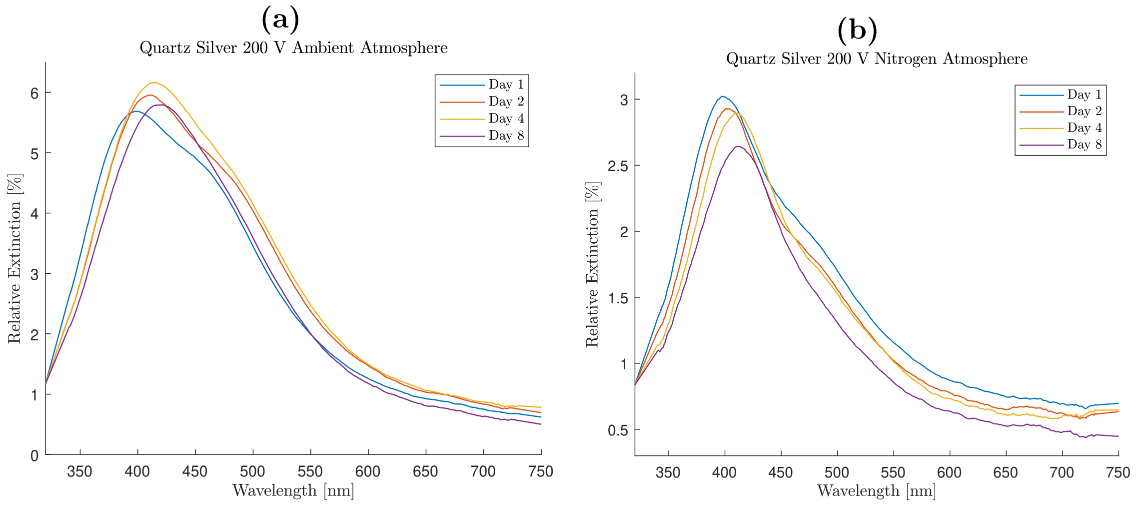

Figure A.3. Relative extinction spectra for (a) Q1 and (b) Q2, respectively with peaks as indicated in Tab. 4.3

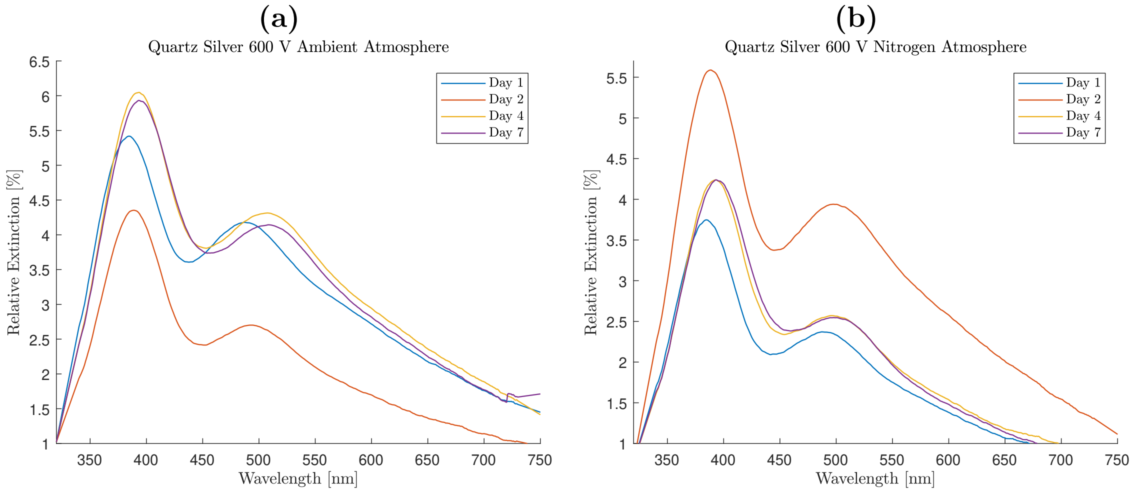

(a) Quartz Silver 600 V Ambient Atmosphere

(b) Quartz Silver 600 V Nitrogen Atmosphere

Figure A.4. Relative extinction spectra for (a) Q5 and (b) Q6, respectively with peaks as indicated in Tab. 4.3

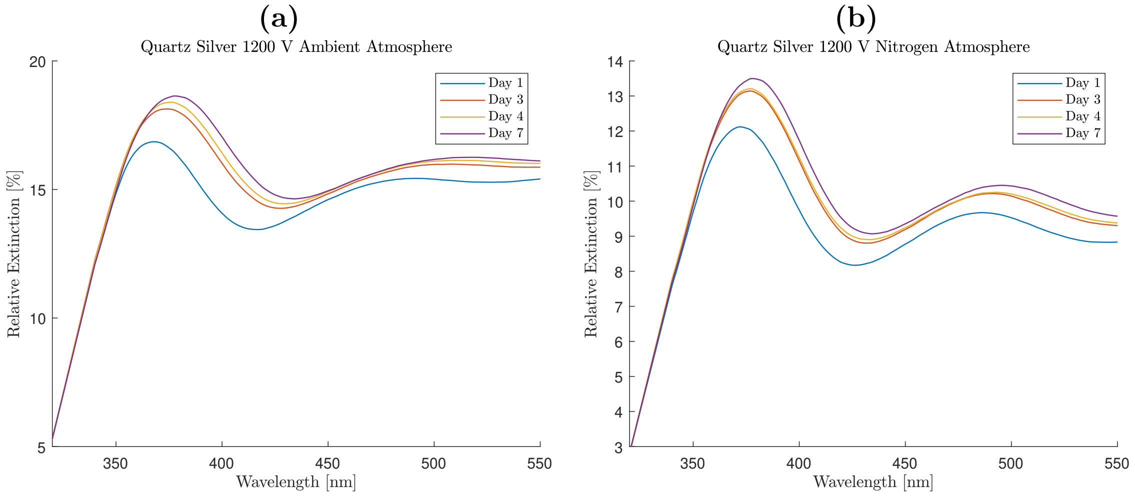

(a) Quartz Silver 1200 V Ambient Atmosphere

(b) Quartz Silver 1200 V Nitrogen Atmosphere

Figure A.5. Relative extinction spectra for (a) Q3 and (b) Q4, respectively with peaks as indicated in Tab. 4.3

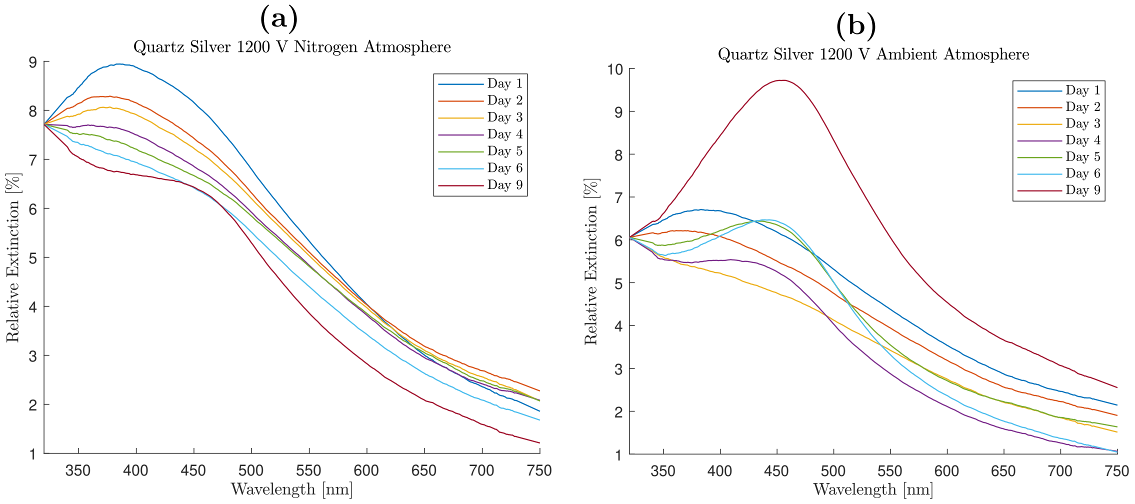

(a) Quartz Silver 1200 V Nitrogen Atmosphere

(b) Quartz Silver 1200 V Ambient Atmosphere

Figure A.6. Relative extinction spectra for (a) Q7 and (b) Q8, respectively with peaks as indicated in Tab. 4.4

A.3 PMMA Silver LSPR Spectra

This section presents additional spectra of the evolution of the LSPR of Ag NPs deposited on PMMA substrates.

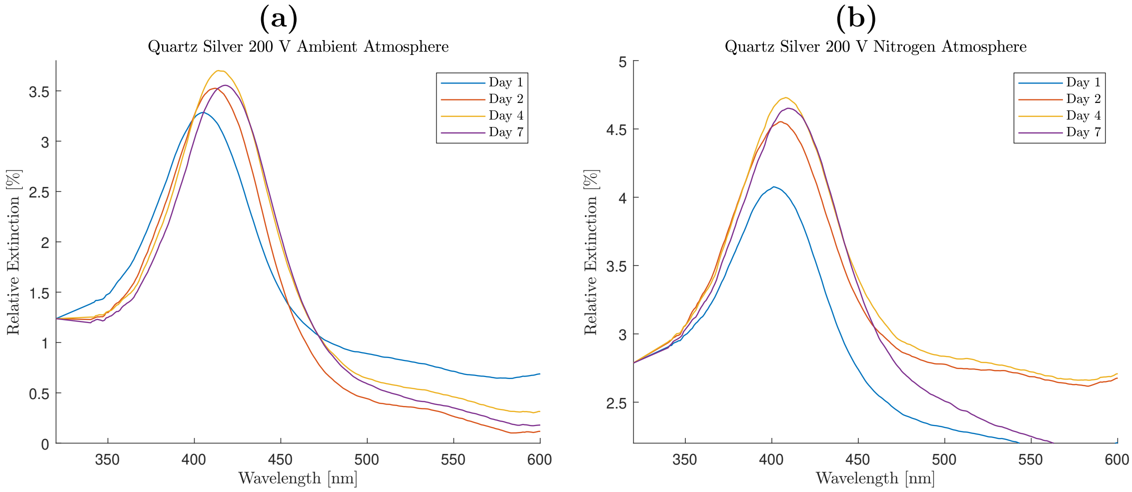

Figure A.7. Relative extinction spectra for (a) P3 and (b) P4, respectively with peaks as indicated in Tab. 4.5

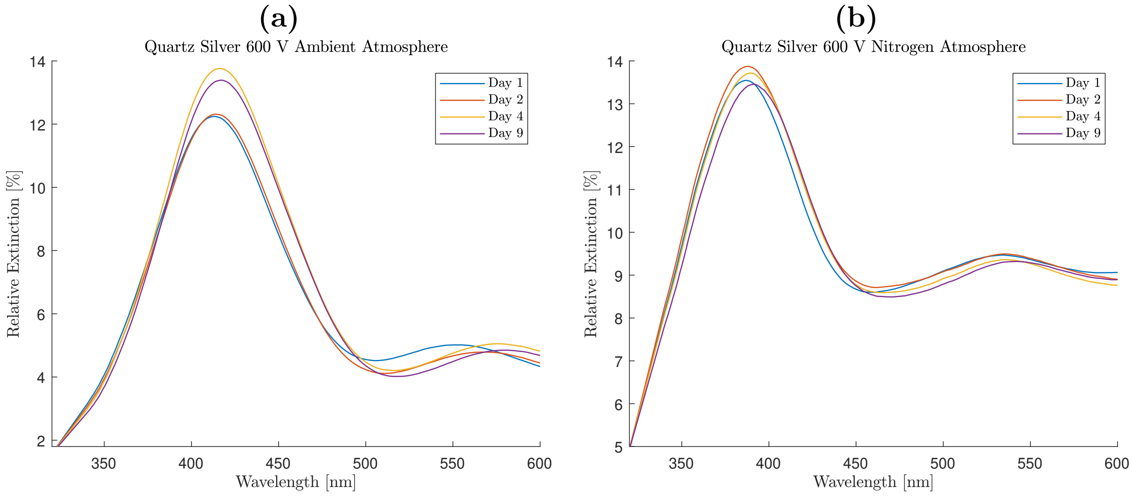

Figure A.8. Relative extinction spectra for (a) P7 and (b) P8, respectively with peaks as indicated in Tab. 4.5

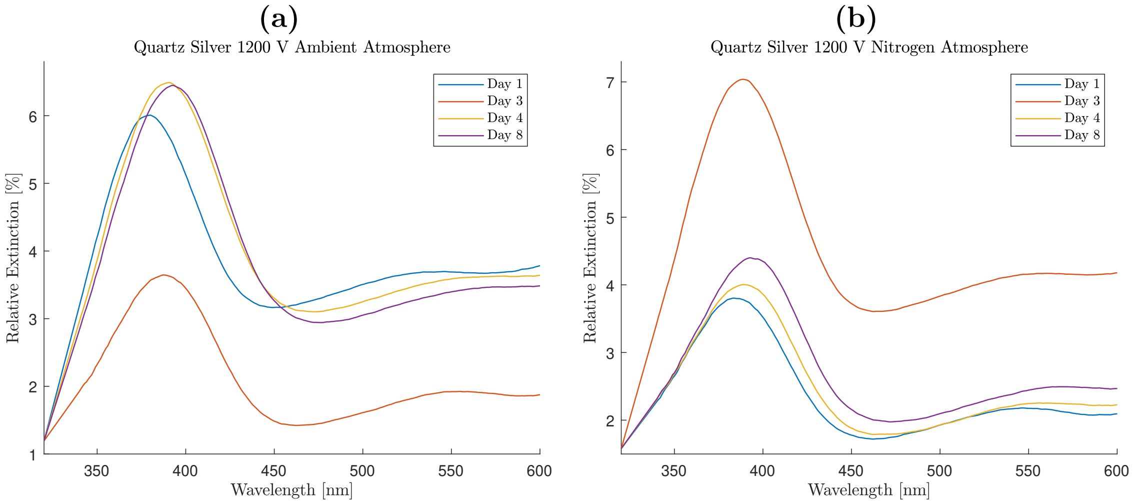

Figure A.9. Relative extinction spectra for (a) P5 and (b) P6, respectively with peaks as indicated in Tab. 4.5

A.4 Quartz Copper LSPR Spectra

This section presents additional spectra of the evolution of the LSPR of Cu NPs deposited on quartz substrates.

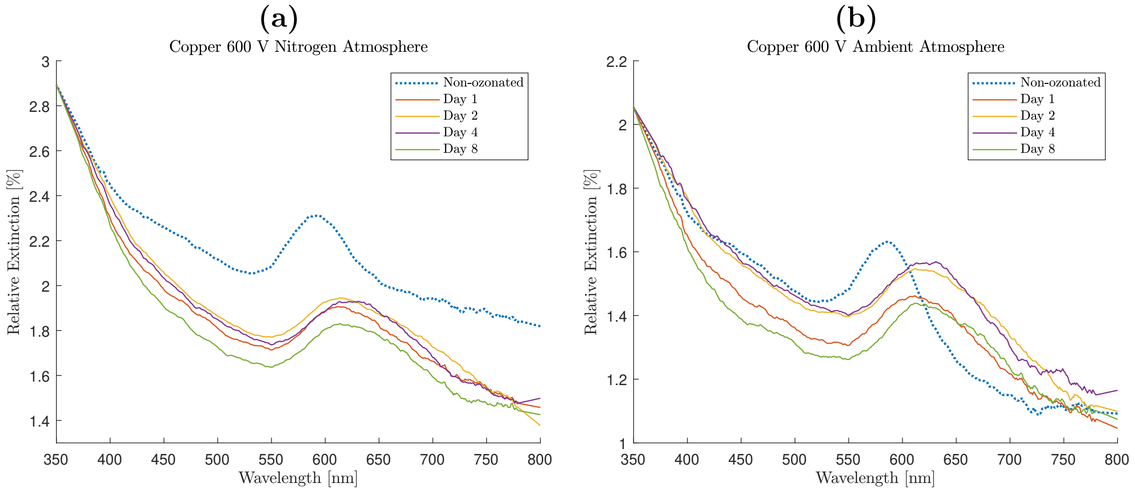

Figure A.10. Relative extinction spectra for (a) C5 and (b) C6, respectively with peaks as indicated in Tab. 4.6

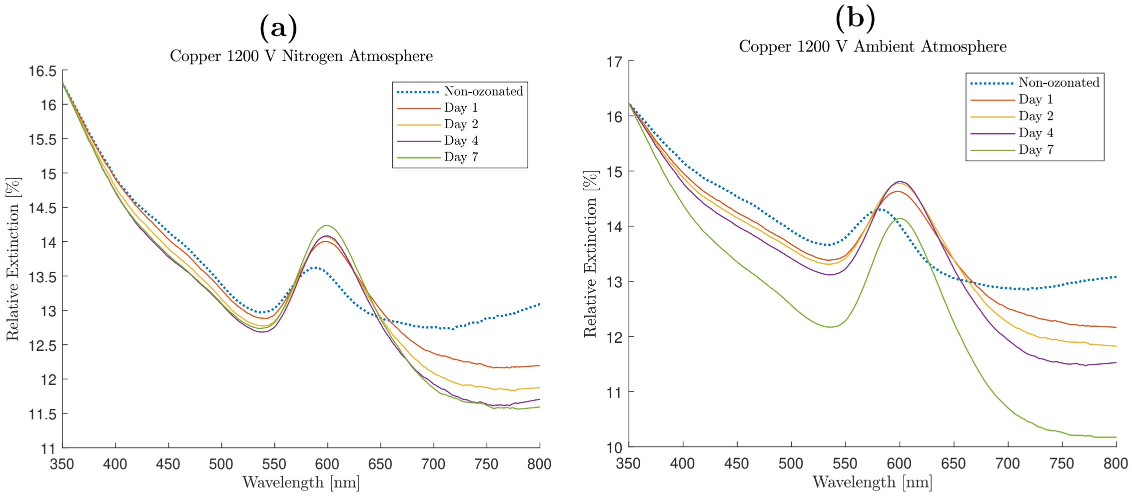

Figure A.11. Relative extinction spectra for (a) C1 and (b) C2, respectively with peaks as indicated in Tab. 4.6

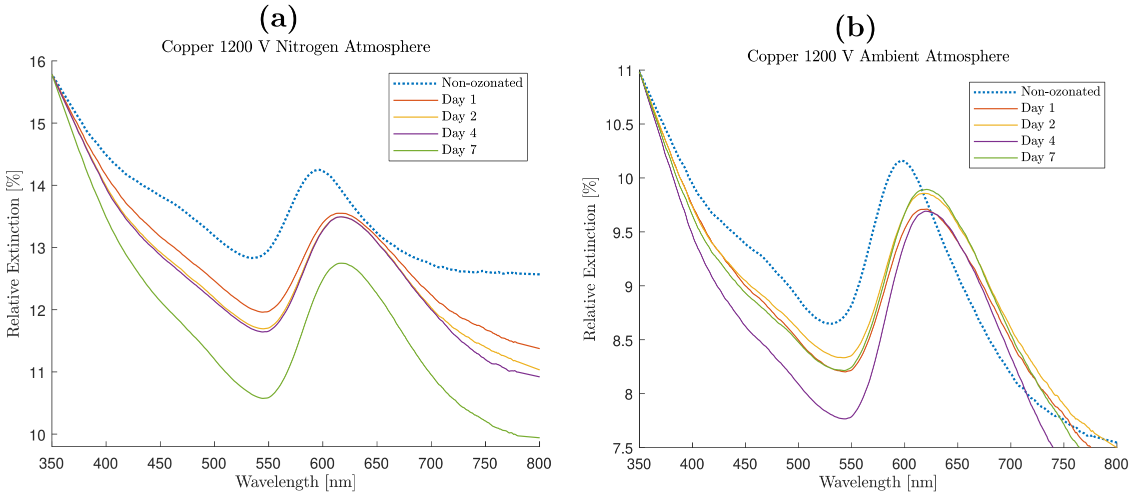

Figure A.12. Relative extinction spectra for (a) C3 and (b) C4, respectively with peaks as indicated in Tab. 4.6

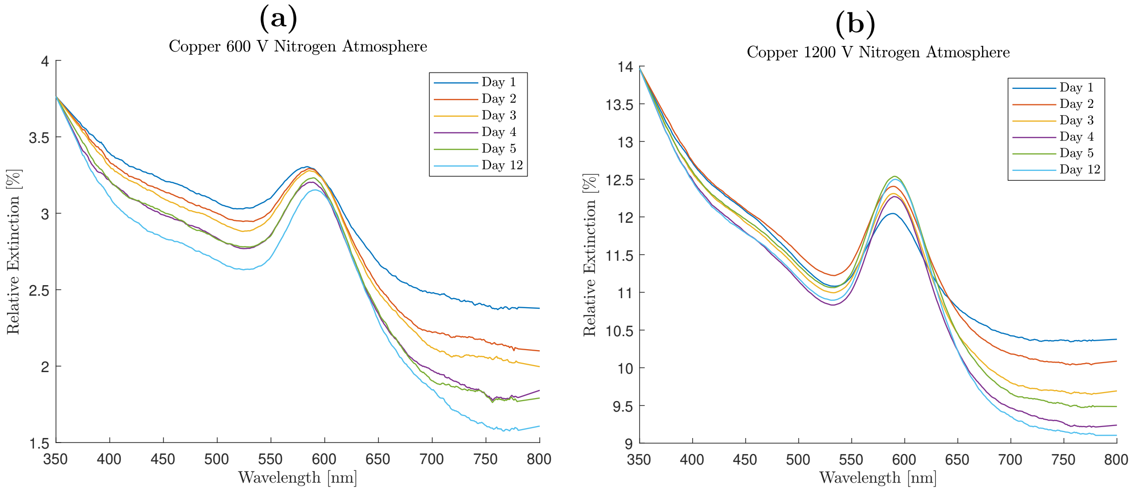

Figure A.13. Relative extinction spectra for (a) C7 and (b) C8, respectively with peaks as indicated in Tab. 4.7

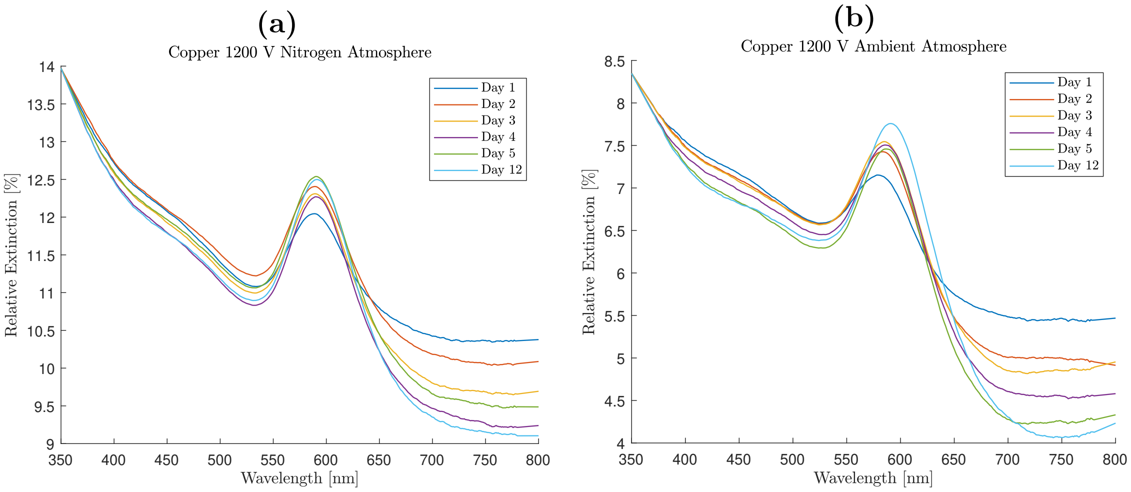

Figure A.14. Relative extinction spectra for (a) C9 and (b) C10, respectively with peaks as indicated in Tab. 4.7